This is to certify that the

thesis entitled

STRESS EVOLUTION DURING ISOTHERMAL AND ISOCHRONAL ANNEALING OF SPUTTERED NiTi THIN FILMS ON (100) - Si

presented by

Jinping Zhang

has been accepted towards fulfillment
of the requirements for

Master's degree in Materials Science

Major professor

Date 12-20-97

STRESS EVOLUTION DURING ISOTHERMAL AND ISOCHRONAL ANNEALING OF SPUTTERED NiTi THIN FILMS ON (100) - Si

By

Jinping Zhang

A THESIS

Submitted to
Michigan State University
in partial fulfillment of the requirements
for the degree of

MASTER OF SCIENCE

Department of Materials Science and Mechanics

1997

ABSTRACT

STRESS EVOLUTION DURING ISOTHERMAL AND ISOCHRONAL ANNEALING OF NiTi THIN FILMS ON (100) - Si

By

Jinping Zhang

The goal of this research has been to investigate the intrinsic stress resulting from sputtering, extrinsic thermal stress resulting from the temperature change in NiTi on (100)Si, stress evolution behavior during isochronal and isothermal annealing of as-sputtered films, and the interaction between stress and phase transformations in crystallized films. The latter may eventually lead to application of NiTi films as actuator materials in microelectromechanical systems (MEMS). Near-equiatomic Ni-rich NiTi films were fabricated by planar d.c. magnetron sputtering using Ni-rich NiTi cathodes, and near-equiatomic Ti-rich NiTi films were fabricated using a composite cathode. Thin film stress measurements by the wafer-curvature method showed that compressive intrinsic stresses resulted from the deposition parameters used, and the magnitude of the intrinsic stress depended on the working gas density as well as the film thickness. Both isothermal and isochronal annealing experiments showed that the residual stresses were stable below the deposition temperature. When the annealing temperature exceeded the deposition temperature, stress was relaxed by a two-stage process for crystalline films, and by a one-stage process for amorphous films. For both near-equiatomic Ni-rich NiTi films on Si and near-equiatomic Ti-rich NiTi on SiO_2/Si, extrinsic thermal stresses as high as 700 MPa were obtained by cooling the sample from a nearly stress-free state at a high annealing temperature, but were relaxed to nearly zero by R-phase and martensitic transformations. The stress was recoverable by reverse transformations taking place during heating. The reversibility of stress relaxation may be exploited to produce cyclic displacements useful in microelectromechanical systems.

ACKNOWLEDGMENTS

This project has been sponsored by the U.S. National Science Foundation and the Center for Fundamental Materials Research at Michigan State University.

I would like first to express my gratitude to my major advisor Professor David Grummon for his guidance and financial support. Special thanks to my committee members Professor Thomas Pence and Professor Martin Crimp for their valuable suggestions and comments to this thesis.

My appreciation is also extended to Reza Loloee, Li Hou, Zhibao Zhao, Tom Lagrange and Kuanbao Wang for their valuable help.

Finally, a special appreciation to my wife Fenglian, who has been understanding and supportive during my study in this period.

TABLE OF CONTENTS

LIST OF TABLES

LIST OF FIGURES

Figures

Chapter 1

INTRODUCTION

Shape Memory Alloys (SMAs) undergo a reversible displacive transformation between a low-temperature martensite phase and a high-temperature austenite parent phase [Wayman and Duerig, 1990]. It is characteristic of SMAs that large amounts of strain that are induced at relatively low flow stresses in the martensite can be recovered when the reverse martensitic transformation is completed, yielding a large force and/or displacement output [Otuska and Shimizu, 1986]. Alloys such as InTl, CuZnAl, CuAlNi, CuSn, AuCd, NiTi, and some ferrous materials have been found to exhibit this effect.

Near-equiatomic NiTi alloys have been the most technically important of the shape memory materials because of their high strain output and austenite toughness. It is well accepted that the displacive transformation underlying the Shape Memory Effect (SME) in NiTi is between a low-temperature B19' monoclinic phase and an ordered B2 phase (CsCl structure) [Goldstien, Kabacoff and Tydings, 1987; Wayman and Duerig, 1990]. In addition, a premartensitic transformation that forms a rhombohedral phase (R-phase) sometimes occurs which also exhibits a SME [Miyazaki and Otuska, 1986; Otsuka, 1990].

Martensitic transformation in near-equiatomic NiTi can produce a fully recoverable strain of up to 10% [Wasilewski, 1972], exceeding that of other known SMAs. In addition, near-equiatomic NiTi has a low martensite flow stress (~100 MPa), high austenite strength (>500 MPa) [Ford and White, 1996], excellent corrosion resistance [Beuhler and Wang, 1967], excellent fatigue properties [Melton and Mercier, 1979; Miyazaki, Sugaya

and Otsuka, 1989] and excellent biocompatibility [Lu, 1990], making it the first choice for many applications. Furthermore, ternary additions such as Cu, Nb, Fe, Hf, Pd and Pt can be readily added to modify transformation properties without destroying shape memory properties, allowing considerable flexibility for material system design.

There has been an increasing interest in developing thermal microactuators with high energy-density output. Crystalline NiTi thin films, which have larger energy-density output than any thermal actuator materials currently available [Johnson, 1991; Kim, 1994], have been demonstrated to possess shape memory properties comparable to those of their melt-solidified counterparts [Busch, Johnson, Hodgson, Lee and Stevenson, 1990; Busch, Johnson, Lee and Stevenson, 1990; Ikuta, Fujita, Ikeda and Yamashita, 1990; Walker, Gabriel and Mehregany, 1990; Chang and Grummon, 1992; Ishida, Takei and Miyazaki, 1993; Miyazaki and Ishida, 1994; Hua, Su, and Wuttig, 1995; Chang and Grummon, 1997]. Thermally driven Si-based NiTi microgrippers [Lee *et al.*, 1995] and various microactuators [Walker *et al.*, 1989; Kuribayashi *et al.*, 1990; Johnson, Busch, Ray and Charles, 1992; Grummon, Hou, Zhao and Pence, 1995; Krulevitch *et al.*, 1997] have been realized.

In order to achieve cyclic displacement output in microactuators, NiTi thin films must have biasing stresses, which can be internal or external, to deform the martensite during the cooling transformation. Thin film fabrication will often introduce intrinsic stresses, and also, temperature changes may result in extrinsic stresses. How to efficiently use those stresses to bias martensite is an important issue for actuators. Also of interest are the relations between the intrinsic stresses and process parameters, thermal stability of the stresses and the way that the stresses affect the martensitic transformation. Theses issues constitute the main objects of this thesis work.

In this thesis, the shape memory effect (with emphasis on that in NiTi alloys), thin film sputtering technology, stresses in thin films and current work on SMA NiTi thin films are reviewed in the *literature survey* chapter. Experimental techniques used in this research

work are illustrated in the *Experimental Methods* chapter. The experimental results on the stress and stress evolution during annealing and phase transformation of NiTi on Si are presented and discussed in the *Results and Discussion* chapter. The major results of this research are summarized in the *Conclusions* chapter.

Chapter 2

LITERATURE REVIEW

In this chapter, the fundamentals of, and experimental findings on SME and related phenomena, particularly in near-equiatomic NiTi alloys, are reviewed. Also, fabrication techniques, microstructural characterization and properties of thin films are discussed with an emphasis on NiTi SMA films. The present applications and possible future work of NiTi thin films are discussed.

2.1. The Shape Memory Effect and Near-Equiatomic NiTi Based Alloys

Since Chang and Read first discovered SME in Au-Cd alloy in 1951 [Chang and Read, 1951], it has been extensively studied by many groups, and a number of alloys have been found to be shape-memory materials. The list includes NiTi, Cu-Zn [Schroeder and Wayman, 1979], Au-Cd [Chang and Read, 1951], Cu-Zn-Al [Delaey *et al.*, 1981], Cu-Al-Ni [Arbuzova and Khandros, 1964], Ni-Al [Smialek and Hehemann, 1973], Fe-Mn-Si [Miyazaki and Otuska, 1989] Pd-Ti [Donkersloot and van Vucht, 1970] and others. Even some ceramics [Muddle and Traill, 1994] and polyimides [Hayashi, 1993] have been found to exhibit SME. Among those materials, NiTi-based alloys are the most important due to their superior properties. In this section a review including the fundamentals of SME, SME-related phenomena, and phase transformation, microstructure and alloying properties of NiTi is presented.

2.1.1. SME and Related Phenomena

SME is a shape recovering effect activated by temperature changes. In more detail, a plastic deformation produced when the materials are in the low-temperature phase can be recovered on heating. In metals, the shape recovery starts at the austenite start temperature (A_s) and completes at the austenite finish temperature (A_f). In the absence of stress, no overall shape change is associated with the martensitic transformation, which starts at the martensite start temperature (M_s) and is completed at the martensite finish temperature (M_f). The four characteristic temperatures M_s, M_f, A_s and A_f are illustrated in Fig. 2-1. Besides SME, other phenomena such as superelasticity of SMAs are also related to the martensitic transformation. In the following, the martensitic transformation in SMAs, martensite structure characteristics, one-way SME, two-way SME, superelasticity and other related properties of SMAs are described.

2.1.1.1. Thermoelastic Martensite vs. Non-Thermoelastic Martensite

The martensite in SMAs is thermoelastic and is characterized by a small transformation hysteresis and mobile martensite/austenite interfaces. Upon cooling, martensite plates continuously grow and new plates nucleate. If the cooling process is stopped, growth and nucleation cease, but if the cooling is resumed, growth and nucleation continue until the plates impinge with an obstacle such as a grain boundary or another plate. When the sample is heated, the reverse transformation occurs by the 'backwards' movement of the martensite/parent interface. The martensite plates revert completely to the parent phase and to the original lattice orientation, *i.e.*, complete crystallographic reversibility. Although martensitic transformations also occur in steels and carbonless ferrous alloys, there are distinct differences among the martensite in steels, in carbonless ferrous alloys and in shape-memory alloys. In steels, when the martensite is heated it undergoes tempering and eventual decomposition into equilibrium phases, *i.e.*, ferrite and carbide [Reed-Hill and Abbraschian, 1992]. In carbonless ferrous alloys such as Fe-Ni,

the martensitic transformation is reversible but the transformation hysteresis is as high as 420 K. In addition, during cooling, a martensite plate usually springs full size into existence, and then the interface between the martensite and parent phase becomes disarrayed and sessile. Such martensite plates do not exhibit 'backwards' movement when the specimen is heated. Instead, the parent phase (austenite) is nucleated as platelets within the martensite plates. Since several variants of the parent with different orientations are usually nucleated within a single martensite plate, the martensite plate as a whole does not revert to its original austenite orientation [Kessler and Pitsch, 1965]. The martensite in Fe-Ni alloys is thus non-thermoelastic [Kaufman and Cohen, 1958].

The thermoelastic martensitic transformation giving shape memory is characterized by several common features [Wayman, 1992]:

(1) The transformation has definite hysteresis, which means that there exists a temperature region at which the microstructure of the materials depends on the thermal history;

(2) The transformation is athermal, which means that phase fraction is only a function of temperature, and independent of isothermal holding time. This is due to the displacive nature of the transformation;

(3) The martensite usually has lower crystallographic symmetry than the parent phase;

(4) Martensite is often internally faulted by lattice imperfections such as twin boundaries and stacking faults;

(5) Plastic deformation of the martensite phase may be accomplished by twinning-type mechanism rather than dislocational slip.

2.1.1.2. Structure and Microstructure Aspects of the Martensitic Transformation in SMAs

Martensitic transformations are accompanied by a lattice distortion that resembles a simple shear, but in general is not exactly a shear, rather, an invariant-plane strain, and a lattice invariant plane exists during the transformation. Mathematically, an invariant-plane

strain is a homogeneous distortion such that the displacement of any point is in a common direction and proportional to the distance from the invariant plane. In most martensitic transformations, a volume change accompanies the structure which produces a normal component to the invariant-plane strain [Wayman, 1983].

A definite orientation relationship between the parent phase and martensite is found in the martensitic transformation in SMAs. However, due to the crystal symmetry of the parent phase, a number of martensite plates with different orientations may form even from a single-crystal parent phase. One martensite plate with a definite orientation is called a martensite variant. Since martensite can nucleate at different places, multi-variant martensite is expected to form upon cooling of austenite.

The martensite formed in SMAs is usually self-accommodating, which means the variants from in groups such that macroscopically the shape-strain is minimized, and microscopically intervariant junction planes are crystallographically reasonable [Miyazaki, Otuska and Wayman, 1989]. The self-accommodating morphology of martensite was observed from the optical microscopic observation of martensitic transformation induced surface relief of a flat surface prepolished prior to the formation of martensite in a Cu-40%Zn alloy. The invariant plane strain surface tilt gives an overall diamond-like morphology, with each diamond consisting of four crystallographic variants of martensite. Scratch observation indicates that although a straight scratch is locally deviated across the width of the individual plates of martensite, it still appears on the whole as a straight line. In more detail, if a given plate produces an 'up' displacement, its adjacent neighbor undergoes a 'down' displacement to annul the first, and the two plates thus self-accommodate each other. Electron diffraction investigation in TEM shows that the martensite plates in a single self-accommodation group are twin-related. Detailed analyses by invariant strain matrix indicate that the martensite variants form in self-accommodating groups because in doing so, the average deformation resulting from the transformation is minimized.

Thermoelastic martensitic transformations are found exclusively in ordered alloys, where an ordered parent phase is transformed into an ordered martensite. In such a case, ordering promotes crystallographic reversibility because the reverse transformation path in ordered alloys is unique, in contrast to multiple paths possible for disordered alloys [Otsuka and Shimizu, 1972]. Ordering also promotes a higher flow stress in the parent phase, making it less likely for the martensite parent interface to become damaged and then immobile as the plate grows [Dunne and Wayman, 1973].

Crystallographically, there is a lattice correspondence for the martensitic transformation. Wechesler, Liebermann and Read [1953, 1955] developed a theory, which is called WLR theory, that can phenomenologically explain structural and microstructural characteristics of the martensite. The basic assumption of WLR theory is that in order to minimize the transformation elastic strain energy, there exists a lattice invariant plane during the transformation. The transformational displacement may be analyzed as consisting of three components:

(1) A Bain distortion, which describes the lattice correspondence between the parent phase and the martensite phase but does not necessarily produce an invariant plane;

(2) A lattice invariant shear, which is realized by twinning or dislocation slip, which does not change the lattice symmetry but yields an undistorted interface plane;

(3) A rigid body rotation, which makes the undistorted plane that has been produced by the first two operations coincide in both martensite space and parent lattices.

2.1.1.3. Deformation Behavior of Martensite and One-Way SME

As shown in Fig. 2-2, deformation of martensite involves an elastic stage followed by a plastic stage. While the elastic stage is the same as that in non-SMA materials, the plastic stage involves a different mechanism. From the discussion in last section, cooling a single-crystal SMA from austenite results in a multi-variant martensite plates appearing in self-accommodated groups with no macroscopic shape strain. Because the variants in a

group are twin-related and the twin interfaces of thermoelastic martensite are mobile, and if the stress to activate dislocation movement is high enough, plastic deformation is realized by twin boundary movement, *i.e.*, in one self-accommodating variant group, one variant grows at the expense of others, in a process called detwinning. The deformation continues until only one variant in the sample is persisted. At this point the specimen surface is featureless. The surviving variant is that whose shape strain direction is most nearly parallel to the highest shear stress component. It is noted that though one self-accommodating group of variants eventually becomes a single variant by detwinning, coalescence of the variants from different self-accommodating groups must occur before single-variant martensite is formed. It is found that all the variants are capable of combining in a twin or pseudo-twin relation, as occurs in a 18R Cu-Zn-Al martensite [Adachi *et al.*, 1988]. Upon further loading of the single-variant martensite, it undergoes elastic deformation followed by plastic deformation by slip until the sample eventually fails, which is the same as that in non-SMA materials.

Because the twin-related variants are crystallographically identical, they are energetically equivalent and will not move back when the specimen is unloaded. Therefore, the deformation realized by detwinning is plastic in nature. When the detwinned martensite is heated between A_s and A_f, the original specimen shape and parent single crystal are regenerated. This is the shape memory effect.

SME is realized by the reverse transformation of thermoelastic martensite. Because of crystallographic restrictions and the necessity to maintain ordering, the detwinned martensite has only one way to undergo the reverse transformation. In other words, there are numerous variants of the Bain strain during the forward transformation but only one in reverse. It is to be noted that the 'one-way' memory just described is a one-time-only occurrence, but can be repeated by retransforming to the martensite, deforming it, and reheating it. Completely recoverable strains of over ten percent have been observed. The

shape memory process in a simplified two-variant model is schematically described in Fig. 2.3.

In polycrystalline SMAs, the deformation of martensite and the shape memory effect occur by the same mechanism as in single-crystal austenite. The only difference is that the grain boundaries are immobile, so each grain must be treated separately. The maximum recoverable strain is the average strain of all grains, and depends on the texture of the austenite grains.

2.1.1.4. Two-Way SME

In the one-way SME, the cooling from the parent phase does not generally give a macroscopic shape change due to the self-accommodating ability of martensite. However, shape memory materials can also be processed to give shape-strains on both heating and cooling transformation, in which case the SME is called two-way SME. Generally there are two ways to do this. One way is to use external biasing stress [Ditman and Bergman, 1994]. In that case, materials spontaneously switch between a low-temperature shape, which is formed by de-twinning the martensite at low flow stresses, and a high-temperature shape, which is restored by reverse martensitic transformation[1], upon heating. The other employs an intrinsic biasing stress. The intrinsic biasing stress may be created by SME cycling or loading-unloading cycling [Schroeder and Wayman, 1977], which introduces stabilized defects [Perkins and Sponholz, 1984; Liu and McCormick, 1990; Filip and Mazanex, 1996], or by constrained annealing, which introduces coherent/semicoherent second phases [Nishida and Honma, 1984]. In each case, the thermally induced martensite is not fully self-accommodated, but biased by the internal stress fields of the defects or second phases. The biased martensite microstructure may realize a different macroscopic

[1] If properly chosen, external biasing stress will produce only a small amount of elastic deformation at austenite, since it has a much higher plastic flow stress than martensite.

configuration with that of austenite. Up to 2% ~ 3% two-way memory strain is observed in cyclically trained samples.

2.1.1.5. Deformation Behavior of the Parent Phase and Superelasticity

At temperatures above M_s, martensite can also be stress induced, in which case the martensite is called stress induced martensite (SIM). According to Clapyron's equation in the strain-stress version:

$$\frac{d\sigma}{dT} = \frac{\Delta H}{T \cdot \Delta \varepsilon} \tag{2.1}$$

where σ, T, ΔH and $\Delta \varepsilon$ are the stress, transformation temperature, transformation enthalpy and resolved transformation strain in the direction of applied stress, respectively [Otsuka and Shimizu, 1986]. Since the martensitic transformation is exothermic (ΔH is positive) [Ortin and Planes, 1990] and $\Delta \varepsilon$ is also positive if σ is positive, the transformation temperature is expected to increase when an external stress is applied.

Due to the transformation hysteresis in temperature, the deformation behavior of austenite is different for different deformation temperatures, as shown in Fig. 2-4. When stresses are applied to an austenite material, it deforms elastically until either the critical stress for stress-induced martensitic transformation or dislocation movement related slip is reached, both of which are temperature dependent. If the critical stress for slip is higher at the deformation temperature (T_d),[2] stress induced martensitic transformation takes place prior to slip and the material may continue to deform by the formation of stress induced martensite, until the structure is fully martensitic [Wayman, 1992]. Unloading at this period of deformation, the material behaves differently depending on the deformation

[2] The temperature at which the critical resolved stress for dislocation slip equals that for stress induced martensite transformation is defined as the upper bound of temperature for superelasticity and is represented by M_d.

temperature. If $T_d < A_s$, the martensite is stable when the stress is released, so almost all strain is retained. If $A_s < T_d < A_f$, the martensite is partly retained upon unloading and hence only a part of the deformation is retained. In these two situations, only when reheated to A_f or above, can the material fully recover the deformation strain. If $T_d > A_f$, upon unloading, the martensite is no longer stable, and it spontaneously transforms back to austenite. Therefore, all the strain is recovered. This phenomenon is called superelasticity (SE), another well-known property of SMAs. More than 10% superelastic strain is observed in NiTi materials.

It is noted that stress induced martensite (SIM) is not a self-accommodated multi-variant martensite, but single-variant martensite in a given austenite grain. The variant chosen by the stress induced martensitic transformation is the one which experiences the maximum resolved shear stress. Further deformation results in the nucleation of numerous parallel variants, which eventually coalesce as the elongation approaches the maximum recoverable strain. Upon unloading, the inverse process occurs, whereby plates of the parent nucleate, coalesce, etc., restoring the parent grains in their original orientations, as occurs in SME.

2.1.1.6. Other Properties of SMAs

Among the properties of SMAs other than SME and PE, the rubber-like flexibility [Olander, 1932] and damping effects [Lin, Wu and Chang, 1994; Yeh *et al.*, 1994] are also observed. Rubber-like behavior is a spontaneous strain recovery upon loading occurring in fully martensitic materials, and was observed in Au-Cd alloy [Olander, 1932; Chang and Read, 1951], Cu-Al-Ni [Sakamoto, Otsuka and Shimizu, 1977], Cu-Au-Zn [Miura, Meada and Nakanishi, 1974], and Cu-Zn [Schroeder and Wayman, 1979]. Interestingly the rubber-like behaviors is found only after the martensite is aged for at least a few hours. Freshly transformed specimens exhibit only shape memory behavior. Based on microscopic observation, Chang and Read [1951] attributed the rubber-like behavior to

favorably oriented 'regions' growing at the expense of others, but did not explain the driving force for the springback. A number of mechanisms were proposed such as interaction between twinning dislocations and order faults inherited from the parent phase [Birnbaum and Read, 1961] and twinning shuffles which were time dependent [Lieberman *et al.*, 1975], but neither was experimentally supported [Ohba, Otsuka and Sasaki, 1990]. More recently, Japanese scientists [Cahn 1995] showed that a short-range order transition occurs during the aging of the deformed martensite which is correlated the transition to the rubber-like phenomenon. However, the driving force is yet not convincingly clarified.

Unusual damping properties are also found in SMAs. Good damping capacity is demonstrated when the SMA is in the martensitic form. Energy dissipation is realized by the movement of planar defects such as twin boundaries and variant interfaces. However, the best damping capacity is always found when the temperature is in the martensitic transformation temperature region. In this case, most of the energy is dissipated through the movement of martensite/parent phase interfaces. The damping effect of SMAs have found various applications in sports supplies[Yeh *et al.*, 1994].

2.1.2. Equiatomic NiTi and NiTi-Based SMAs

Although SME was found as early as 1951, it did not become of engineering significance until 1965, when Buehler, Gilfrich and Wiley at the U.S. Naval Ordnance Laboratory found SME in near-equiatomic TiNi, and named this alloy as Nitinol. Since then, considerable work in understanding of the transformation physics and in developing practical engineering application has been done. The development of NiTi alloy has been so successful that almost all the current SME applications are based on NiTi or TiNi-based ternary alloys.

Compared to other shape memory alloys, near-equiatomic NiTi alloy has the following advantages: (1) Better shape memory effect. Although it depends on the crystal orientation, a theoretically perfectly recoverable strain of up to 10% for single-crystal NiTi,

and 8.4% for polycrystalline NiTi have been found [Miyazaki, Nomura and Ishida, 1995], which are the best among all of the SMAs currently available; (2) Better fatigue properties and thermal stability. NiTi can work for more than 10^8 cycles at a recovery strain as high as 2% without serious SME degradation [Miyazaki, Sugaya and Otuska, 1989]; (3) Excellent mechanical properties. The alloys have an austenite strength > 620 MPa, martensite strength > 103 MPa, and room-temperature ductility of up to 60% [Buehler and Wang, 1968; Cross *et al.*, 1969]; (4) Excellent corrosion resistance [Vicentini *et al.*, 1986], which allows the products to work in severe conditions such as saline environments; (5) Biocompatibility [Lu, 1990], which allows the SMAs to work in the human body. The majority of the current applications of SMAs are biomedically related [Fukuyo *et al.*, 1990].

While the displacive transformations are the basis of SME, the diffusive transformations that take place at higher temperatures modify the microstructure of the material, thereby the mechanical properties and transformation temperatures can be modified, and the SME can be improved. The following describes the transformation aspects of near-equiatomic NiTi and ternary alloys.

2.1.2.1. SME and Displacive Transformations in Near-Equiatomic NiTi Alloys

The high-temperature equilibrium phase of equiatomic NiTi is the CsCl-type ordered structure (B2 structure) with a lattice parameter of 0.301 nm [Knowles and Smith, 1981, Matsumoto *et al.*, 1987]. Upon cooling, the material is subject to the following displacive transformation: B2 → Incommensurate phase (IC) → Commensurate Phase (CP) → martensite phase (M) [Hwang *et al.*, 1983; Wayman, 1983]. The B2 parent phase also transforms directly to martensite without the intermediate phases if certain free energy criteria are satisfied [Liu and McCormick, 1996]. Upon heating, the martensite can transform to the B2 parent phase with or without intermediate phases, also according to the thermodynamic conditions.

In the incommensurate phase, atoms move slightly away from the rational positions, creating diffuse features in electron diffraction patterns. The B2 → IC transformation is a second-order transformation and it is accompanied by a sharp increase of resistivity. The CP is formed from IC when the atoms are locked at the exact rational positions and a rhombohedral angle is achieved. Therefore, the CP is called the R phase. The rhombohedral angle further deviates away from a right angle when the temperature is decreased [Ling and Kaplow, 1981; Meichle *et al.*, 1981]. The B2 → R transformation (R-phase transformation) is a first-order transformation which is accompanied by an internal friction peak and a decrease in elastic modulus. The R phase is characterized by 1/3 superlattice reflections along major directions such as <110> and <111> in reciprocal space [Wu and Wayman, 1989] and by weave-like domains in the microstructure [Xie *et al.*, 1990]. Since the rhombohedral angle is achieved by lengthening one of the <111> direction of the B2 unit cell, there are a total of 8 possible R-phase variants.

The formation of martensite, regardless of whether it comes from the R phase or directly from the B2 parent phase, is a first order transformation. The martensite of NiTi has a monoclinic structure with lattice parameters a = 0.2889 nm, b = 0.4120 nm, c = 0.4622 nm and $\gamma = 98.6°$ [Matsumoto *et al.*, 1987]. The orientation relationship between martensite and austenite is [Otsuka, Sawamura and Shimizu, 1971]

$$\begin{aligned} &[111]_M \,//\, [\bar{1}\,\bar{1}\,1]_{B2} \\ &(001)_M \overset{\sim 6.5}{//} (101)_{B2} \end{aligned} \qquad (2.2)$$

Due to lattice symmetry of the parent phase, there are 12 lattice correspondences satisfying the orientation relationship, and these 12 lattice correspondences further form 24 habit plane variants when internal twinning is considered [Matsumoto, Miyazaki, Otsuka and Tamura, 1987].

For solution-treated binary NiTi, the B2 → R transformation and the R → M transformation are so close that no temperature interval is detected. By adding a third

element such as Fe into the binary alloy, or annealing Ni-rich NiTi alloys at intermediate temperatures, the martensitic transformation can be depressed and the R-phase transformation can be separated from the martensitic transformation. Both the R-phase transformation and the martensitic transformation exhibit SME and PE by the mechanism described in 2.1.1. The SME and PE associated with the martensitic transformation in NiTi exhibit a fully recoverable strain of up to 10%, while those associated with the R-phase transformation exhibit a fully recoverable strain near 1% [Ling and Kaplow, 1980]. The R-phase transformation is unique in that the transformation hysteresis is as narrow as 1 K [Hwang *et al.*, 1983], which is particularly useful for developing snap performance in thermal actuators.

2.1.2.2. Diffusive Transformations in Near-Equiatomic NiTi Alloys

Although Koskimaki *et al.* [1969] reported a eutactoid transformation

$$\beta(NiTi) \rightarrow Ni_3Ti + Ti_2Ni \qquad (2.3)$$

occurred when a near-equiatomic NiTi alloy was annealed at intermediate temperatures ($0.3T_m$ to $0.6\ T_m$), no other independent experiments confirmed this kind of decomposition [Wasilewski *et al.*, 1971]. Thus, it has been generally accepted that the B2 structure is a stable phase at high temperature. Whether the alloys are Ni rich or Ti rich is important for diffusive solid state reactions. According to the equilibrium phase diagram (Fig. 2-5), stoichiometric NiTi can dissolve almost no excess Ti, but can dissolve up to a few percent of excess Ni at solution temperatures. In most Ti-rich NiTi alloys (with atomic compositions more than 50at.% Ti but less than 67at.% Ti), the equilibrium microstructure would be a mixture of β-NiTi and the intermetallic compound Ti_2Ni, which has a B2 structure with a = 0.301 nm, and hexagonal structure with lattice parameters a = 0.2549 nm and c = 4.3648 nm [Bhan, 1971], respectively. For near-equiatomic Ti-rich NiTi alloys,

the matrix essentially is β-TiNi, so the transformation temperatures changes little even though the intermetallic compound Ti_2Ni, which tends to appear near grain boundaries, has negative effects on the mechanical properties of the materials.

Diffusive intermetallic reactions in Ni-rich near-equiatomic NiTi are much more significant than those in Ti-rich NiTi alloys. Firstly, there are a number of metastable intermetallic compounds such as Ni_3Ti, Ni_3Ti_2 and Ni_4Ti_3 that may appear when the materials are annealed at intermediate temperatures (673 K ~ 973 K). The Ni_3Ti phase has a hexagonal structure with lattice parameters a = 0.5109 nm and c = 0.8310 nm [van Vucht, 1966], the Ni_3Ti_2 has a hexagonal structure with lattice parameters a = 0.44028 nm and c = 1.3525 nm [Nishida, Wayman and Honma, 1987], while the Ni_4Ti_3 has a rhombohedral structure with lattice parameters of a = 0.661 nm and α = 113.65° [Kinuma, Matsumoto and Honma, 1986], or equivalently, a hexagonal structure with lattice parameters of a = 1.124 nm, c = 0.5077 nm [Saburi, Nenno and Fukuda, 1986]. A sequence of precipitation was obtained by Nishida *et al.* [Nishida, Wayman, Honma, 1986; Nishida and Wayman, 1987] when they worked on a $Ti_{48}Ni_{52}$ alloys:

$$\beta_0 \rightarrow \beta_1 + Ni_4Ti_3 \rightarrow \beta_2 + Ni_3Ti_2 \rightarrow \beta_3 + Ni_3Ti \qquad (2.4)$$

where β_0 represents the structure of the as-solution treated alloys, and β_1, β_2 and β_3 represent the structures of the matrix after the precipitates Ni_4Ti_3, Ni_3Ti_2, Ni_3Ti are formed. Independent work by Beyer *et al.* [1986] on NiTi-Ni diffusion couples supported these results.

Secondly, metastable phases exert important effects on the R-phase and martensitic transformations. The most significant metastable phase is Ni_4Ti_3. It is lenticular in appearance and can be obtained by annealing the Ni-rich NiTi at temperature between 673 K and 873 K. The orientation relationship between the precipitates and the B2 matrix is [Nishida, Wayman, Kainuma and Honma, 1986]:

$$\begin{aligned} &(100)_{Ni_4Ti_3} /\!/ (142)_{B2} \\ &[001]_{Ni_4Ti_3} /\!/ [0\bar{1}2]_{B2} \end{aligned} \tag{2.5}$$

The habit plane of the precipitation is {111}, and because of the symmetry of the matrix, there are 8 variants of precipitates in total.

Ni_4Ti_3 precipitates affect the R-phase and martensitic transformations differently according with the precipitation stage. When the precipitates are small, a coherent interface with the matrix is maintained. The martensitic transformation is seriously delayed, and the interface stress of the precipitates tends to encourage a single-variant martensite [Nishida and Honma, 1984; Xie *et al.*, 1990], by which biased martensite is formed if the material is sufficiently cooled.

As the precipitates grow, the coherent interface becomes semi-coherent even incoherent, and it becomes a favorable nucleation site for martensite instead [Xie *et al.*, 1990]. By selectively encouraging the growth of Ni_4Ti_3 variants through constrained annealing of Ni-rich β solid solution at intermediate temperature, Nishida *et al.* [1984] found that the two-way SME was realized. The stress biasing effect on the growth of the precipitates was recently proved by Li and Chen [1997] in Ni-rich NiTi under uniaxial stress conditions.

2.1.2.3. NiTi-Base Ternary Alloys

Although near-equiatomic binary NiTi alloys exhibit excellent SME and PE, these alloys have a number of disadvantages. The transformation temperature is very composition-sensitive and the servicing temperature can not be higher than 373 K. Alloying has proven to be an efficient way to modify the properties of the material. The following section briefly describes the most popular ternary NiTi base alloys.

NiTi-Cu SMAs. Transformation temperatures in binary near-equiatomic NiTi are very sensitive to composition. 1 atomic percent excess Ni can decrease M_s by 100 K if all the excess Ni atoms are dissolved into the matrix. Up to 30 at.% addition of Cu substituted for Ni considerably decreases the sensitivity of the transformation temperature on composition [Vanloo, 1978; Mercier and Melton, 1979], making it easier to control the transformation temperature by composition adjustment. In addition, NiTi-Cu has a number of other advantages over binary NiTi. For example, the martensite de-twinning stress is lowered, the hysteresis is narrowed, and fatigue properties are improved [Proft, Melton and Duerig, 1987]. Another feature of NiTi-Cu is that typically the A_s is just above human body temperature, which is convenient for use in biomedical applications [Krulevitch, 1996]. Crystallographically, the lattice parameters of martensite change with increasing Cu addition, and if the Cu content is more than 10 at.%, an orthorhombic martensite may appear before the monoclinic martensite does, yielding a two-step martensitic transformation [Moberly and Melton, 1990].

NiTi-Nb SMAs. Narrow hysteresis is useful for thermal actuation, but wide hysteresis is useful in some other applications such as pipe couplings, where it is desirable for the opened SMA component not to shrink upon a slight temperature increase, and once it shrinks, it does not loosen from transformation while in service. Addition of Nb near 10 at.% works well in widening the transformation hysteresis. It has been reported that in $NiTiNb_9$ alloys, the hysteresis is as large as 130 K [Melton, 1986]. Microstructurally, Additional Nb is not miscible in either the parent phase or the martensite. It exists as pure Nb islands distributed in the matrix, but it does change the deformation behavior of the martensite. The deformation of a NiTiNb material occurs in the martensite as well as the pure Nb islands since Nb is very easy to deform. When heated, the deformed Nb delays the reverse transformation by elastic interactions, therefore, the transformation hysteresis is widened [Zhang *et al.*, 1990].

Ni(TiHf) and Ti(NiPd) SMAs. High-temperature SMAs are needed in automotive and spacecraft applications. Because the M_s temperature of binary NiTi is less than 373 K [Thoma *et al.*, 1991], no SME applications over 373 K can be made with binary NiTi. However, by substituting Zr or Hf for Ti, or by substituting Pd or Pt for Ni, the transformation temperatures can be substantially increased. Although the first few percent of Hf or Pd actually lowers transformation temperatures slightly, if the Hf addition is more than 5 at.% [Angst, Thoma and Kao, 1995], or Pd more than 10 at.% [Lotkov *et al.*, 1982], the transformation temperatures increase very rapidly. 15% of Hf addition or 30% of Pd can raise the M_s temperature to as high as 473 K. In addition, these new ternary alloys have a recoverable strain of up to 3% and satisfactory thermal stability, making them feasible for high-temperature SME applications [Pu *et al.*, 1994]. Crystallographically, there also exist monoclinic martensite and orthogonal martensite, the latter of which appears as the ternary additions increase [Sivokha *et al.*, 1983; Han *et al.*, 1996].

2.2. Thin Film: Fabrication, Microstructure and Stresses

Thin film science and technology plays an important role in industry. While the major exploitation of thin films has been in microelectronics, there are also increasing applications in communications, optical electronics, coatings of all kinds, and in energy generation and conservation strategies, which are also of great interest. Since this thesis work is on NiTi thin films, a review on thin film fabrication and characterization is useful. In the following, the sputtering technique, which is an extensively used method for making thin films and is the major method for NiTi thin film fabrication, is described in detail. Structural characteristics of sputtered films and stress development in thin films are reviewed.

2.2.1. Thin Film Fabrication: Sputtering

There are numerous methods of making films, but there basically are two categories, Chemical Vapor Deposition (CVD) and Physical Vapor Deposition (PVD), according to whether chemical reactions are involved during the deposition. The sputtering method, one of the PVD methods, has a high deposition rate and a high flexibility of target material selection, thus has been favored for small-area deposition.

A sputtering system is composed of a vacuum chamber, which is usually filled to low pressure with an inert working gas (usually argon), a cathode, which is the 'target' material which is connected to a negative voltage supply, and a substrate holder forming the anode and facing the target. Ionized gas atoms (usually Ar) gain kinetic energy through the electric field and accelerate toward the cathode. Atoms in the cathode are ejected from the surface by the knock-on effects of the incoming ions, and deposit on a substrate, forming a continuous film. The collision cascades between the ions and target atoms not only yield neutrals of the target material, but also yield Auger electrons, secondary electrons, and reflected neutral species of the working gas. The secondary electrons are critical for the maintenance of the plasma, which is primarily determined by the working gas pressure. If the working gas pressure is too high, insufficient secondary electrons are produced since the ions lose most of their energy in collisions on the way to the cathode. If the working gas pressure is too low, even if there are enough secondary electrons in the initial period, the ion flux keeps diminishing because not enough working gas atoms are ionized. Both of the situations eventually lead to loss of the plasma and termination of the deposition [George, 1992].

What was described above is essentially glow discharge d.c. sputtering, which uses a d.c. electric field to accelerate the ions and the plasma is self-sustained. As described in the last paragraph, the sputtering must operate with a limited range of working gas pressure (usually >10 mTorr). The most serious drawback of the self-sustained glow discharge as a technique for the sputter deposition of films is contamination of the deposited film by the

inert gas used to produce the discharge. But concentration of this trapped inert gas in the film can be lowered if the sputtering is done at low pressure. Another advantage that might be expected from sputtering at low pressure is the higher mean energy of the sputtering particles when they strike the substrate, resulting in better adhesion and more compact films.

There are several ways to realize sputtering at low pressure. One is triode sputtering. In triode sputtering systems, an independent thermionic source is used to supply additional electrons for the maintenance of the discharge glow at low working gas pressure. The anode of the thermionic source is biased positively with respect to the substrate to avoid the collection of electrons at the substrate, which may result in gross inhomogeneities in plasma density at the target. Triode sputtering allows operation at much lower pressures ($<10^{-3}$ Torr) than in a conventional diode glow discharge system. Another way to enable the sputtering to work at low working gas pressure is magnetron sputtering. The permanent magnets backing the planar cathode in a magnetron sputtering gun make the secondary electrons move in orbits so that the probability of working gas ionization is promoted because the path of secondary electrons becomes much longer. Most magnetron sources operate in the pressure ranging of 1 to 20 mTorr and with a cathode potential of 300 ~ 700 V. In comparison to the conventional diode sputtering, magnetron sputtering gives high deposition rates at lower working-gas pressure and also high-quality films at low substrate temperatures.

2.2.2. Composition, Structure, Microstructure and Properties of Sputtered Films

There are a number of parameters involved in a sputtering process such as working gas species, working gas pressure, working distance (cathode-to-substrate distance), deposition power and substrate temperature. The compositions, microstructure and physical properties of the as-sputtered films depend on the processing parameters chosen, which issues are discussed next.

2.2.2.1. Compositions

It is obvious that a pure-element target produces pure-element film by sputtering even though film growth rate may constantly change with time due to the topographical changes in the target. For alloy cathodes, because the sputter yields of different species are different, preferential sputtering effects may exist. So it is expected that when the deposition is started, the composition of the mass flux will deviate from that of the target material. However, for a well cooled cathode where diffusion is negligible, as the sputtering process progresses, the composition at surface and sub-surface changes such that preferentially sputtered atom species decreases while the other species increases. Eventually, a steady-state mass flux of the same composition as the target material will be achieved. Of course, it can be imagined that an over-worn target will produce films of an unpredictable composition since at that time the geometric configuration of the target has changed substantially.

Although eventually the mass flux of the sputtered neutrals reaches a steady state with the same composition as the target, the resulting film does not necessarily do so. This is primarily because (1), stereo angular distribution of each sputtered species may not be the same, therefore, the composition of the film may vary from site to site, (2) more importantly, a preferential re-sputtering effect may occur on the film. Resputtering is a process whereby some atoms in the growing films are sputtered off by bombardment with the incoming species. Some of the atom species are thus preferentially back-sputtered due to the difference of sputter yielding rates among different species, and no steady state evolves. In general, lighter atoms preferentially re-sputter, but some other effects such as bond energies and saturated vapor pressure are also important in determining the preferential sputtering sequence. Biasing voltage on the substrate, as well as low working gas pressure and off-axis deposition conditions may increase the extent of preferential resputtering.

2.2.2.2. Structure and Microstructure

The structure of the as-sputtered film is strongly dependent on the process parameters such as working gas pressure, working distance, deposition rate, off-axis conditions and substrate temperature, among which the substrate temperature is the most important. Thornton [1977] developed a zone structure model for sputtered films which was extended from the work by Movchan and Demchishin [1969] on electron beam evaporated films. It states that the microstructure of the sputtered films are divided into basically three 'zones' depending on the homologous deposition temperature T_s/T_m (where T_s is substrate temperature during deposition, T_m is the melting temperature of the film):

Zone I ($T_s/T_m < 0.3$): Characteristic microstructure of the films is either amorphous, dentrite or noncrystalline. In each case the structure is extended in the growth direction. The films are rather porous, and possess very poor mechanical properties.

Zone II ($0.3 < T_s/T_m < 0.5$): The most characteristic feature of the microstructure is largely uniform columnar structure with high compactness. The grain diameter, d, extends throughout the thickness of the film, t, but the grain aspect ratio d/h usually less than one.

Zone III ($T_s/T_m > 0.5$): metallic films have a columnar structure with a grain diameter greater than the thickness of the film. The texture of the films is very strong. At extreme conditions, the grain growth behaves like epitaxial growth.

Although it is suggested that there is a regime between Zone I and Zone II where the grain structure changes smoothly from characteristics of one zone to those of the other as the substrate temperature changes [Thornton, 1977], later experiments showed that the grain structure underwent a discontinuous evolution characterized by the formation of a bimodal grain structure [Smith and Ibrahim, 1984].

The zone structure itself can be explained to some extent in terms of self-shadowing, surface diffusion, bulk diffusion, which, along with adsorption of adatoms, constitute four basic processes of film formation [Thornton, 1977; Chopra, 1979; Ohring, 1992]. In the first regime, both adatoms and inner atoms have very poor mobility. Due to self-shadowing effect, porous structures are usually developed. Intermediate substrate temperature allows sufficient surface diffusion of the adatoms but sluggish bulk diffusion of the inner atoms. At this time, more compact films result, but meanwhile, numerous grain boundaries exist. High substrate temperature allows both sufficient surface diffusion and bulk diffusion, therefore, large grain size will result.

For sputtering, working gas pressure is another important parameter since it evidently affects the zone structure. The momentum exchange of the incoming species with the adatoms provide more energy for movement to stable low-energy sites. The kinetic energy of the incoming species diminishes during transport to the substrate if collisions with working gas molecules occur. Low working gas pressure decreases the probability of such collisions, and thus, help to preserve the kinetic energy of the incoming species. As a consequence, lowering working gas pressure is similar in a sense to increasing the deposition temperature [Hoffman and Thourton, 1979; Hoffman, 1983], making the whole zone structure move toward lower temperature regime.

2.2.2.3. Adhesion and Surface Roughness

Interfacial adhesion at the film/substrate interface depends on both the nature of the electronic bonding at the interface and other factors such as substrate morphology, chemical diffusion, contamination, and defects. Strong adhesion of thin films is associated with enhanced substrate-adatom bonding, small local stress, uniform film thickness, and absence of an easy deformation or fracture path [Mattox, 1978]. In practice, adhesion may be improved by means such as substrate cleaning, reduced pressure during deposition, removal of surface oxides and reduction of film thickness. High energy ion bombardment

before or during sputter deposition has been also used to improve the adhesion of thin films [Baglin, 1987].

The surface morphology of thin films evolves in both the deposition process and during post-deposition processes. During deposition, while the surface diffusion potentially makes the film smoother [Chason *et al.*, 1984], resputtering resulting from bombardment by incoming species tends to make the film rougher [Keste and Messier, 1993]. It has been observed that the etching effect induced by resputtering causes considerable non-uniform thickness in the film, which is aggravated by increasing sputtering power, prolonged deposition time, decreasing the working gas pressure, decreased working distance and increased O_2 levels. Microscopically, resputtering causes the formation etch pits, ripples, cones, and craters at the micron scale on the surface of the films [Keste and Messier, 1993]. During post-deposition annealing, hillocks may formed by stress relaxation processes associated with grain sliding and grain boundary diffusion if the annealing film is under stress [Nix, 1989].

2.2.3. Stresses in Thin Films

Stresses are often introduced from thin film fabrication processes and post-fabrication treatment. Stresses in thin films have important effects on many phenomena such as decohesion, defect generation and surface morphology evolution [Drory, Thouless and Evans, 1988; d'Heurle, 1989]. In the following, a review on stress classification, stress formation and stress evolution during post-deposition annealing is presented.

2.2.3.1. Classifications of Stresses

According to how they are created, stresses in thin film can be divided into two general categories: Extrinsic stresses and intrinsic stresses. While extrinsic stress results from differential thermal expansion coefficients, intrinsic stress is simply the rest, which is developed during the film growth process. In addition, stresses can also be divided into

three types according to their spatial homogeneity [Macherauch and Kloos, 1987]. The first, called macro stress, is nearly homogeneous across a large area (say, several grains) of a material, and are equilibrated within the whole body. The second kind of stress is nearly homogeneous across microscopic area (say, one grain or parts of a grain) of a material, and are equilibrated across a number of grains; The third kind of stress is inhomogeneous across submicroscopic area (several atomic distances within a grain) of a material, and are equilibrated across a small part of a grain.

Macroscopic stress generates by numerous ways. Any mechanical, thermal and chemical treatments, including elastic-plastic loading, machining, joining, forming, heat treatment and coating, cause macroscopic stress. In all cases, the resulting stress states strongly depends on the existing geometrical conditions and on the parameters of the treatments and processes applied. In elastic-plastic loading, some of the stress is vanished if the loading is released. However, residual stress may exist if an inhomogeneous deformation has undergone. In welding, the shrinkage of seams produces biaxial residual stress. As a special forming method, shot peening is widely used to produce compressive stress near the surface of the material, thereby to improve the hardness of material's surface.

Residual stress states of the second kind exist in both homogeneous and heterogeneous materials. For example, homogeneous materials with a pronounced anisotropy of the yield strength of their grains show residual grain stresses of different magnitudes after uniaxial elastic-plastic tensile deformation [Macherauch and Kloos, 1992]. Similar effects will occurs in heterogeneous materials composed of two phases with different yielding strengths.

The third kind of residual stresses is produced by lattice imperfections including dislocations, interstitial atoms, substitutional atoms, vacancies, microcracks, grain boundaries and phase boundaries. The submicroscopic stresses are associated with strongly inhomogeneous lattice strains. Very complicated stress states occur when stress

fields resulting from different types of lattice imperfections overlap. Experimentally it is hard to separate the third kind of stress from the others.

2.2.3.2. Thermal Stresses

Generation of thermal stresses are easy to understand. In general, thermal stress can be created by either non-uniform temperature change or uniform temperature change in the presence of differential thermal expansion coefficients. Rapid solidification of a liquid material, which results in a large temperature difference across the material during the process, creates considerable thermal stress even if the thermal expansion coefficient is the same across the material. The stress is generally inhomogeneous due to the complexity of the temperature field. For a thin film on a substrate, considering the situation that at a given time, the temperature is the same across the whole material, thermal stress is the same across the material and it can be quantitatively calculated if the temperature change and the difference in thermal expansion coefficient between film and substrate are known:

$$\Delta\sigma_{thermal} = \int_{T_i}^{T_f} \frac{E_f}{1-\nu_f} \cdot (\alpha_f - \alpha_s) dT \qquad (2.6)$$

Here T_s and T_f are starting temperature and finishing temperature, respectively; E_f is the elastic modulus of the film, ν_f is the Possion's ratio of the film, and α_f and α_s are thermal expansion coefficients of the film and the substrate, respectively. It is assumed that the stresses are biaxial, the substrate is rigid and much thicker than the film, and the film and substrate are elastically deformed. Because the temperature is the same anywhere in the sample, the stress is uniform across the sample. Therefore, thermal stress is basically macroscopic stress.

2.2.3.3. Intrinsic Stresses

While the origin of extrinsic stress is quite clear, that of intrinsic stress is much more complicated. No single model can explain how the intrinsic stress is created. Nevertheless, it is found that a number of mechanisms, such as nonequilibrium growth, defect evolution, interfacial constraint, *in-situ* phase transformation and *in-situ* stress relaxation are related to the sign and magnitude of the intrinsic stress. Each process is reviewed in the following.

Nonequilibrium Film Growth Intrinsic stresses observed in continuous metal films, if no bombardment-like process is involved during the film fabrication process, are generally tensile. Klokholm *et al.* [1968] and Buckel [1969] considered that the material was deposited in a metastable state and that subsequent atomic rearrangement (which would result in a shrinkage of the film if it were not attached to the substrate) generated the observed tensile stress. However, the as-deposited material need not be amorphous or have a metastable crystal structure. Other departures from the equilibrium can lead to stresses. For example, an excess vacancy concentration can result in tensile stresses by diffusion of the vacancies to the grain boundaries and annihilation there. It is noted that the stress results from the rearrangement of the depositing atoms after they arrive to the substrate. If the films is not allowed to change structurally, but maintains its 'frozen-in' structure, no stress is expected to develop.

In order to predict the stress generation in thin films at various substrate temperatures, it is important to consider the kinetic process involved. There are three major aspects of stress generation wherein the kinetics of atomic motion should be considered. The first involves the rate of atomic rearrangement on the growing surface. It this occurs rapidly compared to the rate of arrival of depositing atoms then an equilibrium structure will be formed and the film will grow in a stress-free state. Conversely, if the depositing atoms arrive more rapidly than they rearrange, a nonequilibrium structure will be formed.

Subsequent rearrangement of the structure leads to stress in the film. In this case, the kinetics of the atomic rearrangement must be considered, and deposition temperature seems to be crucial. Buckel [1969] showed stress-free growth of amorphous Ga and Bi below 20 K. At these low temperatures, stress generation is limited by the low atomic mobility. Klokholm [1969] and Rottmayer and Hoffman [1971] showed an increasing stress with increased deposition temperature.

The third aspect of stress generation that requires kinetic considerations involves stress relaxation, *i.e.*, *in-situ* relaxation. Since stresses as high as the flow stress are observed during thin film growth [Klokholm and Berry, 1968; Plunkett *et al.*, 1979], dislocation motion as well as diffusional process can operate to reduce the stress. The observed stress depends on the rate of stress generation associated with atomic rearrangement relative to the rate of stress relaxation rate. Since diffusional stress relaxation involves the mass transport of material from surface or the substrate/film interface to the interior, stress generation due to local atomic rearrangement is likely to proceed faster than stress relaxation. However, if the stresses are high enough, stress relaxation may occur rapidly through dislocation motion.

Grain Growth One type of atomic rearrangement that can be responsible for generating tensile stresses is grain growth [Chaudhari, 1972]. It is believed that the grain boundary density is less than that of the perfect lattice and a strain in the film due to the elimination of grain boundaries will result. Doerner and Nix [1989], based on the observation that the grain growth decreased the grain boundary energy but at the same time, increased the elastic energy, kinetically analyzed the grain growth and grain-growth induced stress evolution. They concluded that the grain growth stops when the grain size reaches a critical size, and the smaller the initial grain size is, the more significantly the stress changes by grain growth. According to their calculation for Ni films, when the initial grain size is less than 20 nm, more than 20 MPa stress can be developed before the

grain size reaches the critical size. Nearly 2 GPa tensile stress can develop when the initial grain size is 2 nm. However, such high stress was rarely observed because stress relaxation becomes significant at this time.

Excess Vacancy Annihilation Another source of stress generation in thin films involves the annihilation of excess vacancies. In general, volume changes are associated with the annihilation of vacancies and these volume changes lead to stresses in the film when the film is attached to a substrate. The sign and magnitude of the stress produced depend both on the vacancy volume and on the site of vacancy annihilation. If the vacancies annihilate at the free surface of the film, or at the surfaces of internal cavities, no additional stress is expected because the planar dimension of the film does not change. However, if the vacancies annihilate at grain boundaries perpendicular to the plane of the film, a biaxial tensile stress develops within the film. The initial vacancy fraction, average grain size and the temperature determine how much stress can result. According to the calculation results by Doerner and Nix [1989], if the initial vacancy fraction of 1% and a grain size of 30 nm are assumed for Ni film, the stress magnitude in the MPa range is not observed for holding time as long as ~10^3 seconds at temperature below 473 K. Therefore, it appears unlikely that vacancy diffusion contributes significantly to stress generation for low temperature deposition.

Grain Boundary Relaxation One of the most widely quoted models of intrinsic stress is Hoffman's grain-boundary relaxation model [Hoffman, 1966, 1976; Doljack and Hoffman, 1972; Pulker, 1982]. According to the model, tensile stresses are created in thin metal films because the crystallites that form on the substrate are never located in the correct positions to produce equilibrium grain boundaries when the crystals grow together. It is argued that, on average, the atoms in the grain boundary are more widely spaced than they would be if the crystals were free to form an equilibrium boundary. As the atoms relax

toward their equilibrium positions, an elastic strain and a corresponding intrinsic tensile stress develops in the film. Under these conditions the equilibrium state of the film is not a stress-free state. Rather, the total free energy of the system, including both interfacial ands elastic strain energy, reaches a minimum at a finite elastic strain.

Even though some ideas from Hoffman's model are open to question [Doerner and Nix, 1989], it is clear that, on average, an atomic deficiency will exist in the grain boundaries due to the arbitrary location of the crystallites on the substrate. Atoms will be added to each growing crystal until they grow together. When the spacing between the surfaces of two separately growing crystals approaches an atomic dimension it becomes more and more difficult for arriving atoms to reach sites between the two crystals. This naturally leads to the porosity of the film. Even the porosity in the grain boundary does not automatically lead to elastic strains in the film, subsequent relaxation process may result in the development of stress.

Impurity Effects The effect of impurities on the stress is not well understood. However, oxygen incorporation is thought to be probably the most significant in changing film stresses. In films deposited by vacuum evaporation, intrinsic compressive stress were observed when the vacuum conditions were poor [Priest *et al.*, 1962; d'Heurle *et al.*, 1968], and the intrinsic stress can change from tensile to compressive if the oxygen level is increased [d'Heurle, 1989]. The mechanism appears to be that the impurity atoms are first absorbed at the surface of the films being deposited and diffuse to the interior. Clearly, this process could happen with materials which have a high affinity for carbon, oxygen, and high solubility limits for these elements. Moreover, these elements occupy interstitial positions, causing an increase in lattice parameter, and diffuse readily. Another possible process is that the impurity atoms are adsorbed on the film surface and get buried under an upper layer of metal, thereby swelling the lattice and causing compressive stress.

Phase Transformation and Precipitation Volume changes associated with phase transformation and particle precipitation also lead to stress generation in thin films. For example, amorphous-to-crystalline transformation often results in a 1 to 2% increase in density [Davis, 1978], it is expected that large tensile stress can develop by crystallization. This effect is observed for a number of materials [Horikoshi *et al.*, 1963; Pan and Belch, 1984]. Stress associated with the precipitation of additional phases have been observed although the effect is smaller [Zingu and Mofokeng, 1993].

Epitaxy Strain can be introduced into a growing film if the film grows with an epitaxial relationship to the substrate and a mismatch between the lattice spacings of the two materials exist. As the thickness of the epitaxial layer increases, the strain energy in the film increases until it becomes more energetically favorable for a series of misfit dislocations to form at the interface. A critical thickness thus exists, below which the coherent strained film is stable and above which an array of misfit dislocations forms to accommodate the lattice mismatch. In this consideration, stress in films quickly decrease when the thickness reaches the critical thickness.

Stress in Sputtered Films In contrast with films deposited by evaporation which usually display tensile stresses, compressive intrinsic stresses are often observed in sputtered films [Blachman, 1974; Thourton and Hoffman, 1977 (a, b); 1980; 1982]. Because such films also contain some amount (~1.0 at% or less) of incorporated gas, many references imply that this incorporated gas is the cause of the unexpected (compared with film deposition by evaporation) compressive stress. But it is not the actual case. It was first pointed out in a study of aluminum films deposited by d.c. sputtering that [d'Heurle, 1970], while in evaporation the deposited atoms are nearly in thermal equilibrium with an energy equal to a few *kT*s, in a sputtering process, a flux of depositing atoms and the ion gas atoms reflected from the sputter cathode arrive on the substrate with an energy of

several electron volts, so that the already deposited layers are subjected to a bombardment which in an atomic scale is similar to the 'shot peening' effect which in metallurgical fabrication is used to put surfaces into compression. It does not matter so much that the energy should be so small since the damage is immediately buried under newly deposited layers, but rather that the damage is accumulated. The effect is increased under conditions of bias sputtering when the substrate is deliberately bombarded with energetic gas ions. In addition, the compressive stress generated in the deposited films is dependent on other sputtering condition such as sputtering gas pressure, power, geometry of the relative atomic mass of the target material to the atomic mass of the working gas [Thornton, Tabock and Hoffman, 1979; Hoffman and Thornton, 1980]. It is particularly noted that this peening effect mechanism is predominant only when working-gas pressure is low, since over-dense working gas can dissipate the kinetic energy of the gas atoms reflected from the sputter cathode.

2.2.3.4. Stress Relaxation

Stress relaxation may occur during deposition, in which case it is referred to as *in-situ* relaxation, or it may occur during post-deposition annealing. All the relaxation processes happening during the deposition such as structure relaxation, grain growth, excess vacancy annihilation, grain boundary relaxation and phase transformation, can also occur during post-deposition annealing. However, because the holding time can be very long during post-deposition annealing, some mechanisms unavailable during *in-situ* relaxation can also happen by post-deposition relaxation and have significant effects on morphology, microstructure and properties of films.

Grain boundary slide is well observed mechanism for stress relaxation. It occurs when films are under compressive stresses. By this mechanism, grains can be extruded from the film surface, whereby hillocks are formed. The formation of hillock stop when the compressive stress is completely relaxed. When the film is under tensile stress,

hillocks can slide back into the film by which the tensile stress is relaxed. Therefore, to a limited degree, hillock formation is reversible.

It is pointed out that stress relaxation in thin films can proceed along different pathways [Gangulee, 1974]. Dislocation motion can take place and be observed at the surface through the formation of visible slip lines [Caswell, Priest and Budo, 1963]. Creep either by lattice diffusion model (Nabarro and Herring creep) or by grain boundary diffusion (Coble creep) is also a means of relaxing film stresses. Based on the level of stress and the temperature, it can be defined which process will be operative [Murakami, 1984]. According to the model proposed by Murakami, dislocation glide and climb occur at high stress (~ 10^{-2}G, where G is shear modulus) and high temperature (T/T_m >0.5), and gives a strain rate as high as 0.1 s^{-1}. Grain boundary diffusion occurs at an homologous temperature (T/T_m) above 0.4 and gives a strain rate of 10^{-2} to 10^{-10} s^{-1}.

For bulk materials, stress relaxation by grain boundaries dominates over bulk diffusion (lattice diffusion) for small grain sizes and in an intermediate temperature range (0.3 ~ 0.6 T/T_m). Since the grain sizes in thin films are typically small, grain boundary diffusion is an important mechanism in thin film deformation. However, both the constraint of the substrate and the columnar microstructure of thin films place significant limitations on the grain boundary diffusion process [Jackson and Li, 1982]. Once the normal stress on the grain boundaries have been completely relaxed, grain boundary diffusion related stress relaxation stops. Therefore, In the absence of bulk diffusion or dislocation motion, stress within the grains will remain due to the substrate constraint.

In summary, for thin films on substrate, while extrinsic stress is easy understood, origin of intrinsic stress is much complicated. A number of mechanisms may contribute to the development of intrinsic stress. Stress relaxation in thin films is also determined by several processes. Which one is operative depends on the stress level and temperatures. Stress relaxation in thin film may differ from that in bulk materials because of the constraint of the substrate.

2.3. NiTi Thin Films

Based on the remarkable performance of melt-solidified NiTi alloy, thin film NiTi has been regarded as a promising material for high-energy-output microactuators for use in microelectromechanical system and has been extensively studied. Considerable progress toward engineering application has been achieved. Below is presented a review on NiTi film fabrication, microstructure, phase transformations, shape-memory effect of sputtered NiTi, and current research interests of NiTi thin films.

2.3.1. Fabrication of NiTi Thin Films

While some work of NiTi thin films were mainly directed at studies of solid state reaction between Ni and Ti, in which case multilayer NiTi was made by sputtering [Clemens, 1986; Jongste *et al.*, 1988; Scineider *et al.*, 1989], or electron beam vaporization [Meng *et al.*, 1987], most work aimed at the preparation of SMA NiTi thin films. Physical vapor deposition techniques, such as sputtering [Kim, Moine and Stevenson, 1986; Rai and Bhattacharya, 1987; Busch, Johnson, Hodgson, Lee and Stevenson, 1990 (b)], thermal evaporation [Gabraud and Delage, 1991; Moine, Delage, Petton and Sinclair, 1992], ion mixing [Zheng and Dodd, 1994; Krulevitch *et al.*, 1996] and ion-beam assisted deposition [Walles, Chang and Grummon, *et al.*, 1992] have been used to make NiTi films. Due to the flexibility of target materials, sputtering, including d.c. magnetron sputtering, r.f. sputtering, triode sputtering, and ion-assisted sputtering, have been widely used in the preparation of near-equiatomic NiTi films.

The composition of resultant films is of concern because it is very important for SME and transformation temperature control. It has been repeatedly shown that the composition of sputtered NiTi films may deviate from that of the sputter cathode material. For example, when an equiatomic NiTi target is used, the as-sputtered films have roughly a composition 51~54 at.%Ni [Johnson, Martynov and Minners, 1995]. The reason is,

compared to Ni, Ti is a preferentially resputtered species. The actual composition of films depends on processing parameters such working gas pressure, working distance, plasma energy and off-axis orientation, as well as target geometric configuration that may change as sputtering proceeds. Lee [1994] tentatively established the relationship between the composition of film and some of the process parameters. According to Lee, at 200 W deposition power, steady-state composition of films can be achieved only after one-hour's presputtering and is lost if the deposition time exceeds 3 hours. In addition, higher plasma energy makes the film more Ni rich, and the composition at off-axis site (1" from the center) in the film is less prone to change with the deposition power than on-axis composition. More recently, Bendahan *et al.* [1995], having demonstrated that the film composition was sensitive to the product of sputtering gas pressure and the working distance, invented a method to control the composition by changing the pressure, which is directed by the *in-situ* measurement of sputtering plasma composition by optical emission spectroscopy. Another method to realize composition control is dual-source sputtering. By making multilayer Ti-rich films, Chang and Grummon [1992, 1997] were able to control the composition by alternating exposure of the substrate to two cathodes (NiTi and Ti). For the multilayer films, good composition homogeneity can be achieved by post-deposition annealing. However, a popular and easy way to roughly compensate the preferential re-sputtering effect is to put a few additional small plate pieces of the pure element to be augmented on the surface of sputtering cathode [Kawamura *et al.*, 1995; Ishida *et al.*, 1995]. No quantitative composition compensation can be expected by this method.

Other qualities such as compactness and brittleness also depend on the deposition parameters used. The most important parameters are working-gas pressure and substrate temperature during deposition. It seems that lower working gas pressure (<10 mTorr) and higher substrate temperature are beneficial to improve the compactness and ductility of the films. However, the compactness and mechanical properties of the films are related to the

structure and microstructure, which may be also modified by post-deposition treatment. The following discuss the structure, microstructure and transformations of NiTi films at as-deposited state and by post-deposition annealing.

2.3.2. Structure, Microstructure and Transformations of NiTi Thin Films

In spite of different fabrication methods, NiTi thin films prepared without additional substrate heating are usually amorphous. This is probably due to the limited diffusion rate at ambient temperature since crystalline TiNi is highly ordered and atomic rearrangement is needed to produce crystalline structure. In crystalline B2 NiTi, the diffusion rate of Ti atoms is approximately one order of magnitude lower than that of Ni atoms [Bastin and Rieck, 1974]. Although at present there is no diffusion rate data of Ti in amorphous TiNi, it can be deduced, from the studies in Ni-Zr system [Johnson, 1988] due to the similarity between Ni-Ti and Ni-Zr, that Ti is a relative immobile species in amorphous NiTi, too. Due to the small free energy gap between amorphous and crystalline phase [Schwarz *et al.*, 1985], and the sluggish diffusion of Ti, The amorphous structure stays stable until crystallization temperature.

Amorphous-to-crystalline transformation of NiTi films occurs at temperatures 673 K [Nakata *et al.*, 1995] or above [Johnson, 1990], depending on film composition [Buschow, 1984; Kim, Moire and Steveson, 1986; Chang and Grummon, 1997], and the heating rate of isochronal annealing [Kissinger, 1957; Chang and Grummon, 1997], with a crystallization enthalpy as low as 1.9 kJ/mol [Busch, Johnson, Hodgson, Lee and Stevenson, 1990(b)]. It is also reported that cold-work of the amorphous NiTi films can lower the crystallization temperature to 623 K [Madsen and Jardine, 1993]. Since atomic rearrangement is needed for transformation of disordered structure to ordered structure, the crystallization is an activated process. Chang and Grummon obtained crystallization activation energies of 385 ± 6 kJ/mol and 501 ± 6 kJ/mol for $Ti_{51}Ni_{44.4}Cu_{4.6}$ and $Ti_{44.7}Ni_{46.5}Cu_{6.1}$ films, respectively.

The crystallization of amorphous NiTi films results in B2 structure and some second phases, depending on whether the film is Ti-rich or Ni-rich. Kim *et al.* [Kim, Moire and Steveson, 1986] studied the crystallization behaviors of magnetron sputtered $Ni_{56}Ti_{44}$ by Differential Scanning Calorimetry (DSC) and Transmission Electron Microscopy (TEM), concluding that the crystallization temperature was 791 K and the crystallization sequence was:

$$NiTi(Amorphous) \rightarrow Ni_4Ti_3 \rightarrow \beta_1(NiTi) + Ni_4Ti_3 \rightarrow \beta_2(NiTi) + Ni_3Ti_2 \qquad (2.7)$$

where β phases are the equilibrium crystalline B2 phases when the precipitates exist.

Ishida *et al.* observed the microstructure of 523 K-deposited $Ti_{51.8}Ni_{48.2}$ films annealed at different temperatures. When the films were annealed at temperatures lower than 973 K, the lower-temperature annealed samples contained Ti_2Ni precipitates inside the B2 grains, which was significantly different from the melt-solidified Ti-rich NiTi, where for as-cast and as-solution-treated samples the Ti_2Ni precipitates appeared along grain boundaries. The fine in-grain precipitates significantly affect the shape memory effect of Ti-rich films [Ishida, Sato, Takei and Miyazaki, 1995].

Hot-substrate sputtering is a way to obtain crystalline NiTi films directly. It has been showed that when the substrate temperature is higher than 673 K, the as-deposited films are composed of B2 NiTi and some second phases [Ikuta *et al.*, 1990; Hou, 1997]. By observing the microstructure of the NiTi films deposited at various temperatures on quartz, Hou established the relationship between the microstructure of the film and the deposition temperature (T_d). When $T_d < 573$ K, the film usually is amorphous with columnar structure. At $573\ K < T_d < 673$ K, the film usually has a mixed structure containing both amorphous structure and B2 crystalline structure, and possibly with some fine Ni_4Ti_3 precipitates. At $T_d > 673$ K, the film is almost fully crystalline with large Ni_4Ti_3 precipitates, and the grains become larger. Hou also discovered that a thin layer of

amorphous NiTi, near which is nanoscale B2 grains in the NiTi side, exists at the interface between the quartz substrate and the crystalline NiTi even when the deposition temperature exceeds 723 K, and a strong (110) texture in the as-deposited crystalline film. Later work by Chang [1997] indicated that the stiffness of the substrate may affect the minimum substrate temperature for fully crystalline NiTi, and working gas pressure also affect the texture of the as-deposited film. According to Chang, with Kapton polyimide substrates, whose elastic modulus is only ~1.4 GPa [Product Bulletin, Du Pont Co.] in contrast to ~72 GPa for quartz [Engineered Materials Handbook, 1993], fully crystalline NiTi films can be obtained at substrate temperature as low as 560 K. At deposition conditions of lower working gas pressure (~4.5 mTorr) with high deposition power (200 W for 2" gun), or high pressure (~6.0 mTorr) with low deposition power (<100 W), strong (110) texture was observed in as-deposited NiTi on Kapton.

Near-equiatomic crystalline NiTi films, obtained either by post-deposition annealing or by hot-substrate deposition, have been demonstrated to undergo the B2 → R and R → B19' or B2 → B19' transformations upon cooling and the martensite transforms back to austenite upon heating, which is basically the same processes as occur in melt-solidified NiTi SMAs, and therefore, the crystalline films have SME and PE comparable to those in melt-solidified NiTi [Busch, Johnson, Lee and Stevenson, 1990; Ikuta *et al.*, 1990; Kuribayashi *et al.*, 1990; Walker *et al.*, 1990; Johnson, 1991; Chang and Grummon, 1992; Ishida *et al.*, 1993; Miyazaki and Ishida, 1994; Hou and Grummon, 1995; Hua, Su and Wuttig, 1995]. Both the R-phase and martensitic transformations are observed by resistivity measurement and DSC measurement. It has been shown that free-standing crystalline B2 NiTi films have comparable SME and PE with their melt-solidified counterpart. Ishida *et al.* [1996] studied the annealing effect of Ni-rich NiTi on the recoverable strain from the martensitic transformation and austenite critical stress for slip deformation, and concluded that coherent Ni_4Ti_3 precipitates, which may be lost by elevated annealing temperature (> 623 K) or prolonged time, help to maintain high stress

(> 580 MPa) for inducing slip deformation and larger recoverable strain (~5%). The same group [1995] also found that fine Ti_2Ni precipitates may exist inside the grains of annealed films with annealing temperature lower than 973 K, therefore, the mechanical properties of the films were improved. Ti_2Ni precipitates depressed the martensitic transformation so the R-phase transformation was separated, making a two-stage transformation during cooling from austenite. Hou and Grummon [1995] demonstrated that crystalline NiTi films also have superelasticity resulting from stress induced martensitic transformation, which is the same as occurring in melt-solidified NiTi alloys.

The martensitic transformation in NiTi/Si composite has been studied by Kim [1994]. It was shown that substrate constraint may suppress the martensitic transformation. The martensitic transformation can be completely suppressed if the thickness ratio between the film and Si substrate is too small. The stress output for reverse martensitic transformation is also related to the thickness ratio as well as substrate rigidity [Mathews *et al.*, 1996]. This result is useful in design of NiTi/Si microactuators.

2.3.3. Current Application-Oriented Work

Melt-solidified NiTi SMAs have found many successful applications in industry as well as in biomedical practice. Some of the applications use SME while others use their superelasticity. However, major work on NiTi thin films has been aiming at the development of Si-based SMA microactuators. The new microactuators will have advantage over many of the actuators currently available, which are based on piezoelectric or electrostatic principles [Fan *et al.*, 1989; Kim, Katsurai and Fujita, 1989], in that their energy density output is one or more orders of magnitude larger (see Table 1-1). Si substrates are used because they compatible with other electronic fabrication processes, and more important, it serves as a good heat sink to allow the SMA actuators operate at higher frequency (> 1 kHz) [Kim, 1994]. Busch and Johnson [1990] proposed the first NiTi SMA microactuator. Ray and his coworkers [Ray *et al.*, 1992] invented a SMA microvalve

made from thin film NiTi. More recently, Krulevitch *et al.* [1996], having demonstrated the reversibility of ~500 MPa stress relief/recovery of NiTiCu on Si, proposed a Si-based microgripper model and a Si-based electromicroactuator model [Ashley, 1996]. Also, latest work in our laboratory demonstrated that Ni-rich binary films on Si may relieve as large as 700 MPa stress upon the R-phase and martensitic transformations and the stress may perfectly recovered by the shape memory effect, which results in useful cyclic displacement [Zhang and Grummon, 1996].

Another novel application of SMA NiTi thin films was suggested by Jardine [Jardine, 1990; Mercado and Jardine, 1995]. It is a ferroelastic -SMA heterostructure produced by depositing of $BaTiO_3$ onto NiTi free standing film. This heterostructure is expected to be able to perform sensing and actuation simultaneously. Recently, Alam *et al.* [1997] prepared a TiNi ferroelastic-ferroelectric thin film heterostructure by hot depositing NiTi on Si with $BaTiO_3$ and PZT buffer layers. The buffer layers improved the crystallinity of NiTi films.

A number of other heterostructures are of industrial interest. One of them is to fabricate SMA NiTi on Kapton, a base material widely used in electronics. Depositing SMA films on Kapton is potentially useful to realize shape change or displacement driven by temperature change and the biasing force of Kapton layer. The difficulty is that although the final decomposition temperature of Kapton is 833 K, which is higher than the crystallization of amorphous NiTi, when annealed at temperature as low as 723 K in vacuum Kapton become unstable. Therefore, post-deposition annealing may not suitable to produce crystalline NiTi/Kapton bilayer structure. Hot-substrate deposition may be a solution. Grummon *et al.* [Grummon, Hou, Zhao and Pence, 1995] demonstrated that NiTi films deposited at elevated temperatures (~673 K) on Kapton was capable of performing SME with the polyimide left intact. However, there arise other problems such as transformation temperatures which are too low for most practical applications, which is probably due to the nanoscale grain size. Thus it would be interesting to deposit SMA NiTi

films on Kapton that have an M_s near room temperature, which is possible by making Ti-rich or stoichiometric NiTi films. Another interest arising from the NiTi/polyimide heterostructure is that the polyimide is a good elastic layer which can offer large displacements due to its good ductility (~40%) and small elastic modulus (~1.4 GPa).

Just like binary melt-solidified NiTi, binary NiTi thin films also suffer from low transformation temperatures. High-transformation-temperature SMAs are of interest. Johnson *et al.* [Johnson, Valery, Martynov and Shahoian, 1995] compared three high-temperature SMA films, CuAlNi, FeNiCoTi and TiNi-Hf, and concluded that, of these candidates, TiNi-Hf had the best SME and the best mechanical properties. By substituting 15% of Hf for Ti, the M_s temperature increased to 473 K, but the recoverable strain was still kept at 4%. Almost concurrently, Miyazaki's *et al.* [Miyazaki, Hashinoga, Yumikura, Hirikawa, Ueki and Ishida, 1995] reported their results of r.f. sputtered TiNi-Pd films and Quandt *et al.* [1995] reported theirs of d.c. magnetron sputtered TiNi-Pd films, and they independently showed that the M_s temperature reached 473 K by substituting 20 at.% to 30 at.% Pd for Ni and concluded that the NiTiPd films were also a promising high-temperature SMA candidate. However, it has also been indicated that the transformation temperature is sensitive to a small composition deviation, especially when the composition falls on the Ni-rich side [Angst *et al.*, 1995]. How to precisely control the composition to ensure precise control of transformation temperature remains a challenging work.

Sputtering has been favored for creating a small-area NiTi films. However, thermal evaporation makes lower cost films over large areas. The problem is, although it is possible to use hot substrates to create crystalline NiTi, which is analogous to sputtering deposition, the composition can be even harder to predict due to the large vapor pressure difference between Ni and Ti. Using equiatomic NiTi as parent alloy may produce composition far away from stoichiometry. Furthermore, and diffusion at high temperatures in the parent alloy makes the frontier composition change with the time. Possible solutions

include the use of parent alloy composition adjustment and the flash evaporation method. No attempts have been published using these methods.

Slow response remains a big problem for thermal induced actuation using SMA even though thin film components on Si can considerably shorten the response time. A novel idea is to develop magnetically induced SME, which allows actuation frequency to reach MHz. While James *et al.* [1997] have claimed success in searching for this kind of material and have developed a theory regarding the magnetically induced martensitic transformation, Ullakko *et al.* [1997] have reported that a recoverable strain of 0.15% produced by the reorientation of magnetically induced martensite variants occurred in Ni_2MnGa. However, much work needs to be done to increase the magnitude of reversible strain.

Despite all difficulties and limitations, Si-based SMA microactuators remain an exciting and promising application of NiTi thin films. In fabricating this kind of microactuator, stresses, either intrinsic or extrinsic, will play an important role in reversible action. This thesis research encompasses stress development during thin film fabrication, stress evolution in response to temperature changes, stress stability during annealing and stress relaxation during the R-phase and martensitic transformations for NiTi thin films on Si.

Chapter 3

EXPERIMENTAL METHODS

Work reported in this thesis includes film fabrication, stress analysis, phase transformation analysis and relevant structure and microstructure investigation. Various experimental methods have been used. In this section, the experiment procedures are detailed.

3.1. Thin Film Fabrication

NiTi thin films were made by the planar d.c. magnetron sputtering method using deposition apparatus constructed in our research laboratory at MSM department of Michigan State University [Hou, 1997]. A schematic representation of the apparatus is shown in Fig. 3-1. It is composed of a 2-inch magnetron gun, substrate holder and external heating devices, housed in a deposition chamber that can be evacuated to 10^{-7} torr by a Welch 1397 rotary pump and a 4000 L/s Varian HS - 10 diffusion pump. Pure Ar was used as the working gas. Pressure was controlled by an MKS 246 mass-flow controller and measured by an MKS Baratron capacitance manometer.

Two target alloys, Ni-rich and Ti-rich near-equiatomic TiNi ingots, were supplied by Special Metals in New York. The Ni-rich ingot had a nominal composition of 51.3%Ni - 48.7% Ti in atomic percent, while the Ti-rich alloy was 49.6%Ni - 50.4%Ti, the former having a nominal M_s of 263 K and latter having a nominal A_s of 366 K, respectively. The targets, which had a diameter of 2 inches and a thickness of 0.25 inches, were cut by Electro Discharge Machining (EDM) from the as-supplied ingots. In addition, a composite

target was used to produce Ti-rich films. It was made by evenly inserting four 0.125 inch pure Ti rods within the wear track of a new Ti-rich target.

Two substrate materials were used in this study. One was single crystal Si with (100) orientation, single-side polished, 5.1 mm (2 inches) in diameter and 0.3 mm in thickness, supplied by Virginia Semiconductors; the other was microscope glass slides with dimensions of 1 mm x 25 mm x 76 mm. The main purpose of using glass substrates here was to produce free-standing films since the films are easily peeled off from the glass substrates, especially when the film/substrate sample was thermally shocked by repeatedly immersing in liquid nitrogen.

Films have been made both with and without external heating. When external heating was used, two separate heating elements were placed with one on each side of the substrate. Substrate temperature was monitored by two thermocouples placed on each side of the substrate. Temperature was regarded to be in equilibrium when both thermocouple readings were stable and very close (difference < 2 K).

Deposition was started with a base vacuum pressure better than 5 x 10^{-6} torr. In order to ensure a mass flux with stable composition, each new target was worn-in for approximately 7 hours before sputtering onto the substrate. 20 min full-power pre-sputtering was also performed at the beginning of each run before the substrate was exposed. For all depositions, the working distance was 65 mm, Ar pressure was set at a carefully controlled level between 3.5 mTorr to 7 mTorr, and the deposition power was set at level between 50 W to 200 W. In the case of hot-substrate deposition, the system was outgassed at 50 K above the planned deposition temperature for 12 hours prior to deposition. As-sputtered films usually experienced furnace cooling at a rate of 20 ~ 40 K/min.

3.2. Thin Film Characterization

3.2.1. Thickness Measurement

Film thickness was initially measured by scanning over deposition steps created by masking (usually near the edge) using a Dektak IIA profilometer at Department of Physics and Astronomy of Michigan State University. Since there was no film in the masked region, the step heights were regarded as the film thickness. To ensure the best accuracy, the slowest scanning speed (~ 1 mm/min) was always used.

The deposition rate is nearly proportional to power used in sputtering, while high deposition temperature or lower working gas pressure tends to decrease the deposition rate. Based on the thickness measured by profilometry, at 200 W, 5.0 mTorr pressure and ambient deposition, a typical sputtering rate was ~1 nm/sec.

3.2.2. Stress Measurement

Stresses in films fabricated under different conditions were evaluated by the wafer-curvature method using Stoney's equation [Hoffman, 1966; Ohring, 1992] which gives the films stress, σ_f, as:

$$\sigma_f = \frac{E_s}{6(1-\nu_s)} \cdot \frac{t_s^2}{t_f} \cdot \frac{1}{R} \qquad (3.1)$$

where: E_s is the elastic modulus of substrate;

ν_s is the Poisson's ratio of the substrate;

t_s and t_f are the thicknesses of substrate and film, respectively, and

R is the curvature radius of the film-substrate composite.

This equation is valid if $t_s \gg t_f$ for a wide variety of shapes of the film-substrate composite [von Preissig, 1989].

The stress measurement system, which is schematically shown in Fig. 3-2, was designed and constructed in our laboratory at MSM department of Michigan State University [Zhao, 1995]. The system was composed of a laser scanning system driven by an Omega PLC 812-PG card which was installed on a CompuAnd 333 computer, a quartz bell-jar that was evacuated down to 10^{-8} torr by an Alcatel TM800 turbomolecular pump and a Franklin Electric roughing pump, and an external furnace that was controlled by a CN8600 Omega temperature controller. The temperature was monitored by a thermocouple which was placed near the wafer. A pure Ti getter was used in order to minimize oxidation at high temperature. Heating was performed at rates ranging from 1.5 K/min to 3.0 K/min by programming the Omega controller and adjusting the power input of the furnace, while cooling was performed at rates lower than 5 K/min to ensure the homogeneous temperature field inside the chamber by slowly introducing cold nitrogen gas into the chamber.

A laser scanning system was used to measure the curvature of film-substrate composite. The optical diagram is shown in Fig. 3-3. The curvature, C, was calculated from the linearly fitted displacement for one scan step by

$$C = \frac{1}{R} = \frac{d}{2Df} \qquad (3.2)$$

where d is the beam displacement for one scanning step measured by Position Sensitive Detector (PSD), D is the beam displacement for one scanning step at the sample surface, and f is the focal length of the lens, which was 1,000 mm in this experiment.

The curvature values from the optical method were compared with that obtained from the height-measurement method by profilometry. Two samples were used to perform calibration. By profilometry, the first one was measured to have a positive curvature radius of 18.71 m, and the other has a negative curvature radius of -15.25 m. The calibration of the laser scanning apparatus was completed by adjusting the gains of the amplifiers for the signals from PSD and the distance between the optical lens and the pedestal on which

rotating mirror and PSD were placed. After calibration, the curvature radii obtained by laser scanning apparatus were 19.03 m and -14.95 m for the positively curved and negatively curved samples, respectively.

Because the wafers were not perfectly flat in the as-supplied condition,[3] considerable error may result from the extra curvature, especially when the stress is low. Therefore, the initial curvature of each as-supplied wafer was measured. When calculating the stress, the curvature of the original wafer was subtracted.

Error in stress measurement may also partly result from the non-uniformity of film thickness, which produces an additional convex curvature. Since the film is usually thicker at the center than at the rim, negative curvature usually results (which corresponds to a compressive stress). This corresponding curvature C_{film} can be calculated by

$$C_{film} = \frac{1}{R} = \frac{2t_f x}{R^2_{wafer}} \qquad (3.3)$$

where R is the curvature radius resulting from the non-uniformity of film thickness, R_{wafer} is the radius of wafer (25.4 mm), t_f is the average thickness of the film, and x is the thickness deviation between that at the center and the rim (approximately 3% according to the manufacturer for 2" gun depositing on a 2" substrate). The stress error can be calculated by combining equations (3.1) and (3.3) and gives 0.25 MPa, which is comparable to the sensitivity of the laser apparatus [Zhao, 1995]. Therefore, the error from the non-uniformity of film thickness is negligible.

3.2.3. Thermal Treatment

Post-deposition thermal treatment was sometimes necessary to acquire the shape memory effect, to get better mechanical properties, and to modify phase transformation characteristics of as-sputtered NiTi films. All the post-deposition anneals were conducted

[3] Polishing usually introduces slight doming of the wafer.

in the vacuum bell-jar used for stress measurement. The system was evacuated to 10^{-8} torr. The heating rate usually 2 K/min. As-annealed samples usually experienced furnace cooling, which typically was of a rate 10 ~ 20 K/min at temperatures above 573 K, or vacuum (radiative) cooling by removing the furnace, which typically was of a rate of 100 ~ 50 K/min at temperatures above 573 K. Pure Ti getters were also used to decrease residual oxygen level.

3.2.4. Transformation Temperature Measurement

Transformation temperatures were obtained by four-probe electric resistivity measurement. A schematic diagram of the apparatus used in this experiment is shown in Fig. 3-4. 0 ~ 15 V voltage (0 ~ 6 W in power, 0 ~ 0.4 A in current) was supplied by an HP 6010A DC supply to a 38 Ω heating tape to heat the films while cold nitrogen gas was introduced to cool the sample. Two 12 V alkaline batteries and a 3 kΩ resistor connected in series with the tested sample (~1 mm wide, ~10 mm long) were used to form a closed circuit. The voltage drop across the sample, which was proportional to the resistance, and output of the thermocouple, which gave temperature readings, were recorded on an HP 17171A chart recorder. The transformation temperatures were derived from resistivity-temperature curves by the tangential-line method. In order to achieve good temperature homogeneity and to obtain reliable temperature readings, both heating and cooling rates were less than 1 K/min.

In some experiments, the resistivity of NiTi films on Si was measured *in-situ* during the stress measurement. In this case, two ~300 nm thick gold squares (3 mm x 3 mm) were sputter-deposited on NiTi side using a pure gold cathode to ensure a good electric contact. The wafer was connected in series with a 3 kΩ resistor and 20 V DC supply through the two gold-layer squares. The voltage between the two gold layer squares was send to an Omega OMNI AMP™ II instrumentation amplifier (x10 ~ 1000) followed by an A/D conversion by an Omega PLC 812-PG card. As a result, the voltage

of the sample, which was proportional to the resistivity, was recorded in digital form (0~4096). By a QuickBasic program, the resistivity and the curvature of NiTi/Si samples were recorded simultaneously, making it possible to relate stress variation to phase transformations.

3.2.5. Composition Analyses

The chemical composition was analyzed by a LINK AN - 10000 X-ray EDS (Energy Dispersive Spectrum) system on a JEOL S - 2500 Scanning Electron Microscope (SEM) operated at 20 kV. Gain calibration was made on Co-Kα radiation and bulk calibration was made using LINK ZAF4 code. The test films were usually ~ 5 μm thick, and were attached to Si wafers or glass substrates. Since no Si X-ray peaks were observed, the substrate was taken to have no interaction with electrons, and thus the spectra could be processed by a ZAF correction. The composition was recorded as the average of at least 5 nearby points.

3.2.6. Structure and Microstructure Analyses

Phase identification was conducted by X-ray diffraction using a SCINTAG-2000 diffractometer with accelerating voltage of 35 kV, tube current of 25 mA, Cu-K_α radiation, and 2θ scanning mode. The scan step was 0.03 °/step, scan rate was 2 °/min and scan range (2θ) is 20 ° ~ 80 °. Glass substrates were usually used in order to avoid extraneous X-ray peaks. However, it was found that when films were thicker than 3 μm, no substrate peaks were observed. Most X-ray diffraction experiments were performed at ambient temperature. In some special cases, resistive heating was used to the elevate sample temperature, which was monitored by a thermocouple.

In-plane microstructure and electron diffraction of TiNi films were observed on a Hitachi H - 800 Transmission Electron Microscope (TEM) operated at 200 kV using a double-tilting specimen holder. Free-standing films obtained by mechanical peeling from

the substrate were glued with acid-resistant lacquer on 3 mm-diameter nickel grids with 2 mm hole. Electron transparency was achieved by twin-jet electropolishing method using a fresh electrolyte containing 20% nitric acid and 80% methanol in volume percentage. The electropolishing apparatus was operated at 8 v to give a current density of 12 mA/mm^2, and the electrolyte temperature was kept between 233 K and 243 K. Better samples were obtained when the initial thickness of the sample was greater than 3 microns.

Chapter 4

RESULTS AND DISCUSSION

In this chapter, experimental results will be presented in two sections. The first section concerns stress and stress evolution behavior in as-deposited films on Si during both isochronal and isothermal anneals, while the second deals with the stress evolution of SMA NiTi films on Si during displacive transformations.

4.1. Stresses and Stress Evolution Behavior of As-Deposited NiTi on Si

Stresses are often introduced from the fabrication process of thin films. Stresses in NiTi films are of particular interest because they are potentially useful in developing two-way shape memory effect by biasing martensite formation. In this section, results from experiments which show the magnitude of stresses that can be introduced into NiTi on Si by d.c. magnetron sputtering, and their evolution behavior during the isochronal and isothermal annealing process, are presented and discussed.

4.1.1. Stress Evolution in NiTi on Si during Post-Deposition Isochronal Heating

The variation of stress with temperature during isochronal heating at a heating rate from 1.5 to 2.5 K/min for as-sputtered NiTi /Si was measured by the wafer-curvature method using equation (3.1). Four representative stress-temperature curves distinguished by the deposition temperatures of the samples are shown in Fig. 4.1. It can be seen that (1), for all samples, upon isochronal heating from room temperature, stresses change at a

rate about -1.5 MPa/K until the temperature reaches the deposition temperature (T_d),[4] where the maximum compressive stress is obtained (for later reference, this stress decrease occurring from RT to T_d is labeled as R-I). (2), When the heating temperature exceeds T_d, the stresses start to relax at rate dependent on the maximum stress. The larger the maximum stress is, the higher the relaxation rate. This stress relaxation occurring starting from T_d is labeled as R-II. (3), Except for the samples deposited at temperatures higher than 673 K, a stress spike with a magnitude of 50 ~ 120 MPa occurs at approximately 723 K (this stress spike at T_c is labeled as R-III). For samples with stress spikes, the stress changes again at a rate of -1.5 MPa/K after the stress spike is established (this stress decrease after T_c is labeled as R-IV); For samples deposited at temperatures higher than 673 K, no stress spike is observed, and the stress remains near zero beyond 873 K on heating (this steady-state stress is labeled as R-V); (4), On cooling at a rate of 30 - 60 K/min, a tensile stress is developed at a rate of 1.5 MPa/K (this stress increase during cooling is labeled as R-VI). In the following section, the origin of each of these stress evolution features is discussed in detail.

4.1.1.1. Extrinsic Thermal Stresses

For a thin film/substrate composite, when the temperature changes, the thermal stress is introduced if their thermal expansion coefficients are different. For NiTi on Si, the linear thermal strain $\varepsilon_{thermal}$ is determined by

$$\varepsilon_{thermal} = (\alpha_{Si} - \alpha_{NiTi}) \cdot \Delta T \qquad (4.1)$$

---

[4] High stress developed from cooling from annealing temperatures may result in delamination of the NiTi films, or fracture of the substrate, especially when the annealing temperature was higher than 923 K. Sometimes the sample was broken into parts upon cooling. In most cases, however, the film was still perfectly kept on the substrate when sample was cooled down to room temperature.
If the films were still on the substrate and when the temperature got close to room temperature, there is a stress relief, which is identified as the result of R-phase or martensitic transformation and is presented in a separate section (4.2) because of its importance.

where α_{Si} and α_{NiTi} are thermal expansion coefficients of Si and NiTi, respectively; ΔT is the temperature change.

Assuming that the substrate remains undeformed and the film is deformed elastically by a strain $\varepsilon_{thermal}$, which is the very close case to our experiment where the thickness ratio between Si substrate and NiTi films is typically more than 100 times, a biaxial thermal stress $\sigma_{thermal}$ can be obtained as:

$$\sigma_{thermal} = \frac{E_{NiTi}}{1-\nu} \cdot (\alpha_{Si} - \alpha_{NiTi}) \cdot \Delta T \qquad (4.2)$$

where ν is Poisson's ratio of the film, E_{NiTi} is the elastic constant of NiTi, α_{Si} and α_{NiTi} are the thermal expansion coefficients of the Si substrate and the NiTi film, respectively, ΔT is temperature change. Taking α_{NiTi} = 15.4 x 10^{-6} [Zhao, 1995], α_{Si} = 3x10^{-6} [Goldsmith, 1961], E_{NiTi} = 83 GPa [Cross *et al.*, 1969; Metals Handbook, 1990] and ν = 0.33 [Beuhler and Wang, 1968], we come a stress slope with temperature during isochronal annealing at ~1.53 MPa/K, which is close to the characteristic stress slope in R-I, R-IV and R-VI. Therefore, it may be concluded that, during the isochronal heating, at temperature lower than T_d, or right after the stress spike (T_c), the extrinsic thermal stress development solely accounts for the stress change, while the intrinsic stress is stable. On cooling at a relatively high rate, the extrinsic thermal stress does not relax appreciably. Further confirmation of the stability of the stress state at temperatures below T_d will be presented below.

4.1.1.2. Stress Development from Crystallization

The stress spike (R-III) occurring at nearly 723 K results from the crystallization of the amorphous films. Previous studies [Ikuta, Fujita, Ikeda and Yamashita, 1990; Hou and Grummon, 1995] showed that crystallinity of sputtered near-equiatomic NiTi was determined to large extent by deposition temperature: at deposition temperatures above 723 K, the as-sputtered NiTi films usually had a fully crystalline structure, while at deposition

temperatures below 573 K, the as-sputtered NiTi films had glassy structure, and at deposition temperatures in between, the as-sputtered NiTi contained partial glassy structure. Crystallization results in a more compact structure so tensile stress development is expected. The reason that the 693 K-deposited films did not show stress spike simply is that no amorphous structure existed in the initial microstructure. Detailed discussion on stress development from crystallization and crystallization temperature is presented in section 4.1.4.

4.1.1.3. Dynamic Stress Relaxation

The continuous stress decrease occurring at temperatures above T_d (R-II) is a stress relaxation phenomenon. During this isochronal annealing period, the stress appears to decrease linearly until it approaches a zero-stress state. The stress decreasing rate varies with different deposition temperatures and the maximum stress at T_d. For the film deposited at 423 K, the stress relaxation rate is 1.2 MPa/K, for the film deposited at 543 K, the stress relaxation rate is 3.7 MPa/K; for film deposited at 623 K, stress relaxation is 2.2 MPa/K, for film deposited at 723 K, the stress relaxation rate is 7 MPa/K.

The stress decreasing rate in R-II results from two opposite processes. One is the continuous increase of compressive thermal stress, the other is stress relaxation. The observation that stress decreases continuously during isochronal heating in R-II indicates that the rate that thermal stress increases is unable to compete with the dynamic stress relaxation rate, therefore, overall stress decreases. Isothermal annealing, which does not result in thermal stress change and allows much more time to observe the stress relaxation, has been used in this study to conduct relaxation kinetic analysis. In the next section, detailed kinetic analyses of the stress relaxation, together with further evaluation of the stress stability observed at the temperatures below T_d are presented.

4.1.2. Stress Evolution of NiTi on Si During Isothermal Annealing

It was shown in last section that stress in as-sputtered NiTi films on Si relaxes at an appreciable rate only when the temperature exceeds the deposition temperature, T_d. However, isochronal data obtained at heating rates from 1.5 K/min to 3.0 K/min used in this study do not lead themselves to adequate kinetic analysis. Both the stress stability below T_d and the stress relaxation behavior above T_d need to be evaluated under isothermal conditions over more prolonged times. The variation of stress with time during isothermal annealing for NiTi films with initial microstructures which are fully crystalline, fully amorphous, or partly amorphous and partly crystalline, are presented in the next sections.

4.1.2.1. Stress Relaxation in Fully Crystalline NiTi on Si

Results Figs. 4-2(a) and (b) show the stress relaxation during isothermal annealing for two NiTi films deposited at 693 K on Si. Fig. 4-2(c) shows detailed stress relaxation behavior during the first 25 ks at each isothermal holding temperature with zero-time corresponding to the beginning of each anneal. It can be seen from the curves that, at temperatures lower than T_d, stress remained stable even when holding time was as long as 40 ~ 60 ks, consistent with the behavior observed in isochronal annealing. In addition, stress tended to relax at an appreciable rate only when the sample was annealed at temperatures higher than T_d, with stress relaxation rates depending on the annealing temperature, initial stress and the time. The higher the initial stress or the higher the annealing temperature, the larger the absolute stress drop during the first few seconds of the isothermal annealing. In the following kinetic analysis, it will be apparent that stress relaxation above T_d occurred by two distinct mechanisms.

Kinetics Analyses Stress relaxation is a process in which total strain, composed of plastic and elastic components, is constant, while elastic strain is continuously converted to plastic strain, causing the stress to decrease as the holding time is prolonged [Oding,

1965]. Maxwell [1868] proposed a dash pot - elastic spring model to describe it. The basic assumption is that the stress relaxation rate is proportional to the stress, *i.e.*,

$$\frac{d\sigma(t)}{dt} = -k \cdot \sigma(t) \qquad (4.3)$$

and if the stress relaxation parameter k, which must be positive, is not a function of the stress σ, the stress at time t is:

$$\sigma(t) = \sigma_0 \cdot exp(-kt) = \sigma_0 \cdot exp(-\frac{t}{\tau}) \qquad (4.4)$$

where σ_0 is the initial stress and τ, the inverse of k, is called the relaxation time.

The above equations essentially describe a viscoelastic process [Oding, 1965]. For crystalline materials, k is also a function of stress, σ, annealing temperature, T, and t. Thus we start from:

$$\frac{d\sigma(t)}{dt} = -k(\sigma, T, t) \cdot \sigma(t) \qquad (4.5)$$

If a first-order-of-time process is assumed [Reed-Hill and Abbraschian, 1992], the parameter $k(\sigma, T, t)$ is not a function of time, and can be obtained as

$$k(\sigma, T) = -\frac{d\sigma(t)}{\sigma(t) \cdot dt} = -\frac{d\, ln(\sigma(t))}{dt} \qquad (4.6)$$

For a diffusional stress relaxation process, $k(\sigma, T)$ can be expressed as a function of diffusivity, D, as [Kato *et al.*, 1990; Shute and Cohen, 1992]:

$$k(\sigma, T) = \frac{E\Omega S}{a_1 a_2 \lambda^2 kT} \cdot D \cdot B(\sigma, T) = \frac{A}{T} \cdot D_0\, exp(-\frac{Q}{RT}) \cdot B(\sigma, T) \qquad (4.7)$$

where E is the elastic modulus, Ω is the atomic volume, S is the cross-sectional area for the diffusion process, k is Boltzmann's constant and a_1, a_2 and λ are grain size parameters. This value for $k(\sigma, T)$ is derived for diffusion within a volume represented by a parallelepiped shaped grain with sides $2a_1 \times 2a_2 \times \lambda$. The cross-sectional area term factor S is a function of the diffusion path, and $A \equiv E\Omega S/(a_1 a_2 \lambda^2 k)$, which is determined by microstructural details and diffusion path. D_0 is the frequency parameter of diffusivity, Q is the activation energy, R is the universal gas constant (= 8.314 J/mol), and $B(\sigma, T)$ is related to the stress and temperature, and can be called a stress induced factor.

Evaluation of $B(\sigma, T)$ is based on the observation that an applied stress can reduce the activation energy by an amount equal to $\Delta V \cdot \sigma$ [Fargeix and Ghibaudo, 1984; Brotzen *et al.*, 1990; Zingu and Mofokeng, 1993], where ΔV is called the activation volume, and σ is taken as the absolute value, which means both tensile stress and compressive stress reduce the activation energy. Thus, $k(\sigma, T)$ can be rewritten by

$$k(\sigma, T) = -\frac{d\,ln(\sigma(t))}{dt} = \frac{A}{T} \cdot D_0\, exp(-\frac{Q}{RT}) \cdot exp(\frac{\Delta V \cdot \sigma}{RT}) \qquad (4.8)$$

or,
$$ln\,k(\sigma, T) = ln\,A - ln\,T + ln\,D_0 - \frac{Q}{RT} + \frac{\Delta V \cdot \sigma}{RT} \qquad (4.9)$$

For an isothermal process at temperature T, $ln(k(\sigma, T))$ should be linearly dependent on stress σ. Assuming $ln(k(\sigma, T)) = m(T) \cdot \sigma + b(T)$, The slope of the line $m(T)$ is $\Delta V/RT$, while the intercept of the line $b(T)$ is the sum of the first four terms in (4.9). Also, if several stress relaxation curves at different temperatures are available, the diffusion volume can be calculated by finding the slope of curve $m(T)$ *vs.* $1/T$ for which the slope should be $\Delta V/R$, and the activation energy is obtained by finding the slope of curve $b(T)+ln(T)$ *vs.* $1/T$ for which the slope should be $-Q/R$.

Kinetic Parameter Calculation Figure 4-3 show curves of $ln(k(\sigma, t))$ *vs.* stress σ (at absolute value), at different annealing temperatures for the data plotted in Fig. 4-2 (a - c). These figures indicate that generally there are two distinct stages of stress relaxation when the isothermal annealing temperature was below 843 K. The first stage (at high stress and short time) is characterized by a steep slope in curve $ln(k(\sigma, T))\sim\sigma$, while the second one is characterized by a shallow slope, which means in the first stage, stress relaxation rate is more dependent on the applied stress.

It is possible to calculate both activation volumes and activation energies for stress relaxation for both relaxation stages from $ln(k(\sigma, T))\sim\sigma$ plots at different temperatures (Fig. 4-3) using the method described above (slope fitting method). In addition, for a given $ln(k(\sigma, T))\sim\sigma$ plot (at a given temperature), the slope $m(T)$ corresponds to $\Delta V/RT$, therefore, ΔV can be calculated by $m(T)\cdot RT$, and averaging all the ΔVs at different temperature gives a value of ΔV (this method is called averaging method hereafter). Results are shown in Fig. 4-4 (a) and (b). For the first stress relaxation stage, the activation energy is 718±12 kJ/mol, and the activation volume arrives at $(8.27\pm0.33)\times10^{-28}$ and $(1.12\pm0.29)\times10^{-28}$ m^3, depending on whether the slope fitting or the averaging methods are used. For the second stress relaxation process, the activation energy is 309±12 kJ/mol, and the activation volume is $(1.34\pm0.93)\times10^{-29}$ m^3 by the averaging method. The activation volume is apparently unavailable from slop fitting method because $m(T)$ appears rather scattered.

It is noted that there is considerable error in determining the activation volume for the first stress relaxation stage, and because the intercepts depend on the slopes, the corresponding activation energy is also considered unreliable. The activation volume for the second stress relaxation is also suspect. However, it is apparently one order of magnitude smaller than that for the first relaxation stage. In addition, the magnitude of stress is smaller for the second stage of stress relaxation than that for the first one. Since the deviation of intercept $b(T)$ is $m(T)\cdot\sigma$ if the stress effect on the activation energy is not

considered, the activation energy obtained by linearly fitting $b(T)+ln(T)$ *vs.* $1/T$ for stress relaxation during the second stage is much more reliable. Actually, the intercept data is fitted well except for the one obtained from annealing at 723 K, the first stop above T_d.

The uncertainty in calculating the diffusion volume and activation energy of the first relaxation stage by equation (4.9) suggests that the relaxation behavior may not be adequately described by equations (4.6) and (4.7), and that other mechanisms, such as microstructural instabilities, may operate when the annealing temperature exceeds the deposition temperature.[5] For near-equiatomic NiTi, grain growth, precipitate growth and precipitation reactions are pronounced upon annealing at temperatures between 673 K to 873 K [Kim *et al.*, 1986; Xie *et al.*, 1990]. The volume change and stress localization brought by these processes influence the evolution of overall stress in ways which are not properly described by equations (4.6) and (4.7). This is because the stress may never fall to zero as time goes to infinity, and because the growth kinetics of second phase formation or grain growth do not necessarily conform to equation (4.1). It may be thus difficult to model,[6] and no successful quantitative analyses have been made at this point.

The second stress relaxation stage at each temperature stop is a diffusion-related relaxation phenomenon. The activation energy for diffusion determines the stress relaxation rate, while stress in turn reduces the activation by an amount equal to $\Delta V \cdot \sigma$ [Fargeix and Ghibaudo, 1984; Brotzen *et al.*, 1990; Zingu and Mofokeng, 1993]. Thus, failure to consider the stress induced term may result in several percent error in the calculation of activation energy [Shute and Cohen, 1992]. Sullivan [1989] arrived at a value of $\Delta V = \Omega/3$ for one-dimension diffusion, where Ω is the atomic volume of the

---

[5] We might be able to show the structure/microstructure instability of sputtered NiTi at temperature higher than the deposition one by comparing the transformation temperatures of hot-deposition as-sputtered films and those of films which experienced annealing at a higher temperature than T_d, since transformation temperatures are sensitive to the microstructure. Data shows that the M_s temperature of as-sputtered crystalline NiTi films is 30 ~ 40 K lower than that of the post-deposition annealed samples.

[6] Later result that stress gradients exist in as-sputtered films which also complicates the modeling.

diffusant. For biaxial stress, a factor of 2 must be to be introduced [Shute and Cohen, 1992]. Even though the data are rather scattered in the activation volume calculation, it appears that the activation volume in the second stress relaxation stage is in the same order of magnitude with the atomic volume of Ti ($\Delta V = 2.23\times10^{-29}$ m^3) or Ni ($\Delta V = 1.21\times10^{-29}$ m^3), while that in the first stress relaxation is one order of magnitude larger.

The activation energy for the second stage of the stress relaxation suggests bulk diffusion rather than the grain-boundary diffusion controls the stress relaxation, since the activation energy for the latter case is typically less than 1 ev. However, the comparison between the activation energy obtained here with those obtained by other authors casts some uncertainty. The chemical activation energy for diffusion in Ni/Ni, NiTi/Ni and TiNi/Ti diffusion couples has been measured by Bastin and Rieck [1974]. They obtained a value of 142 kJ/mol (0.89 ev), which is substantially smaller than the data we have obtained here. The difference is probably because the diffusion in diffusion couples was grain boundary diffusion. Furthermore, stress relaxation processes are controlled by the slowest diffusion species, while the chemical activation energy for intermetallic reactions is controlled by the faster diffusing species. In this context, it is interesting to note that the activation energy of 255 kJ/mol for Ti diffusion in Ni base superalloy [Reed-Hill and Abbraschian, 1992] is comparable to the data we have obtained here.

It is not clear whether grain boundary diffusion related stress relaxation occurs during the annealing, but very likely it occurs because grain boundary diffusion dominates over lattice diffusion where the grain sizes are small. It was proposed that grain-boundary diffusion stops when the normal stresses on the grain boundary have been completely relaxed due to the constraint of the substrate and the columnar microstructure of the films [Jackson and Li, 1982], therefore, stress relaxation by grain boundary diffusion only occurs at an initial stage of relaxation [Oding, 1965], and grain-boundary diffusion alone is unable to completely relax all the stress in thin films. In this experiment, however, because

there is no way to separate the stress relaxation rate by grain boundary diffusion from other mechanisms, the corresponding kinetics parameters were difficult to specify.

The calculation of the activation energy using equation (4.9) is based on the assumption that the parameter A is a constant. Since A is related to the grain size, it must be assumed that the grains do not change during annealing. However, the data from the first annealing at 723 K deviates far from the fitted line, *i.e.*, k is higher than it should be for the first anneal, as shown in Fig. 4-4. This anomaly suggests a microstructural instability. Since k is higher when grain size is smaller [Kato *et al.*, 1990], this suggests that larger grains have resulted after the first annealing. Also, the good reliability of the linear fitting for data above 773 K suggests that the grain size stabilizes after the first annealing excursion.

In summary, it is observed that as-sputtered NiTi films with fully crystalline structures undergo stress relaxation during isothermal annealing above the deposition temperature due to the structure/microstructure instabilities, and by bulk diffusion with an activation energy of 310 kJ/mol. In view of the apparent initial instability of the microstructure, it is interesting to consider stress relaxation of as-deposited films that are initially not fully crystalline. In the following section, presented is the results and discussion of NiTi film deposited at 623 K, which has an initially mixed crystalline and amorphous structure.

4.1.2.2. Stress Relaxation in NiTi on Si with Initially Mixed Structure.

Figure 4-5(a) shows the stress change of a 623 K-deposited film, which is initially partially amorphous and partially crystalline, during isothermal anneals at different temperatures, with time starting at the beginning of the first isothermal annealing at 593 K. Also, the stress was stable at 593 K for an annealing as long as 30 ks, confirming the stress stability at temperatures below T_d. Stress relaxation occurs during annealing at 633 K, and an stress increase of ~150 MPa, which results in the films in 50 MPa tensile stress,

occurs at 673 K due to stress relaxation and crystallization. The film becomes fully crystalline after the annealing at 673 K. Further increases in the temperature brings more compressive stress, which tends to relax at isothermal annealing. The isothermal annealing at temperatures at 773 K or above,[7] and the stress relaxation curves during the first 15 ks at each temperature is shown in Fig 4-5(b).

In order to obtain stress relaxation kinetics, the stress relaxation rate $ln(k(\sigma, T))$ is plotted as a function of stress, following the same procedure used in analyzing stress relaxation behavior in 693 K-deposited films. Fig. 4-6 are the plots of $ln(k(\sigma, T))$ *vs.* σ which also show two-stage stress relaxation process during annealing at temperatures above the crystallization temperature. For the first relaxation stage, the activation energy is 794±66 kJ/mol, and the activation volume is at 11.40±1.35 $\times 10^{-28}$ and 6.03±5.28 $\times 10^{-28}$ m^3 by slope fitting and averaging methods, respectively. For the second relaxation stage, the activation energy is 304±14 kJ/mol, and the activation volume is found to be $7.62 \pm 4.26 \times 10^{-29}$ m^3 by the averaging method, but it is apparently not available by the linear fitting method because the data appears rather scattering. Similarly, because of the errors, it seems that activation energy for both the first relaxation stage, and the activation volumes for the first and second relaxation stage are suspect, while the activation energy for the second relaxation is reliable. Structural instabilities may be responsible for the first relaxation process, and bulk diffusion may be responsible for the second relaxation processes. The activation energy for the second relaxation of fully crystalline NiTi on Si is seen to be very close to that of fully crystallized NiTi on Si with initially partially crystalline structure.

Comparing Fig. 4-4(b) and Fig. 4-7(b), it may be noted that, despite the activation energy is very close, more annealing excursions and high annealing temperature were

---

[7] Stress at temperatures between 673 K to 773 K is so low that considerable error may be introduced in analysis the stress relaxation behavior. Therefore, no isothermal annealing was applied at this temperature range.

needed before the data aligns well along the fitted line, and the fitted line for 723 K-deposited has been shifted to higher temperature, *i.e.*, at a given temperature, k value is larger for the sample deposited at 693 K. Considering the k value increases as grain size decreases [Kato *et al.*, 1990], these features may suggest that the 693 K-deposited film has a small average grain size, or the 623 K-deposited film has experienced more grain growth.

It is noted that the stress relaxation behavior of NiTi film with fully crystalline and that of crystallized film with initially mixed structure is quite similar. This is expected because in both cases the stress relaxation occurs within the crystalline structure. Stress relaxation in amorphous NiTi may be different. This is of interest since amorphous NiTi is prone to form at lower deposition temperature. In the next section, a kinetic analysis of stress relaxation in amorphous NiTi on Si is presented and discussed.

4.1.2.3. Stress Relaxation in Fully Amorphous NiTi on Si

Fig. 4-8(a) shows the stress change with time starting at the beginning of the first isothermal annealing (453 K) of an as-sputtered films deposited at ~473 K, which has a fully amorphous structure. Fig. 4-8(b) shows each stress relaxation curve with time starting at the beginning of each isothermal holding. Once again, stress remained stable during the annealing at 453 K with annealing time as long as 90 ks, confirming that the stress is stable at temperature below T_d. At each anneals, the stress relaxation rate changes with the annealing time. At higher annealing temperature the stress relaxes to zero more quickly.

In analyzing the stress relaxation kinetics, following the same procedure used in analyzing stress relaxation behavior in crystalline or partially crystalline NiTi on Si, the stress relaxation rate is plotted as a function of stress. Fig. 4-9 are the plots of $ln(k(\sigma, T))$ *vs.* σ, which show one-stage stress relaxation process during annealing at temperature above T_d. Unlike those of the crystalline films and partially crystalline films, plots $ln(k(\sigma, T))$ *vs.* σ show a one-stage stress relaxation process. The activation energy for stress

relaxation is 246±10 kJ/mol, and the diffusion volume arrives at 3.52±.32 $\times 10^{-28}$ m^3 and 7.59±3.91 $\times 10^{-29}$ m^3 by slope fitting and averaging methods respectively, as shown in Fig. 4-10.

The activation energy for stress relaxation in amorphous NiTi is obvious lower than that for the second-stage stress relaxation in fully crystalline NiTi. If the stress relaxation in amorphous is also related to diffusion process, this result is reasonable. Amorphous structure is comparably less compact that the crystalline structure, and diffusion process in amorphous materials should be thus easier. Although there is no activation data available for amorphous NiTi, Cotts and his coworkers [1986] obtained the activation energy for interdiffusion in $Ni_{68}Zr_{32}$ amorphous phase to be 1.0 ~ 1.1 ev, which is comparable to the activation energy data from our stress relaxation experiment (1.5 ev). Once again, the difference may arise from that the stress relaxation process is primarily determined by the most sluggish diffusant.

4.1.2.4. Stress Relaxation Behavior of NiTi on Si During Isochronal Annealing

The stress relaxation behavior in R-II during isochronal heating of NiTi films on Si is understandable from the stress relaxation behaviors during isothermal annealing. During the isochronal heating beyond T_d, while extrinsic thermal stress development built more compressive stress, stress relaxation caused continual decrease in compressive stress. In addition, stress relaxation rate was controlled by two processes: on one hand, when the stress (in absolute value) went down, the stress relaxation rate (absolute stress drop in unit time) was decreased since it was proportional to the stress. On the other hand, the stress relaxation rate increases with increased annealing temperature. It is observed that at temperatures above T_d, the overall stress kept decreasing, indicating that the stress relaxation process dominated. Furthermore, since the stress relaxation rate was stable within a fairly long of temperature interval for both amorphous and crystalline films, it is suggested that the stress relaxation rate changes resulting from the decreased stress and

increased temperature were almost canceled out during this period. Ultimately, however, when the temperature went high enough, the stress relaxation rate became so fast that the thermal stress was relaxed very quickly, therefore the stress remained low, as was observed when the temperature approached the crystallization temperature for amorphous films and beyond 893 K for crystalline films.

4.1.3. Stress Evolution of Amorphous NiTi on Si During and After Crystallization

In section 4.1.2 it was shown that the diffusion process as well as structure/microstructure instability may result in the stress evolution in as-sputtered films of fully crystalline, partially crystalline and fully amorphous structure. As will be shown below, for an as-sputtered films with fully amorphous structure, crystallization may also produce a non-equilibrium microstructure. Microstructural evolution during the extended annealing after crystallization of amorphous NiTi film may result in stress relaxation stress in ways which depend on the composition of the film.

Results Figures 4-11 (a) and (b) show two representative stress-time curves of NiTi films deposited at ambient temperature on Si, during isothermal annealing at the crystallization temperature. Both of the curves demonstrate a quick stress drop from compressive stress levels to zero stress due to relaxation in amorphous NiTi, and a quick stress climb of about 170 MPa due to densification during crystallization of the amorphous structure. What distinguishes them from each other is the stability of the 170 MPa tensile stress during extended annealing after crystallization. The first figure (Fig 4-11 (a)) shows a slower stress drop (30 MPa in 4.5 ks) while the second one (Fig. 4-11 (b)) shows a steady-state stress followed by a quicker stress relaxation (70 MPa in 0.5 ks).

TEM observation has been made for each of the aged samples exhibiting different stress variation behavior. As shown in Figs. 4-12 (a) and (b), the sample that has

experienced fast stress relaxation contains numerous Ni_4Ti_3 precipitates while the sample that has experienced no fast stress relaxation is precipitate-free.

Discussion The fact that the sample undergoing a fast stress relaxation contains lots of precipitates while the one undergoing no fast stress relaxation is precipitate-free during the prolonged annealing after crystallization leads to a conclusion that the precipitation is associated with the fast stress relaxation process. [8] It is plausible that the steady stress period corresponds to the incubation and the early growth of precipitates, based on the observation of stress relaxation in (Ti, Nb) high strength low alloy steel [Park *et al.*, 1992; Djahazi *et al.*, 1992]. In an annealing process of a stressed (Ti, Nb) high strength low alloy steel, the stress relaxation rate was reduced when the coherent precipitates start to appear and when they are small. But when the precipitates grew so large that the interfacial coherency between them and the matrix was lost, they have little effect on stress relaxation rate. The authors accounted the dislocation movement and/or diffusion is severely suppressed by the presence of the coherent precipitates. The situation of precipitation in Ni-rich NiTi films is similar. Metastable lenticular precipitates Ni_4Ti_3 are subject to form at an intermediate-temperature annealing. They are coherent with the B2 matrix when they are small, and as they grow, coherent interfaces become semi-coherent, even incoherent [Xie *et al.*, 1990].

Applied stress can induce preferential growth of the precipitate. For example, preferential site for precipitation may exist under applied stresses. In studying stress effects on second phase in Cu-Cd alloys, Sulonen [1964] found that the second phases grew preferentially at grain boundaries that were perpendicular to the applied stress axis,

---

[8] TEM micrographs in Fig. 4.12 suggest that the films showing no fast stress relaxation is very likely close to stoichiometry while the other is one Ni-rich. The composition deviation from film to film arose from target configuration when the films were deposited [Lee, 1994]. Even when all the films are deposited by the targets of same composition, the target wear affects the composition of the film: a newly replaced target tends to produce Ni-rich films, while an over-worn one tends to produce Ti-rich films.

and asymmetric strain was attributed to this phenomenon [Sulonen, 1964; Dryden *et al.*, 1990; Guo *et al.*, 1993]. More relevantly, stress can induce preferential growth of selective precipitate variants, as Ni_4Ti_3 precipitates in Ni-rich NiTi. The preferential growth of Ni_4Ti_3 was proposed by Nishida *et al.* [1986] and confirmed by Li and Chen [1997] under uniaxial stress condition.[9] Since uniaxial stress makes the precipitate variant selective, there is no reason that biaxial stress used in this experiment does not. However, no evidences to support this prediction have been found from the in-plane TEM observations at this point.

Preferential growth of selective precipitate variants may result in a quicker stress relaxation process. In the constrained annealing experiment conducted by Nishida *et al.* [1986], the fixed curvature was formed when the constrained annealing was completed because the elastic strain had been converted to plastic strain, which was a stress relaxation process. The driving force to do so was the reduction of elastic strain energy. By forming topotaxial precipitates, elastic strain energy was reduced in the most efficient way, and therefore, stress relaxation process is quicker. Another In comparison to the precipitate-free sample, the relaxation rate in the precipitate-free sample is determined by the diffusion of sluggish species Ti, while the precipitation of Ni_4Ti_3 is determined by the diffusion of Ni atoms. In this sense, it can also be expected that stress relaxation in Ni_4Ti_3-containing sample is quicker.

4.1.4. Crystallization Temperature of Amorphous NiTi

It has been repeatedly demonstrated that, without additional substrate heating, sputter-deposited NiTi is amorphous, and in order to acquire SME, crystallization is necessary [Kim *et al.*, 1986; Busch *et al.*, 1990]. However, how high the crystallization temperature has to be is of concerns, especially in circumstances where interdiffusion

[9] The preferential growth of Ni_4Ti_3 was believed to create intrinsic two-way shape-memory effect by biasing the martensitic formation [Fig. 4-14].

between the substrate and the films or decomposition of the substrate may occur. For example, Kapton polyimide, a potentially useful substrate, may decompose when exposed to temperatures higher than 723 K even in an inert atmosphere. So there have been efforts aimed at lowering the crystallization temperature of NiTi [Madsen and Jardine, 1993].

As shown in last sections, the completion of crystallization of fully amorphous results in a biaxial stress of ~170 MPa increase, which corresponds to a strain of

$$\varepsilon_{crystallization} = \Delta\sigma \cdot \frac{1-\nu}{E_{NiTi}} = 170 \times 10^6 \cdot \frac{1-0.33}{83 \times 10^9} = 0.00137$$

and a volume change of $\Delta V/V$ = 3·0.00137 = 0.0041. Taking advantage of the stress development, the crystallization process can be monitored by measurement of the stress variation during the isothermal annealing of the NiTi/Si composite, which in turn can yield estimates for the kinetic parameters controlling the crystallization event.

Results Figure 4-14(a) shows stress variation with time of NiTi films deposited at ambient temperature on Si during isothermal annealing at 673 K to 723 K. It is apparent that crystallization occurs at annealing temperatures as low as 673 K. In addition, as the isothermal annealing temperature increases, the annealing time to reach the maximum tensile stress sharply increases, which means the crystallization takes longer. Also evident is that the incubation time is generally needed for the occurrence of the crystallization. For example, when annealing at 708 K, about 0.8 ks of incubation time is needed, However, if the annealing temperature decreases to 673 K, about 25 ks of incubation time is needed.

Discussion Previous reports on crystallization temperature of amorphous NiTi have been inconsistent. It is usually believed that amorphous NiTi will not crystallize until the annealing temperature is higher than 773 K [Johnson *et al.*, 1990]. But other reports indicate the crystallization temperature is lower than 773 K [Nakata *et al.*, 1995; Zhang and Grummon, 1996]. The inconsistency probably arises from the fact that most of the crystallization temperatures have been determined by isochronal heating with heating rates

as high as 20 K/min. Since incubation time is needed for crystallization, the higher the heating rate is, the higher the apparent temperature of crystallization. Isothermal annealing has provided more precise information about how low the crystallization temperature can be.

Considering that the incubation time for crystallization is necessary, it is possible to decrease the crystallization temperature or shorten the crystallization time of NiTi film by deliberately producing crystalline embryos, which can be realized by setting the deposition temperature just slightly above 573 K. Crystallization time of a film deposited at 623 K supports this prediction. As shown in Fig. 4.5 (a), the film deposited at 623 K which is expected to be partially crystalline, is fully crystallized in about 3 ks at 673 K, which is much shorter than 103 ks, the time required for full crystallization of the film deposited at ambient temperature and annealed at 673 K.

Since the crystallization is a thermally activated process, it has a corresponding activation energy. Chang [1992] observed that crystallization which took place during isochronal heating of triode sputtered NiTi and NiTi-Cu multilayer films. Using Kissinger's method [Kissinger, 1957], Chang obtained the activation of 485 kJ/mol for crystallization of single-layer NiTi films deposited by triode sputtering using a $Ti_{50.1}Ni_{49.9}$ target.

For isothermal annealing in this experiment, the activation energy for crystallization can be calculated by measuring the crystallization time τ from the stress-time curves. In this calculation, we ignore the incubation time for crystallization, assume that the crystalline phase fraction is proportional to the stress, and the crystalline phase fraction $\eta = 1 - exp(-t/\tau)$. Therefore, the crystallization time τ corresponds to the time when the stress reaches $1 - 1/e$, *i.e.*, 63.2% of the maximum level. Since $\tau = Aexp(Q/RT)$, the activation energy Q may be obtained by linear-fitting $ln(\tau)$ vs. $1/T$ with the slope corresponding to Q/R. Fig. 4-14(b) shows the linear-fitting result and gives an activation energy of ~477 kJ/mol, which is very close to Chang's result.

In our experiments, crystallization never occurred in NiTi films deposited at ambient temperature if the annealing temperature was lower than 673 K, which is thus the low-temperature limit for the crystallization for amorphous NiTi on (100)Si by post-deposition annealing. By hot deposition, at least partially crystalline structure in as-deposited films may be obtained at deposition temperatures as low as 373 K. For T_d = 673 K, as-sputtered films are fully crystalline within a deposition time of just tens of minutes. This difference may result from the different diffusion mechanism. As we know, crystallization produces an ordered B2 structure, which requires short-range diffusion. Surface diffusion plays a major role in the *in-situ* crystallization process during the deposition, and also, energetic collision events with reflected working gas atoms, incoming neutrals and secondary electrons provide diffusants with additional kinetic energy. Since surface diffusion is a faster mechanism than the bulk diffusion, a lower temperature to produce fully crystalline films is expected where *in-situ* crystallization is involved. Since hot-deposition can produce fully crystalline NiTi at relatively low temperature, it offers an alternative method to produce crystalline NiTi at the situation where high temperature annealing is not practical due to substrate instability.

4.1.5. Intrinsic Stress *vs.* Deposition Parameters

It has been indicated that both intrinsic and extrinsic stresses were stable at temperature below T_d. Intrinsic stresses result from sputtering at T_d. Therefore, their magnitudes can be inferred from the stress-temperature curve of NiTi/Si composites during isochronal heating: the peak stress as the annealing temperature approaches the deposition temperature equals the intrinsic stress.

Results Figs. 4-15 through 4-18 show the intrinsic stress variation with the deposition parameters. It can be seen that, (1) Under the deposition conditions used in this experiment (Ar pressure: 3.6 ~ 5.8 mTorr; T_d: ambient to 723 K), the intrinsic stresses in

NiTi are compressive without exception[10]; (2) higher deposition temperature generates higher compressive stresses. For films deposited at constant Ar pressure, compressive intrinsic stresses was increased from 240 MPa to 700 MPa when the deposition temperature was increased from 373 K to 723 K; (3) lower working gas pressure leads to higher compressive stresses. For films deposited at ambient temperature (T_d = 400 K), compressive intrinsic stress was increased from 380 MPa to 570 MPa when Ar pressure was decreased from 5.2 mTorr to 3.6 mTorr; (4) Thinner films supported more compressive stresses. For films deposited at ambient temperature with a constant Ar pressure of ~5.0 mTorr, compressive intrinsic stress was decreased from 460 MPa to 250 MPa when film thickness was increased from 1.3 μm to 4.4 μm.

Discussion Intrinsic stresses in thin film depends on many processes. *In-situ* condensation and growth make the film more compact, so they usually make the films more tensile or less compressive; incorporation of working gas makes films more compressive or less tensile; *In-situ* stress relaxation makes the films less stressed. But the predominant process by far in sputtered films is the peening effects of the energetic reflected working gas ions, neutrals and electrons on the atoms on the surface and at sub-surface of the films [Hoffman and Thornton, 1977 (a) and (b); 1980; 1982; Thornton and Hoffman, 1985], which produces compressive stress. The more kinetic energy the incoming species have, or the greater the magnitude of the flux, the more compressive stress will be produced. Kinetic energy may be lost if the incoming species collide with working gas atoms. Lower working gas pressure preserves the kinetic energy of the bombarding species since fewer collision events will happen in transit from the cathode. Consequently, low working gas pressure makes the film more compressive.

---

[10] This could be qualitatively verified by observing the reflection of the sputter cathode through a window on the sputtering system. The gun image appeared smaller than it actually is, which means the sample surface is concave, consistent with the thin film being under substantial compressive stress.

The probability that one incoming species collides with the working gas molecules is proportional to the density of the working gas density if the working distance is held constant.[11] Thus, the key parameter is the volume density, n/V, of the working gas. According to the ideal gas equation

$$\frac{n}{V} = \frac{P}{RT} \qquad (4.11)$$

Thus, increasing the temperature while keeping the pressure unchanged decreases the volume density of the working gas, resulting in more compressive stress. In order to show experimentally how the intrinsic stress was related to the working gas density, we combine Fig. 4-15 and Fig. 4-16 into Fig. 4-17 by expressing the stress as a function of P/T for both constant temperature and constant pressure experiments. Plotted this way, constant temperature and constant pressure data collapse onto a single master curve. If treated linearly, the data gives a slope of ~52.6 GPa·mTorr^{-1}·K. In Fig. 4-17, the intrinsic stress is also expressed as a function of the ratio of working distance to free-path length. If treated linearly, the data gives a slope of ~950 MPa per mean free-path length.

Under the same deposition conditions with Ar pressure of 5.1 mTorr and T_d of 400 K, intrinsic stress in the sputtered NiTi film was also found to vary with film thickness, as shown in Fig. 4-18. If treated linearly, the data gives a slope of ~66 MPa·μm^{-1}. Many factors may contribute this effect. First, it is reasonable to consider that the strength of thin film is related to film thickness. Thinner films usually have higher strength [Murakami, M., 1979], and lower flow stress in thicker films places a limit on intrinsic stress.

---

[11] The mean free path, λ, for foreign atoms passing through a space populated with Ar can be calculated as

$$\lambda = \frac{R \cdot T}{N_A \cdot P \cdot \pi (r_{Ar} + r_x)^2} \qquad (4.10)$$

where T is the temperature in Kelvin, R is universal gas constant (=8.314 J·mol^{-1}·K^{-1}), N_A is Avgadro' constant (6.022×10^{23} mol^{-1}), P is Ar pressure in Pascal, and r_{Ar} and r_x are atomic radius of Ar and exotic atoms, respectively. λ is proportional to the ratio of T/P.

Second, *in-situ* stress relaxation may help preserve more compressive stress. As shown in Fig 4-2(b), a post-deposition annealing at the deposition temperature cause a slight stress relaxation, which is a thermally activated process. However, the depositing species have a kinetic energy of up to several electron volts, and the energy exchange between the adatoms and interior atoms could be significant to enhance diffusion related stress relaxation. It is thus expected that *in-situ* stress relaxation results in a faster relaxation rate than the stress relaxation during post-deposition annealing at the deposition temperature. Thicker films have longer time for *in-situ* stress relaxation or densification, so there should be less compressive stresses in the films.

Third, interfacial stress may be neutralized as the film grows. Considering that there exists a certain amount of interfacial strain, which corresponds to certain constraint force. As the thickness of films is increased, the average stress is decreased. In this consideration, it is suggested that a stress gradient may exist along the thickness of films.

Finally, substrate rigidity may affect the intrinsic stress. Assuming that the intrinsic strain produced by energetic ion bombardment is limited for ion fluxes with a given energy level and density, and the strain is also limited within a layer with a certain thickness, therefore, the more rigid the strained layer is, the more the intrinsic stress is produced. For thinner films, the elastic modulus of Si (~126 GPa) mainly contributes to the effective modulus of the strained layer, and as the film grows, the modulus of NiTi film (~83 GPa) contributes more and more to the effective modulus of the strained layer, and cause it decreasing monotonously. As a result, the intrinsic stress decreases as the film thickness increases. The observation [Chang, 1997] that the intrinsic stress is very small in NiTi deposited on Kapton polyimide, which has an elastic modulus as low as 1.4 GPa, supports the substrate modulus effect described above. However, clarification needs to be made using more rigid substrates, such as sapphire (E = 434 GPa), before a positive conclusion may be drawn.

4.1.6. Discussion on the Stresses and Stress Evolution in As-Sputtered NiTi

It has been shown above that (1), large compressive stress, the amount of which was controllable through changing deposition parameters, can be developed from sputtered NiTi films; (2) this stress was stable during isochronal ramping and isothermal holding at temperatures lower than T_d. These results are potentially useful when we want the intrinsic stress to bias martensitic formation, by which cyclic two-way SME can be realized. Since the intrinsic stress is stable until the temperature reaches T_d, it can work under a wide range of temperature. To preserve this stress when temperature changes, however, the thermal expansion coefficients of substrate and the films have to be very close, otherwise, the intrinsic stress may be neutralized by the extrinsic thermal stresses developed from cooling from deposition temperature, as was observed in the present study.

Another implication from the present experiment is extrinsic thermal stress can be used to bias the martensitic transformation to realize two-way SME for NiTi/substrate composites. It has been shown that when the sample is annealed at temperatures higher than T_d, intrinsic stresses may be readily annealed out. In this case, the stress in films arises from the extrinsic stress developed by cooling from the annealing temperature. To get large stress, the thermal expansion coefficients of substrate and the films has to be large. Below will be described experiments which illustrate how high extrinsic tensile stresses can interact with displacive transformations to produce cyclic stress relief and recovery.

4.2. Displacive Transformation Induced Stress Evolution in SMA NiTi Films on Si

Due to the structure difference between martensite and austenite of an NiTi SMA, the martensitic transformation is accompanied by a volume shrinkage of 0.34%, shear strain of 13.07% [Knowles and Smith, 1981], and an elastic constant drop by typically ~50% [Metals Handbook, 1990], any one of which should result in a stress change in a

NiTi film which is attached to a substrate. However, the most important feature for stress evolution in SMA NiTi/Si is the formation of detwinned R phase or detwinned martensite, by which the stress relaxes in a unique way. This section deals with the relaxation of extrinsic thermal stresses in both Ni-rich NiTi/Si and Ti-rich NiTi/Si composites by the R-phase and martensitic transformations, and stress recovery by reverse transformation.

4.2.1. Displacive Transformation induced Stress Evolution in a Ni-Rich NiTi Film on Si

Figure 4-19 show the stress-temperature curve of a 1.3 μm thick Ni-rich NiTi film on Si substrate during a thermal cycle from 253 K to 363 K. The sample used in this experiment was deposited at ambient temperature on Si and had been annealed at 723 K for 2 hours. The stress-temperature curve was obtained right after the annealing. So it is essentially the first thermal cycle after the annealing.

by annealing at 723 K, part of the intrinsic stress is relaxed, and cooling from the annealing temperature, extrinsic tensile stress is introduced at a rate of ~1.5 MPa/K, as discussed in section 4.1.1.1. As the cooling continues, the tensile stress continues increasing until temperature reaches 348 K, at which a maximum stress of ~700 MPa is achieved. Further cooling from 348 K, the stress sharply decreases at a rate of ~10.5 MPa/K during the first ten Kelvin and followed by a rate of ~5.8 MPa/K until the temperature reaches 253 K,[12] where the stress has fallen to ~80 MPa. When the sample is subsequently reheated from 253 K, the stress first decreases at a very shallow slope (~0.85 MPa/K) until 318 K, then climbs sharply to 700 MPa at a rate of ~36 MPa/K. After the stress is fully recovered at 343 K, further heating results in tensile stress decreasing by -1.5 MPa/K. Two features clearly shown in the figure are (1), 700 MPa biaxial stress is relaxed upon cooling is fully recoverable upon heating, so the stress-temperature curve forms a close loop during a cooling/heating cycle; (2), the slope of the stress recovery upon heating is almost 7 times larger than that of the stress relaxation upon cooling.

[12] Further cooling is not available from the apparatus used in this experiment.

The X-Ray diffraction spectrum of the sample at ambient temperature is shown at the left-upper corner of Fig. 4-19. It indicates that the structure of the sample at 298 K is martensite. It might be thought that the volume change and elastic constant drop associated with the B2 → B19' transformation account for the stress relaxation [Jardine *et al.*, 1990]. However, the martensitic transformation is accompanied by a volume shrinkage of ~0.34%, which should cause an increase in tensile stress. According to self-accommodating theory, even if the elastic constant decreased by 50%, the residual stress, σ_r, would be

$$\sigma_r = \frac{700}{2} + \frac{0.0034}{3} \cdot \frac{83000}{2(1-0.33)} = 350 + 140 = 490 \text{ MPa}$$

upon the completion of the martensitic transformation, or, more than 350 MPa should be maintained during the martensitic transformation. However, the stress was in fact relaxed to a value close to zero (~80 MPa), therefore, there must be other reasons for the stress relaxation behavior. The formation of detwinned martensite induced by thermal stress may be the answer. Under the thermal stress, the martensite variants were selectively formed, *i.e.*, the detwinned martensite is formed. The actual martensite variant combination must result in a net macroscopic biaxial strain to cancel the biaxial thermal strain. Thus, the stress is decreased, and the overall energy therefore is decreased. In this aspect, the martensite formation during cooling of an SMA NiTi/Si composite is similar to that in a tensile test of an austenite NiTi at a constant temperature.

However, there may exist differences between the elongating of austenitic NiTi at a constant temperature and the cooling of a stressed SMA NiTi/Si. In the former case, only the variant that experiences the maximum resolved shear stress and thus gives the maximum strain in the stress axis direction, is formed. The material is fully martensitic only when the maximum SE elongation is reached. At that time, the martensite exists as a single variant, and is fully detwinned. In the latter case, however, the martensite does not

have to be single-variant. This is because in NiTi/Si, the observed strain is much smaller than the maximum SE strain. For example, cooling NiTi/Si from 723 K to 273 K creates a strain $\varepsilon_{thermal} = \Delta T \cdot (\alpha_{Si}-\alpha_{NiTi}) = 450\cdot(15.4 - 3)\times10^{-6} = 0.56\%$, which is one order of magnitude smaller than 8.4%, the theoretical maximum recoverable strain for polycrystalline NiTi [Miyazaki, Nomura and Ishida, 1995]. When the temperature reaches M_f, NiTi film is fully martensitic. Therefore, the martensite is in a partially detwinned multi-variant condition. Since martensite has a low flow stress of < 100 MPa [Ford and White, 1996; Krulevitch *et al.*, 1996], low residual stress is expected at temperatures lower than M_s.

Ambient X-Ray diffraction indicated that B19' martensite exist at room temperature. Therefore, the formation of martensite, at least partly, contributes to the stress relaxation during cooling. But it is not clear if the R-phase transformation has been taken place prior to the formation of martensite. From the observation that the stress/temperature slope is apparently steeper stress slope (10.5 MPa/K) during the first ten Kelvins of stress relaxation, it is likely that the B2 → R transformation has occurred. However, according to Nishida *et al.*'s data [1996], the start temperature of the B2 → R transformation increase at a rate of ~0.046 K/MPa under uniaxial applied stress, therefore, the corresponding stress relaxation slope should be $(0.046)^{-1}/(1-\nu) = 33$ MPa/K, which is two times larger than the first slope (10.5 MPa/K) during cooling. On the contrary, for start temperature of R → B19' transformation, the expected stress/temperature slope is $(0.2)^{-1}/(1-\nu) = 7.5$ MPa/K, which is more comparable to the second slope (5.8 MPa/K) of stress relaxation observed during cooling. The major difference between the expected and observed stress relaxation slopes associated with the B2 → R transformation may arise from that the rhombohedral angle of R phase is not acute enough to create as much shape strain as needed to relax stresses. Other reasons include that there may exist deviation between the actual temperature-stress data and that quoted from Nishida's results. It is noted that according to Clausius-Clapeyron's equation, the transformation temperature under stress is related to the

transformation enthalpy, which is not available for this particular sample. Nevertheless, if the compositions are close (both are Ni-rich), the estimation generally holds satisfactorily.

The recovery of the stress upon heating results from SME by reverse martensitic transformation. Since the strain associated with the formation of detwinned martensite is recovered, the stress is recovered. Since the recovery is perfect, it is apparent that no slip-related plastic strain, which is unrecoverable by heating, has been introduced. The perfect recovery also suggests that the biaxial strength of austenite Ni-rich NiTi films is at least 700 MPa, which corresponds to a uniaxial strength of 470 MPa. This value is better than the one obtained by Ishida *et al.* [1996], who reported the critical stress for inducing slip deformation of 8 μm $Ti_{48.7}Ni_{51.3}$ films annealed at 723 K was < 400 MPa. Difference may be expected because of the film thickness and the substrate constraint. Thinner films (1.3 μm in our experiment) may be stronger than free-standing thicker films because the grain size is expected to be smaller, and the substrate constraint makes the dislocation motion more difficult to occur [Nix, 1989].

It appears puzzling that the slope of stress recovery upon heating is considerably steeper than that of stress relief upon cooling. For stress induced transformation, the onset of the stress drop corresponds to M_s at stress σ_{max} and the finish temperature of the stress drop corresponds to M_s at stress σ_{min}, just as what we have stated before. In a similar fashion, the onset temperature of stress recovery corresponds to A_s at stress σ_{min} and the finish temperature of stress recovery corresponds to A_f at stress σ_{max}. Since stress relaxation and recovery are based on reverse transformations and A_f-A_s is usually small (< 5 K), the slopes of stress vs. temperature at heating and cooling should be very close.

The difference in stress change slope between cooling and heating may be explainable considering a two-step reverse transformation during heating. From the electric resistivity-temperature curve of free-standing film, both B19' → R and R → B2 occur during the heating. It may be assumed that the two-step reverse transformation occurs in NiTi/Si since the stress is very low. However, R phase, like martensite, has a low flow

stress, therefore, it will not contribute any remarkable stress recovery. Instead, because B2 phase is strong, R → B2 transformation is mainly responsible to the stress recovery. The increasing rate of biaxial stress in NiTi/Si can also be inferred from Ishida *et al.*'s experiment [1996]. It gives a rate of 1/0.046/(1- ν) = 33 MPa/K, which is close to 36 MPa/K, the slope observed in the present experiment.

4.2.2. Displacive Transformation Induced Stress Evolution in a Ti-rich NiTi Film on SiO_2/Si

Figure 4-20 shows the stress *vs.* temperature curves of a Ti-rich NiTi/SiO_2/Si composite which experienced different annealing treatments between thermal cycles from 283 K to 383 K. The sample was obtained by 473 K-deposition of NiTi on SiO_2 passivated Si substrate[13] using a Ti/NiTi composite target (see Chapter 3 for detail). The sample experienced four thermal treatments after each the sample was thermally cycled in order to get a stress-temperature curve. The four treatments were: the 1st, 2 hours at 723 K; the 2nd, 1 hour at 873 K; the 3rd, 4 hours at 873 K and the 4th, 3.5 hours at 873 K. Except for the 4th stress-temperature curve, each curve was obtained directly after the annealing, so essentially the stress-temperature data come from the first cooling/heating cycle after each anneal. The 4th curve was from the second thermal cycle after the annealing, because before conducting stress measurement, two 0.3 μm thick 3 mm x 3 mm gold squares were coated at the edge of the sample in order to perform *in-situ* resistivity measurement. During the gold-coating process, the temperature reached 373 K.

---

[13] The purpose of using SiO_2 here was to avoid interdiffusion between Si and NiTi because high annealing temperature was used. The SiO_2 layer was only 0.2 micron and was just 1/8 of NiTi layer and 1/1500 of the Si substrate thickness. It did not significantly affect the stress measurement but did provide a good diffusion barrier since experiments demonstrated that annealing at temperature higher than 873 K may destroy the interface between the unpassivated Si and NiTi.

4.2.2.1. Stress-Temperature Hysteresis Loop After Annealing at 723 K

Figure 4-20 shows the stress-temperature hysteresis loops during thermal cycling from 283 K to 383 K. The first hysteresis loop has $\Delta\sigma \approx 100$ MPa, $\Delta T < 3$ K, and may be from the R-phase transformation occurring in a limited volume fraction of material. The electric resistivity-temperature curve (Fig. 4.21) for a similar free-standing film which experienced the same annealing treatment also suggests that the R-phase transformation is responsible to the stress-temperature hysteresis loop. As shown in Fig. 4-21, after annealed 723 K for 2 hours, the Ti-rich film (at zero stress) had a very low martensite start temperature (240 K). If a slope of 0.2 K/MPa for M_s increase by applied stress is assumed [Nishida *et al.*, 1996], the M_s under 600 MPa biaxial stress is 320 K, which is somewhat lower than the onset temperature of the stress relief (~340 K). From the resistivity data of free-standing film, the R phase start temperature without applied stress was at 333 K, and considering the applied stress can also increase the R-phase transformation temperature, it is plausible that the R-phase transformation alone accounted for the stress relief. Noticeably, upon the completion of the R-phase transformation, only 100 MPa out of 600 MPa stress was relaxed, suggesting that only a limited volume fraction was transformed. It may be concluded that there are non-transforming material present, possibly in a form of amorphous or highly defected NiTi resulting from incomplete crystallization .

4.2.2.2. Stress-Temperature Hysteresis Loops After Annealing at 873 K

Three larger stress-temperature hysteresis loops ($\Delta\sigma = 450 \sim 800$ MPa, $\Delta T = 10 \sim 25$ K) were obtained after the sample was annealed at 873 K for 1 hour, accumulatively for 5 hours and accumulatively for 8.5 hours, respectively. As shown in Fig. 4-20, the loop obtained after the sample experienced the first 873 K annealing, which has a maximum stress of 850 MPa, is not closed while the other two are closed. Since the non-closed loop indicated that non-recoverable strain has been introduced, the austenite yield strength is apparently lower than 850 MPa. In addition, at the very initial stage of cooling, the stress

is apparently steady, instead of increasing at the expected 1.5 MPa/K slope, also indicating the film is yielding. Similarly, the closed loops occurring when the sample experienced more anneals at 873 K indicate that the film has a yielding strength is higher than or equal to 780 MPa.

Stress Relaxation on Cooling After annealing at 873 K, stresses resulting cooling from annealing temperature can be relaxed to almost zero stress upon cooling. The stress relaxation paths is composed of two segments, the first segment has a steeper slop (~50 MPa/K) while the second segment has a more shallow slop (~11 MPa/K). For all the stress relaxation paths, while the onset temperatures for stress relaxation change little, the finish temperatures for stress relaxation change significantly. After annealing 1 hours at 873 K, the stress relaxation finish temperature is 288 K. When the annealing time at 873 K increases to accumulatively 5 hours, the stress relaxation finish temperature becomes 310 K. With accumulatively 8.5 hours at 873 K, the stress relaxation finish temperature increases to 318 K.

The change of stress-temperature slope on cooling suggests the mechanism changes during the stress relaxation. In order to get the transformation information during stress relaxation and recovery, electric resistivity has been measured *in-situ* during stress measurement. The stress-temperature curve together with a resistivity-temperature curve acquired during a cooling/heating cycle from 300 K to 290 K for the NiTi/SiO_2/Si composite, which was annealed 2 hours at 723 K and accumulatively 8.5 hours at 873 K, are shown in Fig. 4-22. According to the traditional resistivity change with transformation in NiTi SMA [Thornburg, Dunne and Wayman, 1971], it is clearly indicated that the R-phase transformation is responsible for the first segment of the stress relaxation, while the martensitic transformation is responsible for the second segment of the stress relaxation during continued cooling. The stress bump occurring when the martensitic transformation started suggests that there is a volume shrinkage, which is in agreement with the theoretical

calculation from lattice parameters [Knowles and Smith, 1981]. However, it is not possible to relate the stress bump with exact volume change, since the stress reflects the detwinning stress flow of the martensite.

Because the configurations of stress-temperature curves after the sample was annealed at 873 K with varying time are similar, it is suggested that the two-step transformation is responsible for the stress relaxation behavior during cooling after the sample was annealed at 873 K. The stress relaxation in the first segment upon cooling corresponds to stress induced B2 → R transformation, by which the stress was decreased at a rate of ~55 MPa/K. This stress decreasing rate in Ti-rich film is apparently larger than the one observed in Ni-rich films (~36 MPa/K), which is expected because Ti-rich NiTi usually has a larger transformation enthalpy than Ni-rich alloys[Lo *et al.*, 1990]. For the same reason, it is expected the rate of stress decrease by stress induced martensitic transformation in Ti-rich film (11 MPa/K) is also larger than that in Ni-rich film (~5.8 MPa/K).

It is noted that the onset temperature for stress relaxation corresponds to R_s under the stress. According to the transformation temperature data for similar free-standing film that experienced annealing at 873 K (Figure 4-23), R_s remains stable as the annealing time at 873 K is prolonged. Since R_s is rather insensitive to the stress (0.046 K/MPa for uniaxial stress), reasonably the onset temperature for stress relaxation does not change significantly. The stress relaxation finish temperature, however, corresponds to M_s under zero stress. According to the transformation data of annealed free-standing film (Fig. 4-23), it increases evidently as the annealing time at 873 K increases. Therefore, it is expected that the stress relaxation finish temperature increases with increased annealing time.

Stress Recovery on Heating For thermocycles after the sample was annealed at 873 K, the stress that relaxed upon cooling can be recovered by reheating. From Fig. 4-20

it can be seem that the onset temperature for stress recovery increases with increased annealing temperature, and the stress recovery slope on heating is very close to the stress relaxation rate by stress induced B2 → R transformation. This suggests that the stress recovery primarily results from the corresponding reverse transformation, *i.e.*, R → B2 transformation. Since B19' phase has formed when the sample is cooled down, During reheating, B19' → R transformation must have occurred before the quick stress recovery begins. The reason that no obvious stress change for B19' R transformation is that the flow stress of R phase is because R phase has a flow stress as low as 40 MPa [Miyazaki, Kimura and Otsuka, 1988]. Stress is limited within the flow stress by forming biased R phase variant.

The onset temperature for stress recovery during heating corresponds to A_s temperature at zero stress. From the transformation temperature data of annealed free-standing film (Fig. 4-23), it is expected that the onset temperature for stress relaxation increases as the annealing time at 873 K is prolonged.

4.2.3. Discussion about the Potentials of the Transformation Induced Stress Relief of NiTi on Si.

The stress relaxation and recovery of SMA NiTi/Si demonstrated in the last two sections may be useful for actuation in microelectromechanical system. Characteristics of the stress-temperature hysteresis loops include:

1. Stress relaxation and recovery is reversible at biaxial stress as high as 780 MPa;
2. Stress may be relaxed to nearly zero state on cooling;
3. Stress relaxation and recovery are driven by temperature change;
4. The onset temperatures for stress relaxation and recovery may be controllable in a limited range by thermal treatment as well as stress;

The stress relaxation and recovery can produce cyclic displacements. If a 700 MPa biaxial stress in 3 μm NiTi on 2" diameter 300 μm thick Si is achieved before stress relaxation,

according to Stoney's equation (3.1), the composite has a curvature radius of ~1.3 m. Upon cooling when the stress is fully relaxed, the curvature radius becomes infinite. If the center of the composite is secured, a displacement of 250 μm is produced at the rim of the composite. Or for a 2" long cantilever, if one end is secured, a displacement of nearly 1 mm is produced at the other end (Fig. 4-24). According to Stoney's equation, the curvature radius of the composite is proportional to film thickness, substrate modulus and inverse of square of substrate thickness, larger displacement is available when thinner substrates or less rigid substrates is used [Krulevitch *et al.*, 1995].

Although the stress output was large, strain output was far less than the maximum available from NiTi SMA films. Again assuming 700 MPa stress is achieved before stress relaxation, which can be relaxed out on cooling and recovered completely on heating, the reverse martensitic transformation produces a strain in NiTi of

$$\Delta\varepsilon = \Delta\sigma \cdot \frac{1-\nu}{E_{NiTi}} = 700 \cdot \frac{1-0.33}{83000} = 0.0056$$

which is almost one order of magnitude smaller than the typical fully recoverable strain in NiTi films [Ishida, 1996]. Therefore, the transformation energy output density is far less than the optimum. The reason for this is that the detwinning strain of martensite is preset by the substrate. Further cooling results in multi-variant self-accommodating martensite, which is unable to generate directional energy output. One way to maximize the energy density output is pre-deform the free-standing SMA NiTi films by the maximum fully recoverable strain, which corresponds to fully detwinned martensite in microstructure, then deposit an elastic layer. A robust SME will be produced by the reverse martensitic transformation and the fully dewinned martensite may be restored by the elastic layer upon cooling. Research in this direction is currently in progress.

Chapter 5

CONCLUSIONS

From experiments on stress evolution in as-deposited and annealed NiTi on Si during isochronal and isothermal anneals, and based upon structure and microstructural analyses, the following conclusions may be drawn:

1. Compressive intrinsic stresses were obtained without exception in magnetron sputtered NiTi films when deposition temperatures from ambient to 723 K and argon pressures from 3.6 to 5.8 mTorr were used. The magnitude of the intrinsic stress increased with decreasing working gas pressure, increased deposition temperature and decreased film thickness. The ratio of the argon pressure to the deposition temperature, which is proportional to the working gas density, apparently determines the magnitude of the compressive stress, giving a rate of ~52.6 $GPa \cdot K \cdot mTorr^{-1}$.
2. Irrespective of the deposition temperatures or the degree of crystallinity in as-deposited films, the stress decreased at a rate of ~1.5 MPa/K during heating between ambient temperature and the deposition temperature, which is the characteristic slope of thermal stress development of NiTi on Si based on differential thermal expansion coefficients. Isothermal annealing experiment confirmed that both intrinsic stress and thermal extrinsic stresses were stable at temperatures below the deposition temperature, and they were subject to relaxation at temperatures higher than the deposition temperature. Kinetics analysis indicated that a two-stage relaxation

process occurred during isothermal annealing of crystalline or partially crystalline as-deposited films at temperatures higher than the deposition temperature. The first was characterized by relaxation rates more strongly dependent on stress, while the second was characterized by lower relaxation rates, less dependence of stress, and an activation energy of ~310 kJ/mol. One-stage stress relaxation was observed for as-deposited amorphous films characterized by an activation energy of ~248 kJ/mol.

3. Amorphous films on (100)Si can be crystallized at temperatures as low as 673 K during isothermal annealing. The activation energy for crystallization of amorphous films was 477 kJ/mol. Crystallization of fully amorphous films produced a tensile stress of ~170 MPa during isothermal annealing.
4. Stress relaxation behavior during and immediately following depends on composition and microstrutural stability. The precipitation of Ni_4Ti_3 leads to a constant stress nucleation period followed by an obviously faster stress relaxation process than that was observed in precipitate-free samples.
5. Reversible stress relief and recovery during thermal cycling was observed in crystallized Ni-rich NiTi/Si composites. the maximum fully recoverable stress was greater than 700 MPa. As the temperature was decreased from high temperature to subambient temperature, stress in the film was relaxed to nearly zero stress, and the stress was recovered by a slope obviously steeper than that of stress relaxation during cooling when the sample was heated. By analyzing the stress relaxation and recovery slopes, X-ray diffraction and transformation temperatures, stress induced R-phase or martensitic transformation was responsible for the stress relaxation on cooling, while R $\rightarrow$ B2 transformation was mainly responsible for the stress recovery on heating.
6. Reversible stress relief and recovery during thermal cycles around room temperature was also found in crystallized Ti-rich TiNi/SiO_2/Si composites. The maximum fully recoverable stress was between 780 MPa to 850 MPa. Stresses above 850 MPa

apparently caused plastic flow in the austenite phase. When a sample deposited at 473 K was annealed at 723 K, the R-phase transformation resulted a small narrow stress-temperature loop between 328 K and 338 K, and 500 MPa residual stress still remained upon the completion of the R-phase transformation. When the sample was annealed at 873 K, stress could be relaxed to less than 100 MPa, and both the B2 $\rightarrow$ R and R $\rightarrow$ B19' transformations contributed to the stress relaxation on cooling, while R $\rightarrow$ B2 transformation was mainly responsible for the stress recovery on heating. Thermal treatment at 873 K may affect the onset temperatures of stress relaxation on cooling and stress recovery to a limited extent.

BIBLIOGRAPHY

BIBLIOGRAPHY

Adachi, K., Perkins, J. and Wayman, C.M., *Acta Metall.* **36**, 1343, 1988

Alam, M.R., kumar, A., Shu, N.., Chan, H.L. and You, Q., *Applied Surface Science*, **109/110**, 393, 1997

Angst, D.R., Thoma, P.E. and Kao, M., *J. de Physique IV*, **5**, C8-747, 1995

Arbuzova, I.A. and Khandros, L.G., *Phys. Met. Metalloved*, **17**, 390, 1964

Ashley, S., *Mechanical Engineering*, p91, September issue, 1996

ASM Metals Handbook, 10th ed., Vol.2, the Materials Information Society, 1990

Badahan, M., Canet, M., Seguin, J.-L. and Carchano, H., *Materials Science and Engineering*, **B34**, 112, 1995

Baglin, J.E., in *Ion Beam Modification of Isolators*, Eds. Mazzoldi, P. and Arnold, G., Elsevier, Amsterdam, 1987

Bastin, G.F. and Rieck, G.D., *Metall. Trans*, **5**, 1827, 1974

Bhan, S., *J. the Less-Common Metals*, **25**, 215, 1971

Birnbaum, H.K. and Read, T.A., *Trans. AIME*, **218**, 662, 1960

Blachman, A.G., *Metall. Trans.*, **2**, 699, 1971

Brotzen, F.R., Rosenmayer, C.T., Cofer, C.G. and Gale, R..J., *Vacuum*, **41**, 1290, 1990

Buehler, W.J. and Gilfrich, J.V. and Wiley, R.C., *J. Applied Phys.*, **34**, 1475, 1963

Beuhler, W.J. and Wang, F.E., *Ocean Engineering*, **1**, 105, 1968

Beyer, J., Brakel, R.A. and Lloyd, J.R.T., *Proc inter Conference on Martensitic Transformation*, 703, 1986

Buchel, W., *J. Vac. Sci. Technol.*, **6**, 606, 1969

Buchwitzz, M., Adlwarth-Dieball, R. and Ryder, P.L., *Acta Metall. Mater*, **41**, 1885, 1993

Busch J.D. and Johnson, A.D., *IEEE' 90*, 40, 1990

Busch, J.D., Johnson, A.D., Hodgson, D.E., Lee, C.H. and Stevenson, D.A., (a), *Materials Science Forum*, **56-58**, 729, 1990; (b), *J. Applied Physics*, **68**, 6224, 1990

Busch, J., Johnson, A.D., Lee, C.H., and Stevenson, D.A., *J. Appl. Phys.*, **68**, p6224, 1990

Buschow, K.H., *J. Appl. Phys.*, **56**, 304, 1984

Cahn, R.R., *Nature*, **374**, 120, 1995

Caswell, H.L., Priest, J.R. and Budo, Y., *J. Appl. Phys.*, **34**, 3261, 1963

Chang, F., unpublished work, Michigan State University, 1997

Chang, L., Ph.D. Dissertation, Michigan State University, 1994

Chang, L., and Grummon, D. S., *MRS Symposium Proceedings*, **246**, p141, MRS Society, Pittsburgh, 1992; *Philosophical Magazine*, **A76**, 163, 191, 1997

Chang, L.C. and Read, T.A., *Trans AIME*, **49**, 191, 1951

Chason, E., Mayer, T.M. and Howard, A.Y., *MRS Symposium on Mechanisms of Thin Film Evolution*, Pittsburgh, PA, **317**, 91, 1984

Chaudhari, P., J. *Vac. Sci. Technol.*, **9**, 520, 1972

Chopra, K.L., *Thin Film Phenomena*, p138, 1969

Clemens, B.M., *Physical Review*, **B33**, 7615, 1986

Cotts, E.J., Meng, W.J. and Johnson, W.L., *Physical Review Letters*, **57**, 2295, 1986

Cross, W., Kariotis A. and Stimler, F., *Nitinol Characterization Study*, NASA CR-1433, 1969

d'Heurle, F.M., *Metall. Trans.*, **1**, 725, 1970; *International Materials Reviews*, **A34**, 53, 1989

d'Heurle, F.M., Berenbaum, L. and Rosenburg, R., *Trans. AIME*, **242**, 502, 1968

Davis, L.A., *Metallic Glasses*, American Society of Metals, Metals Park, Ohio, 1978

Delaey, L., van Humbeeck, J., Chandrasederan, M., Janssen, J., Andrade, A. and Mwamba, N., *Metals Forum*, **4**, 164, 1981

Ditman, J.B. and Bergman, L.A., in *Proc of 2nd Inter Conference on Intelligent Materials*, ed. Rogers C.A. and Wallece, G.G., p450, Virginia, Technical Publishing Co. Inc., 1994

Djahazi, D., He, X.L., Jonas, J.J. and Sun, W.P., *Materials Science and Technology*, **8**, 628, 1992

Donkersloot, H.C. and van Vucht, J.H.N., *J. of the Less-Common Metals*, **20**, 83, 1970

Doljack, F.A. and Hoffman, R.W., *Thin Solid Films*, **12**, 71, 1972

Drory, M.D., Thouless, M. and Evans, G., *Acta Metall.*, **36**, 2019, 1988

Dryden, J.R. and Purdy, G.R., *Acta Metall.*, **38**, 1255, 1990

Du Pont Co., Product data sheet.

Dunne, D.P. and Wayman, C.M., *Metall. Trans.*, **4**, 137, 1973

Engineered Materials Handbook, **Vol.4**: Ceramics and Glasses, ASM international, 1993

Fan, L.S., Tai, Y-C. and Muller, R., *Sensor and Actuator*, **20**, 41, 1989

Fargeix, A. and Ghibaudo, G., *J. Applied Physics*, **56**, 589, 1984

Flugge, W., *Viscoelasticity*, Blaisdell Publishing Company, Waltham, MA, p5, 1967

Filip, P. and Mazanex, K., *Scripta Mater.*, **35**, 349, 1996

Ford, D.S. and White, S.R., *Acta Mater.*, 1996

Fukuyo, S., Suzuki, K. and Sairenji, E., in *Engineering aspects of Shape Memory Alloys*, eds. Duerig, T. W., Melton, K.N., Stockel, D., and Wayman, C.M., Buttherworth-Heinemann Ltd., Boston, 1990

Gabraud, R.J. and Delage, J., *Thin Solid Films*, **200**, 275, 1991

Gangulee, A., *Acta Metall.*, **22**, 177, 1974

George, J., *Preparation of Thin Films*, Marcel Dekker Inc, New York, 1992

Goldsmith, A., Waterman, T. and Hirschorn, H., *Handbook of Thermophysical Properties of Solid Materials*, Amor Research Foundations, Pergamon, 1961

Goldstien, D., Kabacoff, L. and Tydings, J., *J. Metals*, **39**, 19, 1987

Grummon, D., Hou, L., Zhao, Z. and Pence, T., J. *de Physique IV*, **Colloque C8**, 665, 1995

Guo, W., Dryden, J.R. and Pury, G.R., *Acta Metall.*, **41**, 1183, 1993

Han, X., Zou, W., Wang, R., Zhang, Z. and Yang, D.Z., A*cta Mater.*, **44**, 3711, 1996

Hardwick, D.A., *Thin Solid Films*, **154**, 109, 1987

Hayashi, S., *Int. Progress in Urethanes*, **6**, 90, 1993

Hoffman, R.W., in *the Use of Thin Films in Physical Investigations*, ed. Anderson, J.C., p261, Academic Press, New York, 1966; *Phys. Thin Film*, **2**, 211, 1966; *Thin Solid Films*, **34**, 185, 1976; *Thin Solid Films*, **107**, 353, 1983

Hoffman, D.W. and Thorton, J.A., *Thin Solid Films*, **40**, 355, 1977(a) ; *Thin Solid Films*, **45**, 383, 1977(b); *J. Vac Sci Technol*, **16**, 134, 1979; *J. Vac Sci Technol*, **17**, 380, 1980; *J. Vac Sci Technol*, **20**, 335, 1982

Horikoshi, H. and Tamura, N., *Jpn J. Appl. Phys.*, **2**, 328, 1963

Hou, L., Ph.D. dissertation, Michigan State University, 1997

Hou, L. and Grummon, D.S., *Scripta Mater.*, **33**, 989, 1995

Hou, L., Pence, T.J. and Grummon, D.S., *Mat. Res. Soc. Proc.*, **360**, 369, 1995

Hsu, Z.Y., *Martensite and Martensitic Transformation*, Academic Press, 1980

Hua, S., Su, C.M., and Wuttig, M., *MRS Symposium Proceedings*, **360**, p375, MRS Society, Pittsburgh, 1995

Hwang, C.M., Meichle, M., Salamon, M.B. and Wayman, C.M., *Phil. Mag.*, **A47**, 9, 31, 1983

Ikuta, K., Fujita, H., Ikeda, M., and Yamashita, S., *Micro Electo Mechanical Systems*, IEEE Proceedings No. 90CH2832-4, p38, **IEEE**, Piscataway, 1990

Ishida, A., Takei, A. and Miyazaki, S., *Thin Solid Films*, **228**, 210, 1993

Ishida, A., Sato, M., Takei, A., Kase, Y. and Miyazaki, S., *J. de Physique IV*, **5**, C8-70, 1995

Ishida, A., Sato, M., Takei, A. and Miyazaki, S., *Mater. Trans., JIM*, **36**, 1349, 1995

Ishida, A., Sato, M., Takei, A., Nomura K. and Miyazaki, S., *Metall. and Mater. Trans.*, **27A**, 3753, 1996

Jackson, M.S. and Li, C.-Y., *Acta Metall.*, **30**, 1993, 1982

James, R. and Wuttig, M., MSM Seminar, MichiganState University, 1997; *Preprint for Philosophical Magzine*, 1997

Jardine, A.P., *Proceedings of MRS*, **271**, 31, 1990

Jessen, D.E. and Pennycook, S.J., *MRS Symposium on Mechanisms of Thin Film Evolution*, Pittsburgh, PA, **317**, 297, 1984

Johnson, A.D., *J. MicroMech Eng.*, **1**, 39, 1991

Johnson, A.D., Busch, J.D., Ray, C.A. and Charles, S., *Proceedings of MRS*, **271**, p151, MRS, 1992

Johnson, A.D., Martynov, V.V. and Minners, R.S., *J. de Physique IV*, **5**, C8-783, 1995

Johnson, A.D., Martynov, V.V. and Shahoian, E.J., *Proceedings of SPIE*, **2441**, 165, 1995

Johnson, W.L., *Materials Science and Engineering*, **97**, 1, 1988

Jongste, J.F., Hollanders, M.A., Thijsse, B.J., and Mittemeijer, E.J., *Materials Science and Engineering*, **97**, 101, 1988

Kato, M., Niwa, H., Yugi, H. and Tsuchikama, H., *J. Applied Physics*, 68, 334, 1990

Kaufman, L. and Cohen, M., *Pro. Met. Phys.* **7**, 165, 1958

Kawamura, Y., GyA., Horikawa, H. and Tsaburi K., *J. de Physique IV*, **5**, C8-683, 1995

Kessler, H. and Pitsch, W., *Acta Metall.*, **13**, 871, 1965

Kester, J.D. and Messier, R., *J. Materials Research*, **8**, 1928, 1938, 1993

Kim, J.J., Moire, P. and Steveson, D.A., *Scripta Metall.*, **20**, 243, 1986

Kim, T., *Ph.D. Dissertation*, University of Maryland, 1994

Kim, Y., Katsurai, M. and Fujita, H., *Sensor and Actuator*, **20**, 33, 1989

Kinuma, R., Matsumoto, M. and Honma, T., *Spring Meeting of Japan Institute of Metals*, Sedai, p221, 1986

Kissinger, H.E., *Anal. Chem.*, **29**, 1702, 1957

Klokholm, E., *J. Vac. Sci. Technol.*, **6**, 138, 1969

Klokholm, E. and Berry, B.S., *J. Electrochem. Soc.*, **115**, 823, 1968

Knowles, K.M. and Smith, D.A., *Acta Metall.*, **29**, 101, 1981

Koskimaki, D., Marcinkowski, M.J. and Sastri, A., *Trans. AIME*, **245**, 1883, 1969

Krulevitch, P., Ramsey, P.B., Makowiecki, Lee, A.P., Northrup, M.A. and Johnson, G.C., *Thin Solid Films*, **274**, 101, 1996

Krulevitch, P., Lee., A. P., Ramsey, P.B., Trevino, J. C., Hamilton, J., and Northrup, M. A., *J. of Microelectromechanical Systems*, **5**, 207, 1996

Kuribayashi K., Yoshitake, M. and Ogawa, S., IEEE, p217, 1990

Lee, A., Dino, R.C., Krulecitch, A.P., Lehew, S., Trwvino, J. and Northrup, M.A., *8th inter Conference on Solid-State Sensors and Actuators and Eurosensors IX*, Stockholm, p368, 1995

Lee, J., M.S. Thesis, Michigan State University, 1994

Li, D. and Chen, L., *Acta Mater.*, **45**, 471, 1997

Lieberman, D.S., Schmerling, M.A. and Karz, R.S., *Shape Memory Effects in Alloys*, p203, Plenum, New York, 1975

Liebermann, D.S., Wechesler, M.S. and Read, T.A., *J. of Applied Physics*, **26**, 473, 1955

Lin, H.C., Wu, S.K. and Chang, Y.C., in *Shape Memory Materials'94*, ed. Chu Y. and Tu, H., International Academic Publishers, Beijing, 1994

Ling, C.H. and Kaplow, R., *Metall. Trans.*, **A11**, 77, 1981

Liu, Y. and McCormick, P.O., *Acta Metall Mater.*, **38**, 1321, 1990; *Materials Transactions, JIM*, **37**, 691, 1996

Lo, Y. C., Wu, S.K. and Wayman, C.M., *Scripta Metallurgica et Meterialia*, 24, 1571, 1990.

Lotkov, A.I., Grishkov, V.N. and Fadin, V.V., *Phys. Stat. Sol.*, **a(70)**, 513, 1982

Lu, S., in *Engineering aspects of Shape Memory Alloys*, eds. Duerig, T.W., Melton, K.N., Stockel, D., and Wayman, C.M., Buttherworth-Heinemann Ltd., Boston, 1990

Macherauch, E. and Kloos, K.H., *Residual Stress in Science and Technology*, ed. Macgerauch, E. and Hauk, V., Intormationsgesellschhaft, Verlag, **Vol.1**, p3, 1987

Madsen J.S. and Jardine, A.P., *MRS Proceedings*, **308**, 45, 1993

Massalski, T.B., (ed), *Binary Alloy Phase Diagrams*, **2**, 1768, American Metals Society, Metal Park, Ohio, 1987

Mathews, S.A., Wuttig, M. and Su., Q., *Metall. Mater. Trans.*, **27A**, 2859, 1996

Matsumoto, O., Miyazaki, S., Otuka, K. and Tamira, H., *Acta Metall.*, **35**, 2137, 1987

Matthews, J.W. and Blakeslee, A.E., *J. Cryst. Growth*, **32**, 265, 1976

Mattox, D.X., in *Adhesion Measurement of Thin Films, Thick Films and Bulk Coatings*, ASTM Special Technical Publication 640, ed. Mittal, K.L., 54, 1978

Maxwell, J.C., *Phil. Mag.*, Series 4, **35**, 129, 1868

Meng, W.J., Fultz, B., Ma, E., And Johnson, W.L., *Appl. Phys. Lett*, **51(9)**, 1987.

Meichle, M.E., Ph.D. dissertation, University of Illinois, 1981

Melton, K.N., *Proc Int. Conference on Martensitic Transformation*, p1054, 1986

Mercado, P.G. and Jardine A.P., P*roceedings of SPIE*, **2441**, 185, 1995

Mercier, O. and Melton, K.N., *Metall. Trans.*, **A10**, 387, 1979

McNichols Jr., J.L. and Corey, J.S., *J. of Applied Physics*, **61**, 972, 1987

Mittal, K.L., *Electroncomponent Science and Technology*, **3**, 21, 1976

Miyazaki, S., Hashinoga, T., Yumikura, K., Hirikawa, H., Ueki, T. and Ishida, A., *Proceedings of SPIE*, **2441**, 156, 1995

Miyazaki, S., Imai, T., Otsuka, K. and Suzuki, Y., *Scipta Metallurgica*, **15**, 853, 1981

Miyazaki, S., and Ishida, A., *Mater Trans., JIM*, **35**, p14, 1994

Miyazaki, S., Kimura, S. and Otsuka, K., *Phil. Mag.*, **A57**, 467, 1988

Miyazaki, S., Nomura, K. and Ishida, A., *J. de Physique* IV, **5**, C8-677, 1995

Miyazaki, S. and Otuska, K., *Metall Trans,* **A17**, 53, 1986; *ISIJ Int.*, **29**, 353, 1989

Miyazaki, S., Otsuka, K. and Wayman, C.M., *Acta Metall.*, **37**, 1873, 1989

Miyazaki, S., Sugaya, Y. and Otsuka, K., *MRS International Meeting on Advanced Materials*, **9**, 251, 1989

Moberly, W.J. and Melton, K.N., in *Engineering aspects of Shape Memory Alloys*, eds. Duerig, T.W., Melton, K.N., Stockel, D., and Wayman, C.M., Buttherworth-Heinemann Ltd., Boston, p46, 1990

Movchan, B.A. and Demchishin, A.V., *Phy. Met. Metallogr.*, **28**, 83, 1969

Muddle, B.C. and Traill, R.M., in *Shape Memory Materials'94*, ed. Chu Y. and Tu, H., p689, International Academic Publishers, Beijing, 1994

Murakami, M., *Thin Solid Films*, **69**, 105, 1979; *CRC Critical Reviews in Solid State and Materials Science*, **11**, 317, 1984

Nakata, Y., Tadaki, T., Sakamoto, H., Tanaka, A. and Shimizu, K., *J. de Physique IV*, **5**, C8-671, 1995

Nishida, M. and Honma, T., *Scripta Metall.*, **18**, 1293, 1984

Nishida, M. and Wayman, C. M., *Materials Science and Engineering*, **93**, 191, 1987

Nishida, M., Wayman, C.M. and Honma, T., M*etall. Trans.*, **A17**, 1505, 1986; *Metall. Trans.*, **A18**, 785, 1987

Nishida, M., Wayman, C.M., Kainuma, R. and Honma, T., *Scripta Metall.*, **20**, 86, 899, 1986

Miura, S., Meada, S. and Nakanishi, N., *Phil Mag.* **30**, 565, 1974

Nix, W.D., *Metall. Trans.*, **A20**, 2217, 1989

Oding, I.A., Ivanova, V.S., Burdukskii, V.V. and Geminov, V.N., *Creep and Stress Relaxation in Metals*, Oliver and Boyd, Edinburgh and London, 280, 1965

Ohba, T., Otsuka, K. and Sasaki, S., *Martensitic Transformations*, p317, Tans. Tech. Publications, Brookfield, VT, 1990

Ohring, M., *Materials Science of Thin Films*, p403, 1992

Olander, A., *Z. Kristall*, **83A**, 145, 1932

Ortin, J. and Planes, A., *J. de Physique IV*, **4**, C4-13, 1990

Otuska, K., in *Engineering aspects of Shape Memory Alloys*, eds. Duerig, T.W., Melton, K.N., Stockel, D., and Wayman, C.M., Buttherworth-Heinemann Ltd., Boston, 1990

Otsuka, K. and Shimizu, K., *Scripta Metall.*, **11**, 757, 1972; *International Metal Review*, **31**, 93, 1986

Otsuka, K., Sawamura, T. and Shimizu, K., *Phys. Stat. Sol.*, **A5**, 457, 1971

Pan, J.T. and Belch, I., *J. Appl. Phys.*, **55**, 2874, 1984

Park, S.H., Yue, S. and Jonas, J.J., *Metall. Trans.*, **23A**, 1641, 1992

Perkins, J. and Sponholz, R.O., *Metall. Trans.*, **15A**, 313, 1984

Plunkett, P.V., Johnson, R.M. and Wiseman, C.D., *Thin Solid Films*, **64**, 121, 1979

Priest, J., Caswell, H.L. and Budo, Y., *Vacuum*, **12**, 301, 1962

Proft, J.L., Melton, K.N. and Duerig, T.W., *Proc. Inter. MRS Conference*, Tokyo, Japan, 1987

Pu, Z., Tseng, H.K., and Wu, K.H., *Porc of SPIE, Smart Materials*, **2189**, 289, 1994

Pulker, H.K., *Thin Solid Films*, **89**, 91, 1982

Quandt, E., Halene, C., Holleck, H., Heit, K., Kohl, M. and Shlobmacher, *the 8th Int. Conf. on Solid-State Sensors and Actuators and Eurosensors IX*, Stockholm, 282-PA11, 1995

Rai, A.K. and Bhaattacharya, R.S., *Materials Science and Engineering*, **85**, 137, 1987

Ray, C.A., Sloan, C.L., Johnson, A.D., Busch, J.D. and Petty, B.R., *MRS Proceedings*, **276**, 161, 1992

Reed-Hill, R.E., and Abbraschian, R., *Physical Metallurgy Principles*, 3rd edition, PWS-KENT Publishing Company, Boston, 1992

Rottmayer, R.E. and Hoffman, R.W., *J. Vac. Sci. Technol.*, **8**, 151, 1971

Saburi, T., Nenno, S. and Fukuda, T., *J. the Less-Common Metals*, **125**, 157, 1986

Sakamoto, H., Otsuka, K. and Shimizu, K., *Scripta Metall.*, **11**, 607, 1977

Schlossmacher, P., *Materials Letters*, **31**, 119, 1997

Schroeder, T.A., and Wayman, C.M., *Scripta Metall.*, **11**, 225, 1977; *Acta Metall.*, **27**, 405, 1979

Schwarz, R.B., Petrich, R.R., and Saw, C.K., *J. of Non-Cryst. Solid*, **76**, 281, 1985

Scineider, S., Schroder, H., and Samwer, K., *Thin Solid Films*, **174**, 11, 1989

Shute, C.J. and Cohen, J.B., *Materials Science Engineering*, **A149**, 167, 1992

Sivokha, V.P., Savvinov, A.S., Voronin, V.P. and Khachin, V.N., *Phys. Met. Metall.*, **56**, 112, 1983

Smialek, J.L. and Hehemann, R.F., *Metall. Trans..*, **4A**, 1571, 1973

Smith, D.A. and Ibrahim, A., *MRS Symposium Proceedings*, **317**, 401, 1984

Su, Q., Kim, T., Zheng, Y. and Wuttig, M., *Proceedings of SPIE*, **2441**, 179, 1995

Sullivan, T.D., *Applied Phys. Lett.*, **55**, 2399, 1989

Sulonen, M.S., *Acta Metall.*, **12**, 749, 1964

Thoma, P., Blok, A. and Kao, M., in *Fundamental Aspects and Applications of SMA*, ed. Liu, C.T., Kunsmann, H., Otsuka, K. and Wuttig, M., MRS proceedings, 321, 1991

Thornburg, K.A., Dunne, D. P. and Wayman, C. M., *Metall. Trans.*, **2**, 2033, 1971

Thornton, J.A., *Annual Review of Materials Science*, **7**, 239, 1977

Thornton, J.A. and Hoffman, D.W., *J. Vac. Sci. Technol.*, **A3**, 576, 1985

Thorton, J.A., Tabock, J. and Hoffman, D.W., *Thin Solid Films*, **64**, 111, 1979

Ullakko, K., Huang, J.K., Kokorin, V.V. and O'Handley, R.C., *Scripta Mater.*, **36**, 1133, 1997

van Vucht, J.H.N., *J. the Less-Common Metals*, **11**, 308, 1966

Vanloo, F.J.J., *J. the Less-Common Metals*, **57**, 171, 1978

Vicentini, B., Rondelli, G., Cigada, A. and Turisini, G., *Shape Memory Alloy'86*, p2147, China Academic Publisher, Beijing, 1986

von Pressig, F.J., *J. Applied Physics*, **66**, 4262, 1989

Walker, J.A., Gabriel, K.J. and Mehaegany, M., *5th int. Conference on Solid State sensors and Actuators*, Montreanx, Swiss, p123, 1989; *Sensors Actuators*, **A21-A23**, p243, 1990

Walles, B., Chang, L. and Grummon, D.S., *MRS Research Society Symposium Proceedings*, **V246**, 349, 1992

Wasilewski, R., *NASA Technical Report*, 1972; *Scripta Metall*, **4**, 127, 1971

Wasilewski, R., Betler, S.R., Hanlon, J.E. and Worden D., *Metall Trans*, **2**, 229, 1971

Wayman, C.M., *Nondiffusive Phase Transformations*, in *Physical Metallurgy*, ed. Cahn, R.W. and Haasen, P., **3rd Edition**, p1035, Elsevier Sceince Publishers BV, 1983; *The International Symposium on Shape Memory Alloys*, ed. Chu, Y.Y., Guilin, China, p59, 1986; *Progress in Materials Sciences*, **36**, 203, 1992

Wayman, C.M. and Duerig, T.W., in *Engineering aspects of Shape Memory Alloys*, eds. Duerig, T.W., Melton, K.N., Stockel, D., and Wayman, C.M., Buttherworth-Heinemann Ltd., Boston, 1990

Wu, S.K. and Wayman, C.M., *Acta Metall.*, **37**, 2085, 1989

Wu, S.K., Lin, H.C. and Chou, T.S., *Acta Metall. Mater.*, **38**, 95, 1990

Wechesler, M.S., Liebermann, D.S. and Read, T.A., *Trans. AIME*, **197**, 503, 1953

Xie, C., Zhao, L. and Tei, T., *Scripta Metall.*, **24**, 1753, 1990

Yeh, M.T., Kao, H.P. and Hsu, S.E., in *Shape Memory Materials'94*, ed. Chu Y. and Tu, H., p561, International Academic Publishers, Beijing, 1994

Zhang, J. and Grummon, D.S., *MRS Fall Meeting*, 1996, Boston, MA.

Zhang, C., Zhao, L, Duerig, T.W. and Wayman, C.M., *Scripta Metall.*, **24**, 1807, 1990

Zhao, Z., M.S. Thesis, Michigan State University, 1995

Zheng, X. and Dodd, R.A., *Nuclear Instrument Methods*, 1994

Zingu, E.C. and Mofokeng, B.J., *MRS Symposium Proceedings*, **308**, 85, 1993

Table 1. A comparison of NiTi SMA with piezoelectric, electric, and bimetal actuators (after Johnson, 1991)

Principle	Maximum work energy density (J/cm^3)	Drive conditions	Biocompatibility	Shrinkability	Power/Weight ratio
DC magnet motor	0.9	B = 1.5 T	Yes	Poor	Low
Microelectrostatic	0.4	E = 300 V/μm	No	Good	High
Piezoelectric	4.8×10^{-4}	E = 30 V/μm	No	Good	High
NiTi SMA	10.4	P = 1.4 W/mm^{-3}	Yes	Good	High

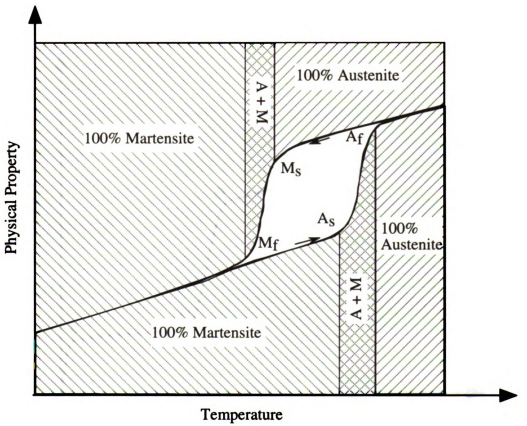

Figure 2-1 A schematic of martensitic transformation showing four characteristic transformation temperatures and structure within certain temperature intervals.

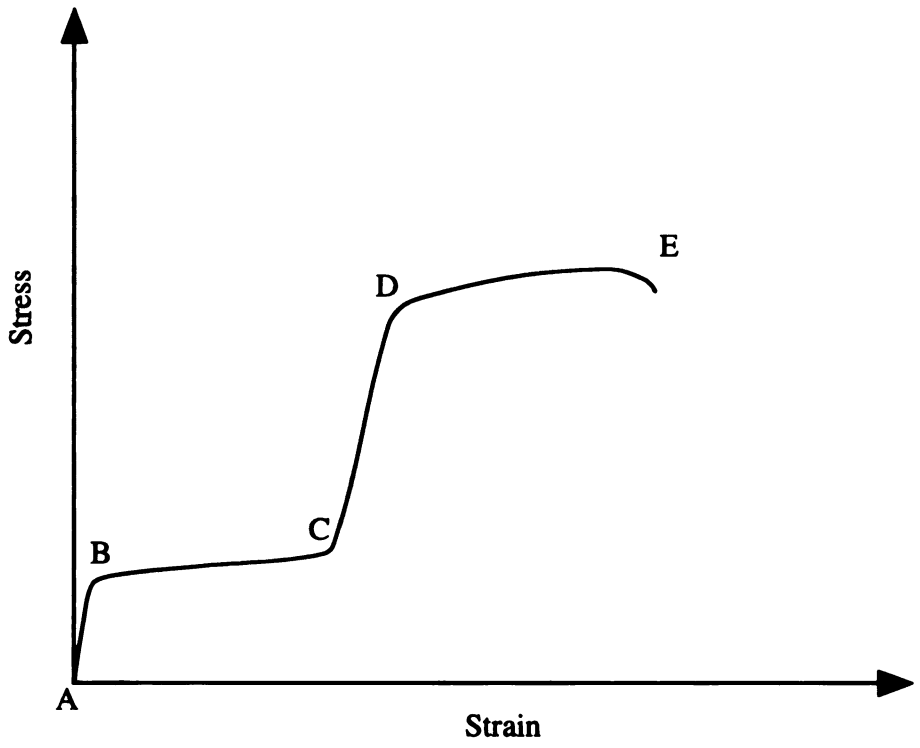

Figure 2-2 Deformation behavior of a martensite material.
AB: elastic deformation of multi-variant martensite;
BC: plastic deformation of martensite by reorientation of the martensite variants;
CD: elastic deformation of fully detwinned martensite;
DE: plastic deformation of fully detwinned martensite by slip

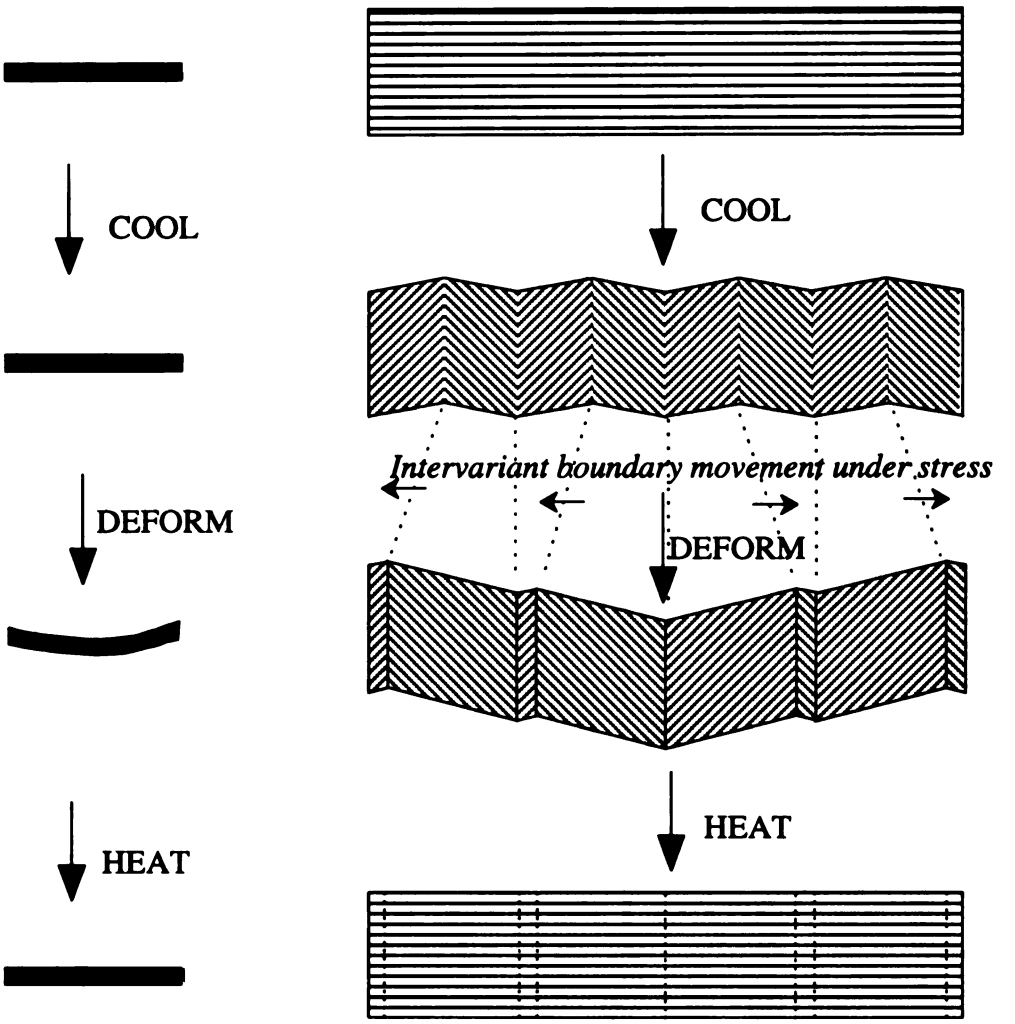

Figure 2-3 A schematic of SME in two-variant martensite. The left side shows the macroscopic change of an SMA material by heating/cooling and applied stresses, the right side shows the corresponding microscopic response.

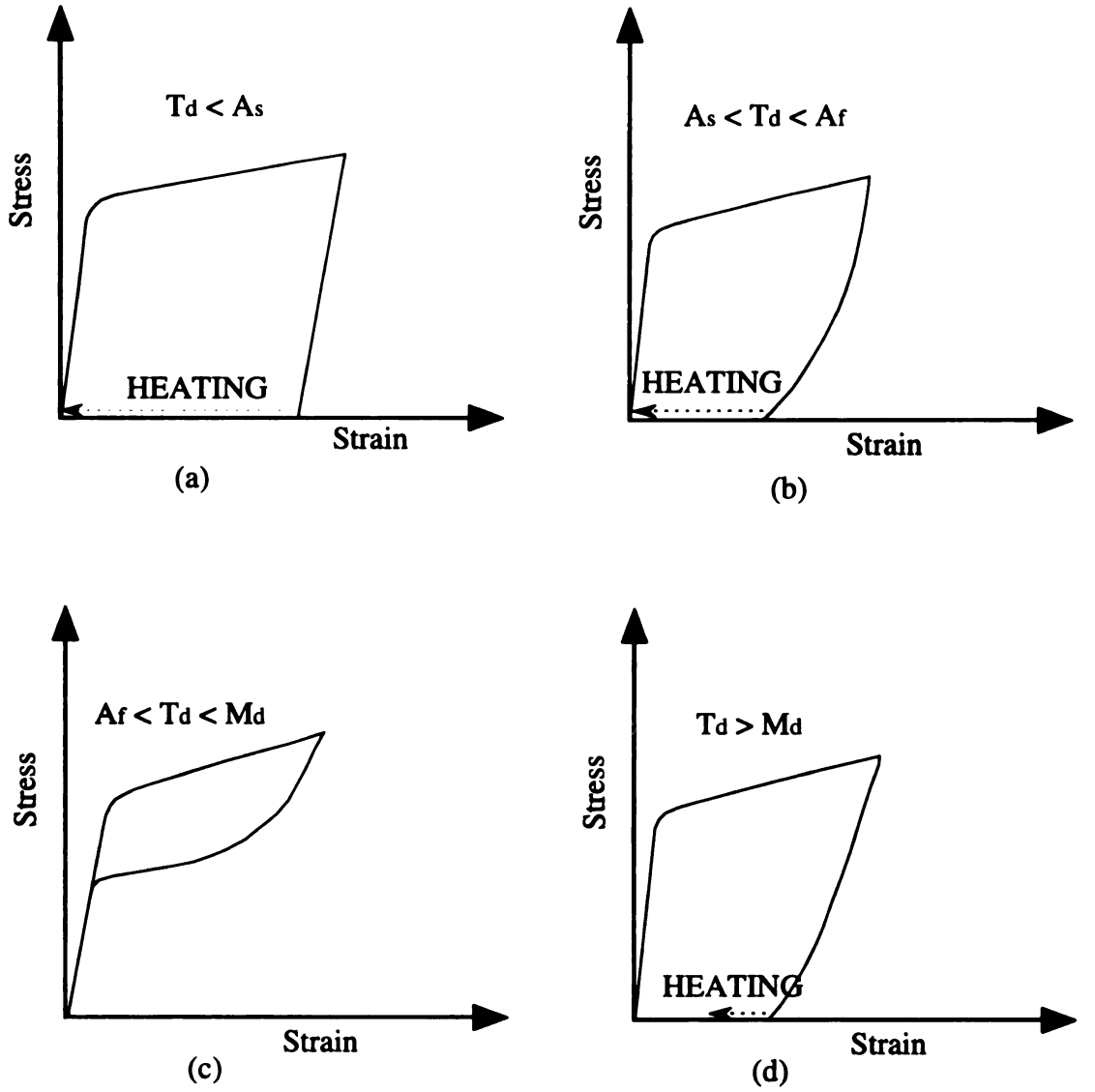

Figure 2-4 Deformation behavior of an austenite material at different temperatures:
(a) $T_d < A_s$, all the strain is recovered by heating the material to above A_f;
(b) $A_s < T_d < A_f$, part of the strain is recovered spontaneously upon unloading, while the rest is recoverable by heating the material to above A_f;
(c) $A_f < T_d < M_d$, all the strain is recovered spontaneously upon unloading, which is perfect psuedoelasticity;
(d) $T_d > M_d$, permanent strain is introduced by slip.

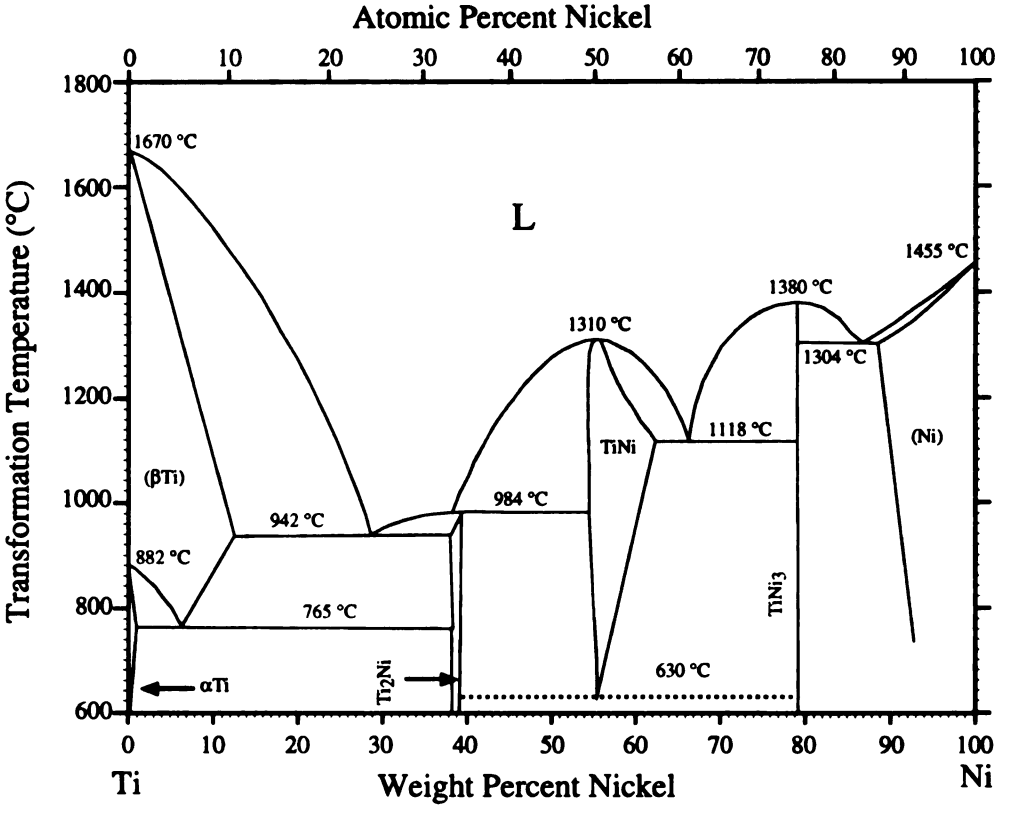

Figure 2-5 Binary Ni-Ti phase diagram [Massalski, 1987]

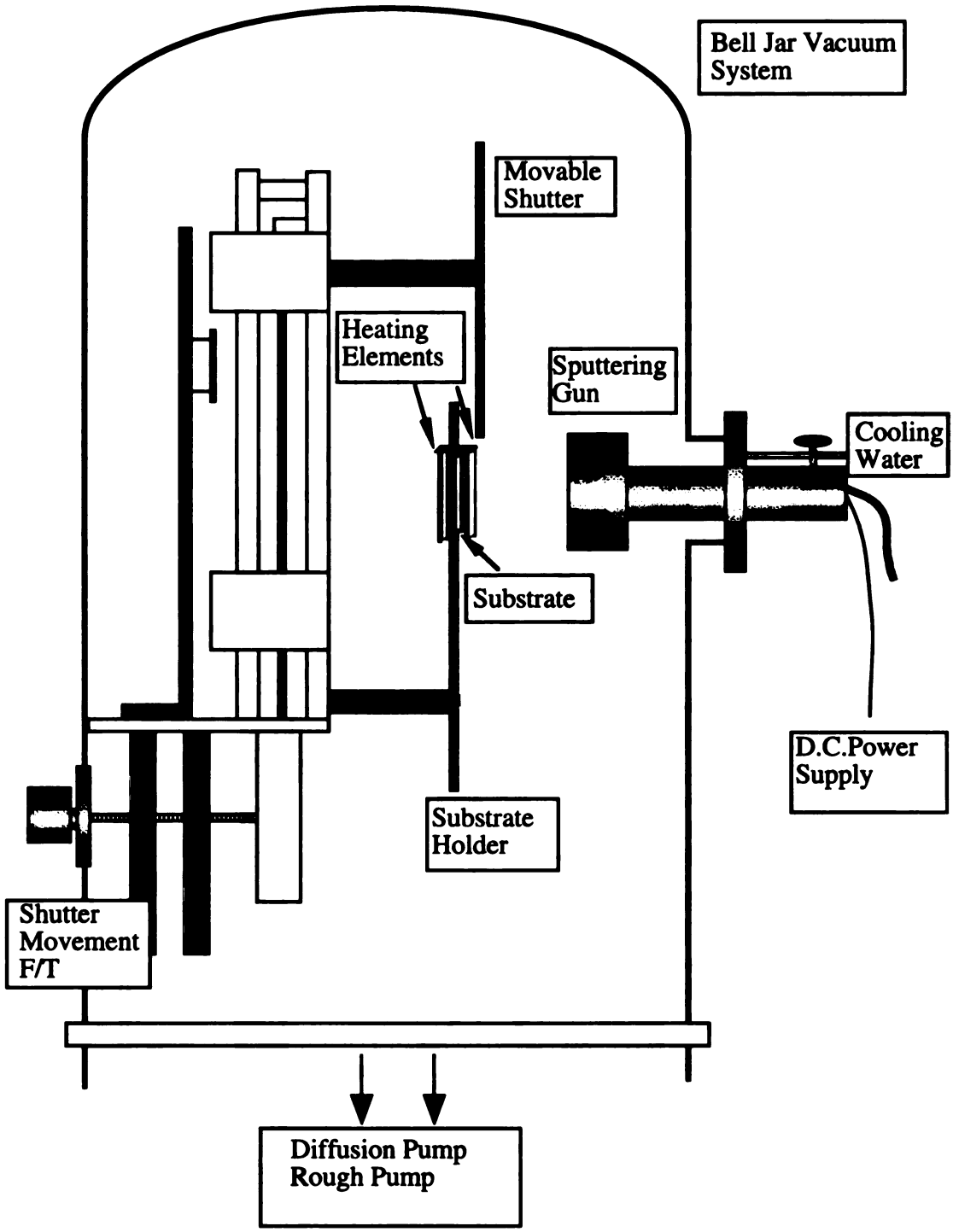

Figure 3-1 A schematic showing the d.c. megnetron sputtering apparatus.

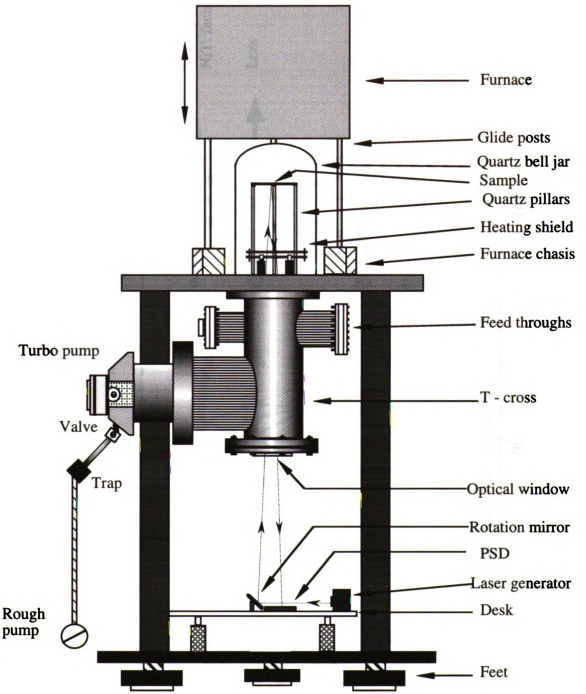

Figure 3-2 Sketch of apparatus for stress measurement by wafer-curvature method.

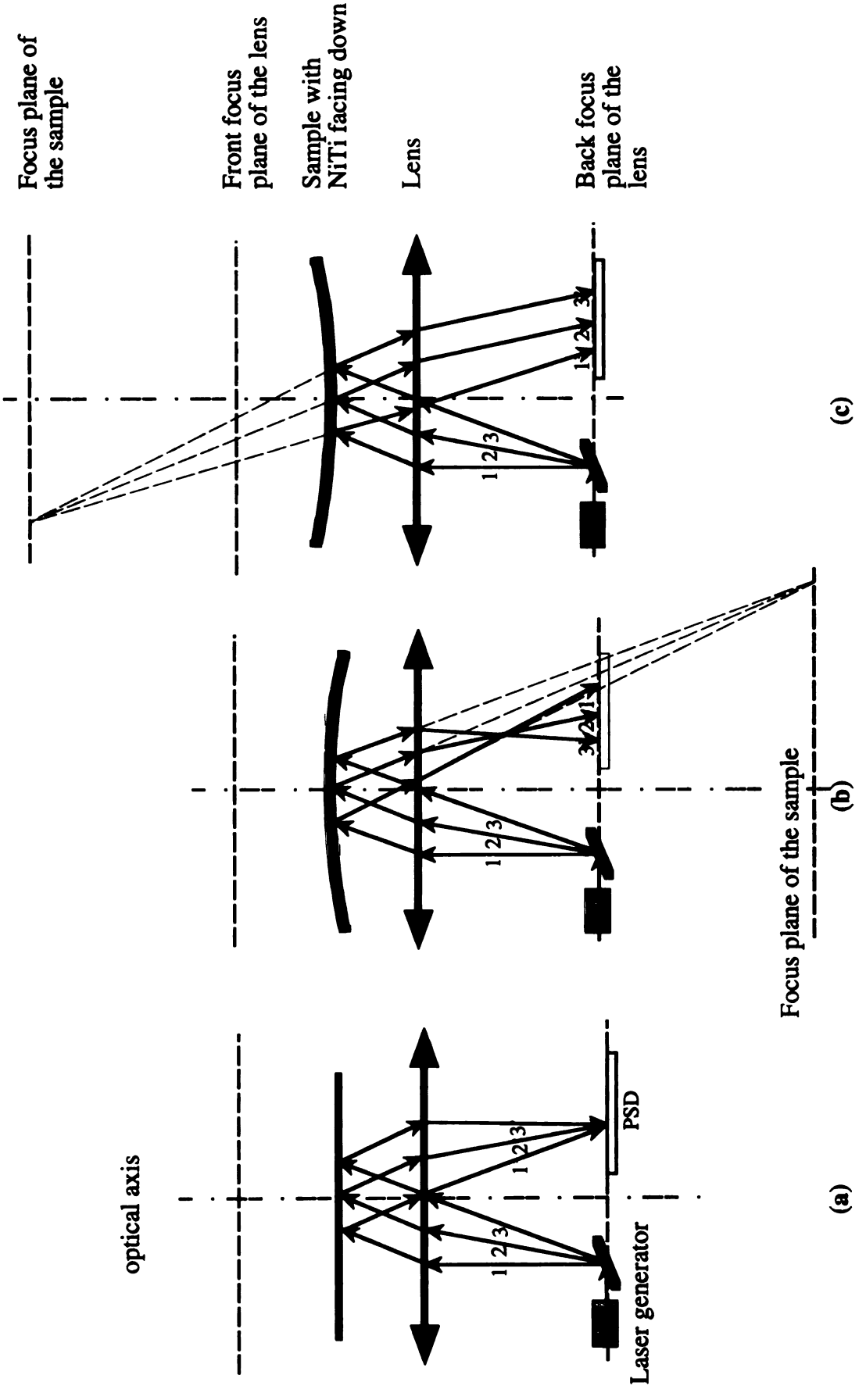

Figure 3-3 Optical paths for **(a)** flat wafer (stress-free), **(b)** concave wafer (tensile stress), and **(c)** convex wafer (compressive film stress).

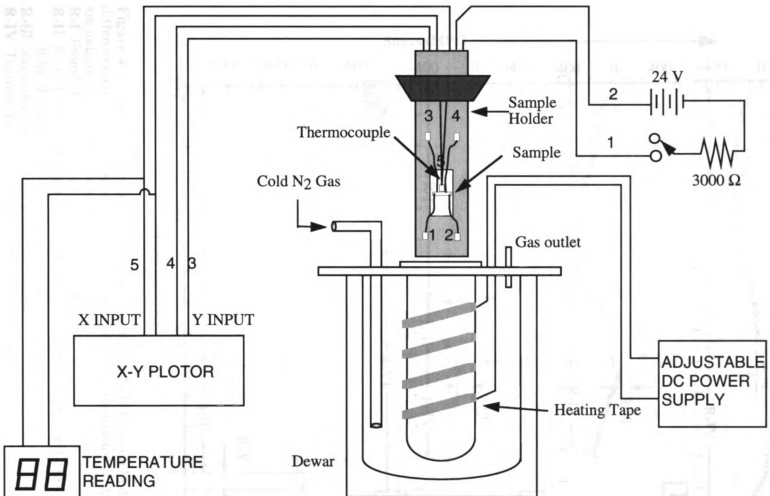

Figure 3-4 Schematic drawing showing apparatus for transformation temperature determination by electrical resistivity measurement.

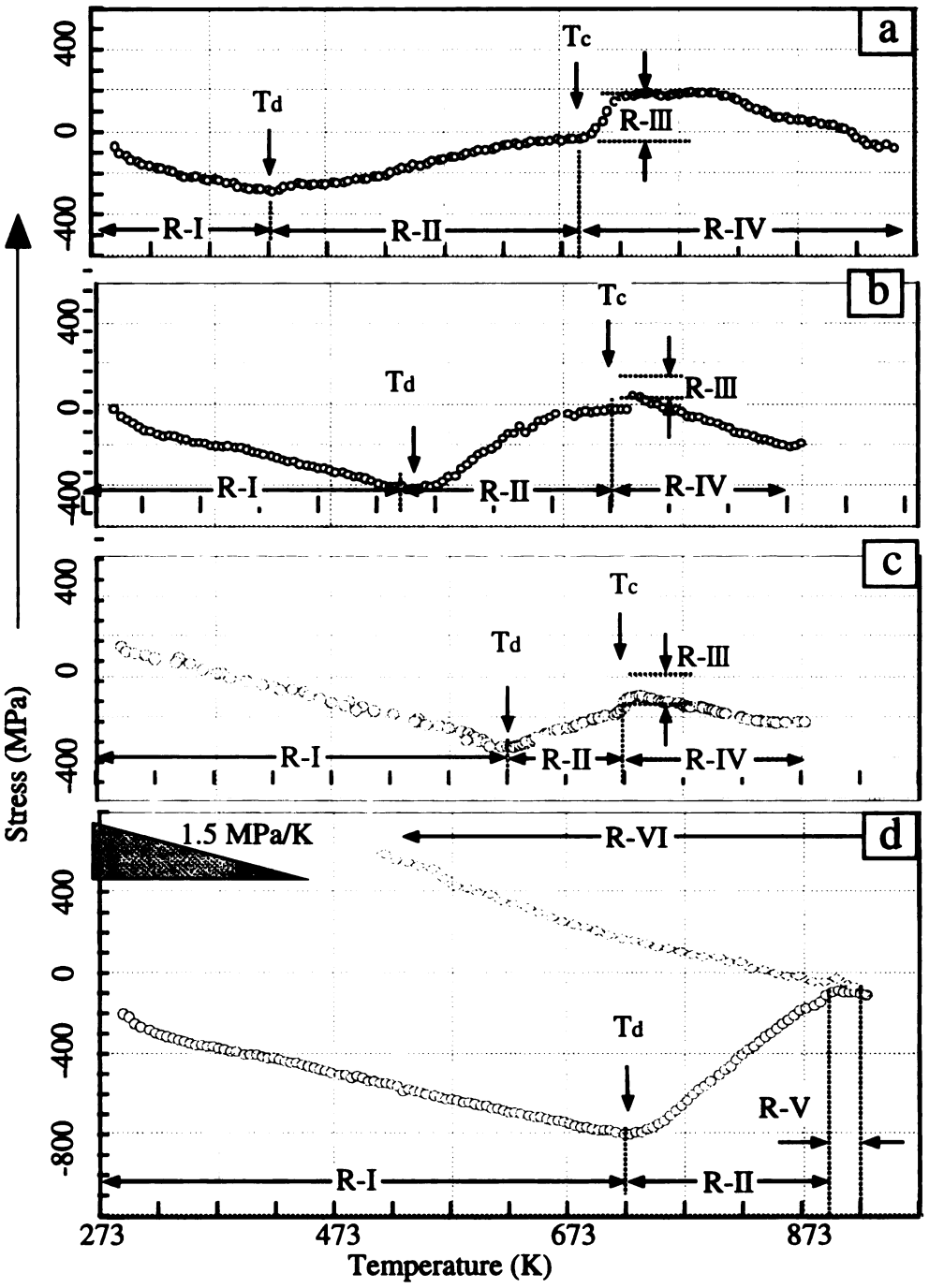

Figure 4-1 Stress - temperature curves of as-sputtered NiTi films on Si deposited at different temperatures. Deposition temperature Td and crystallization temperature Tc are indicated by arrows in each figure.
R-I: From RT to Td, thermal Stress development;
R-II: From Td to Tc for amorphous or partially amorphous films, or Td to ~893 K for fully crystalline films, stress relaxation;
R-III: Stress development due to crystallization;
R-IV: Thermal stress development after crystallization;
R-V: Steady-state stress when temperature exceeds 893 K for fully crystalline films;
R-VI: Thermal stress development due to fast cooling.

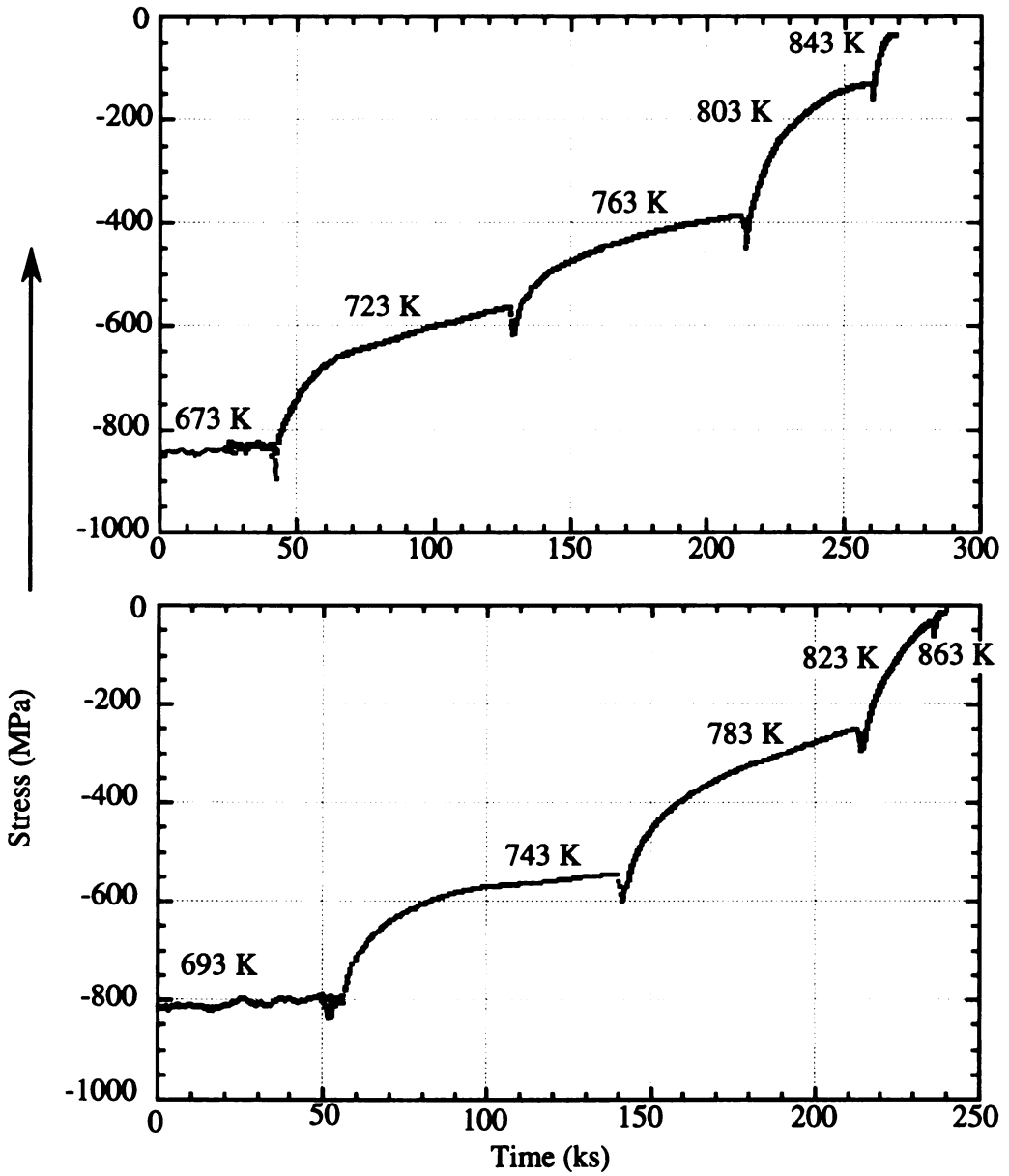

Figure 4-2 (a,b) Stress variation of two crystalline NiTi films on Si deposited at 693 K during thermal treatments with time starting at the first isothermal annealing.

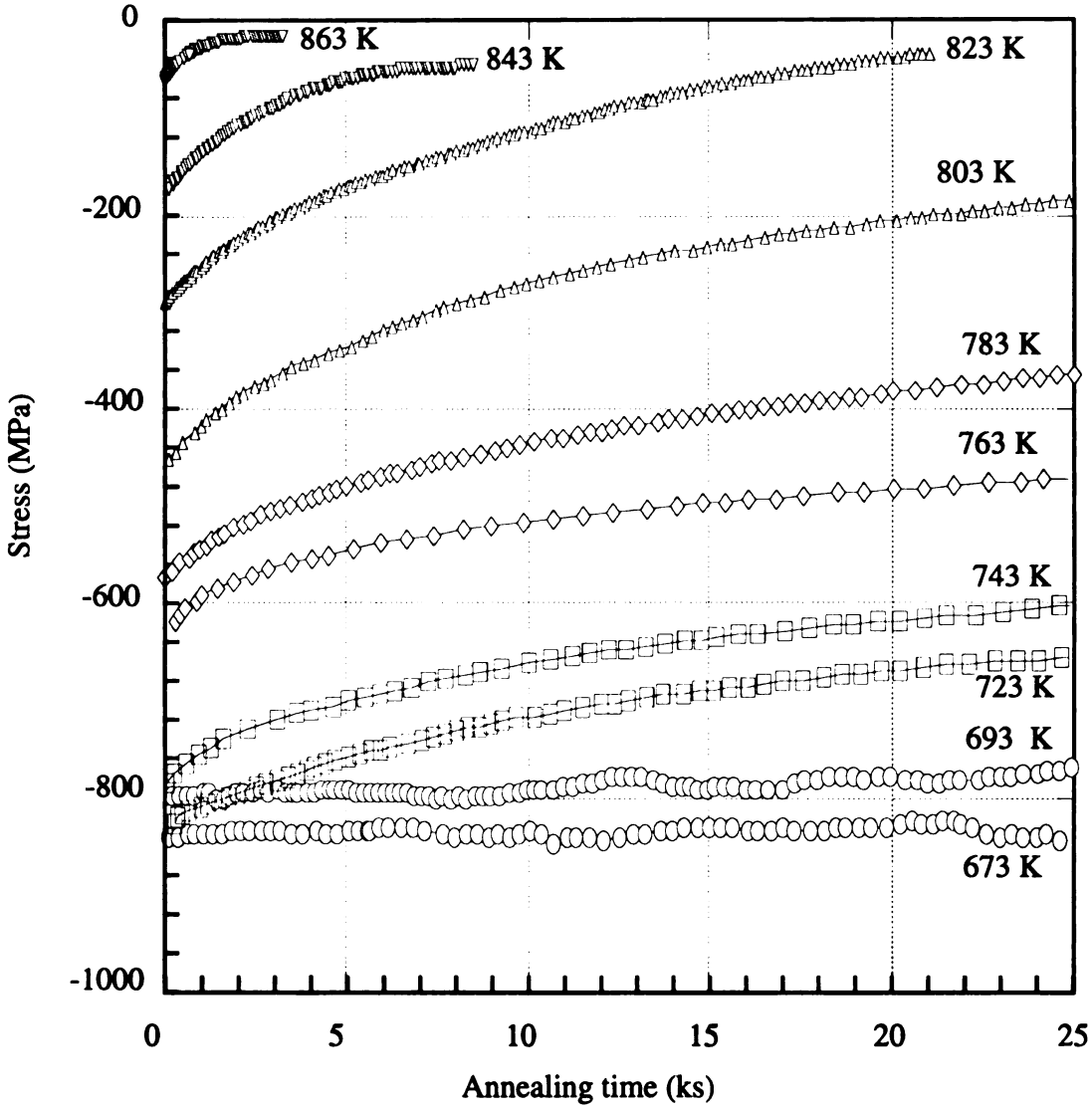

Figure 4-2(c) Stress relaxation in as-sputtered NiTi films on Si deposited at 693 K during the first 25 ks isothermal holding at different temperatures. Timing started at each temperature.

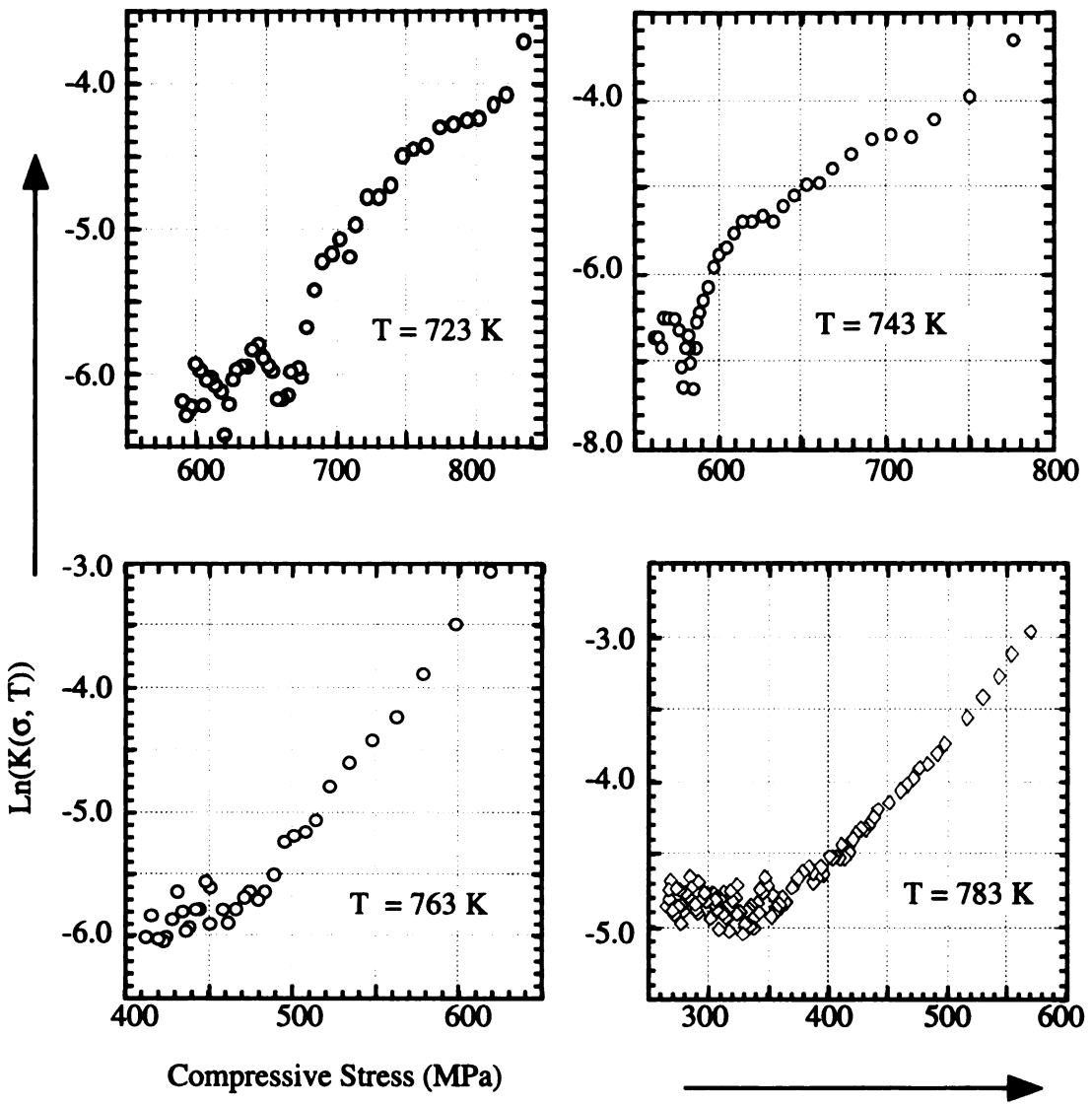

Figure 4-3 Plots of *ln(k(σ, T)) vs.* σ from stress relaxation curves for the crystalline films deposited at 693 K and isothermally annealed at different temperatures (to be continued).

Figure 4-3 (cont'd)

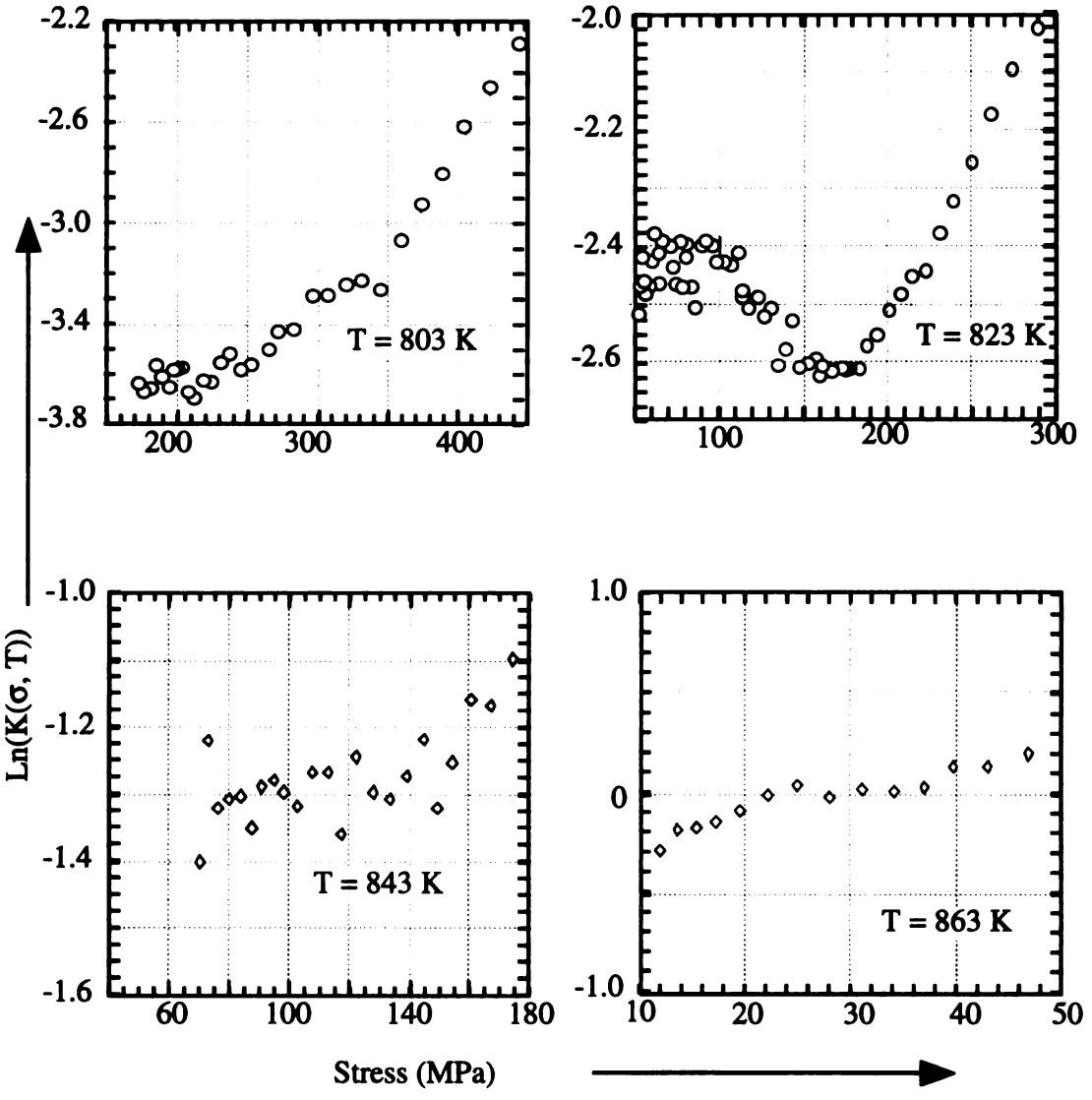

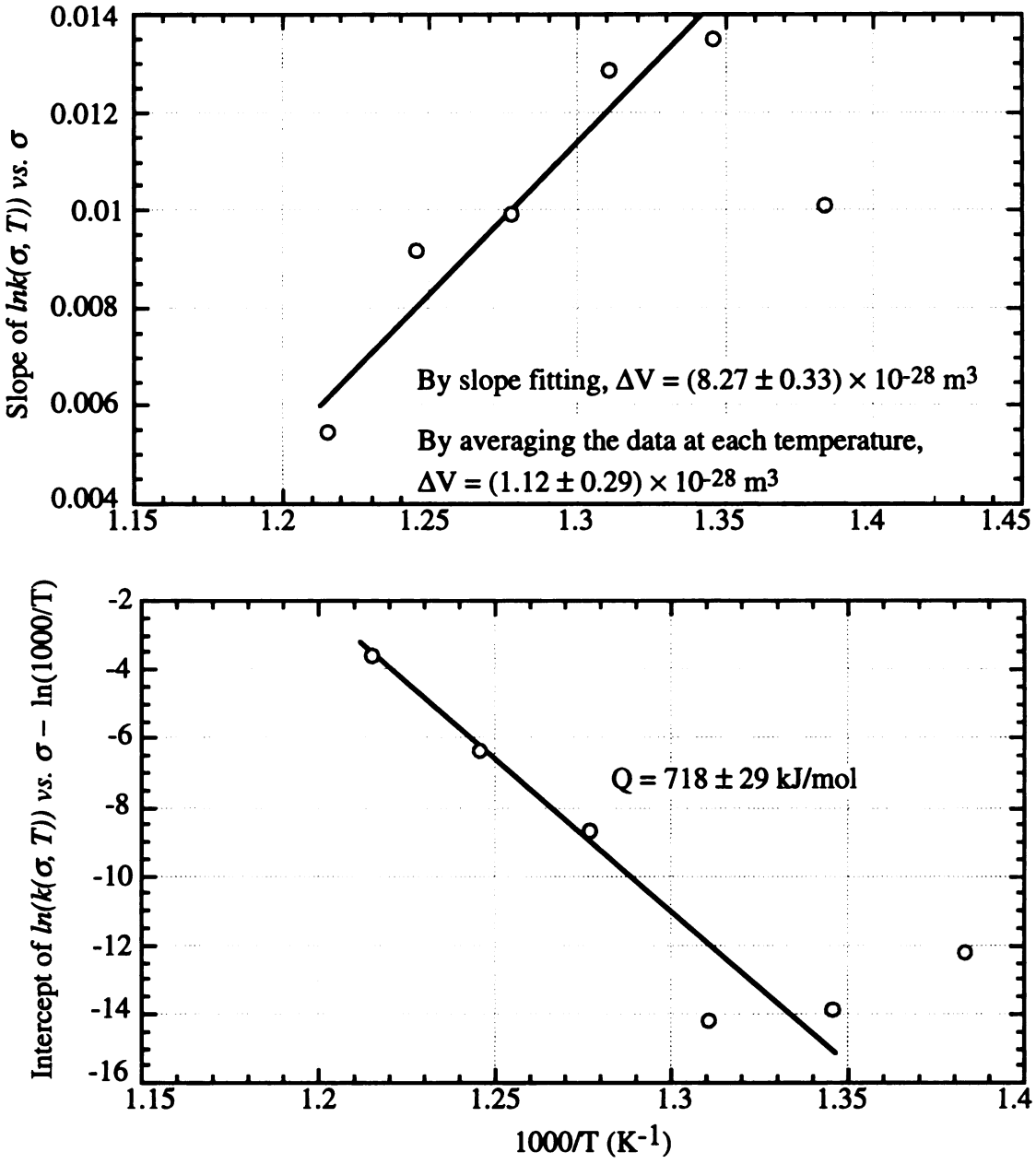

Figure 4-4(a) Calculations of activation volume (upper) and activation energy (lower) based on the intercepts and slopes in Figure 4-3 for the first stage of stress relaxation in fully crystalline films.

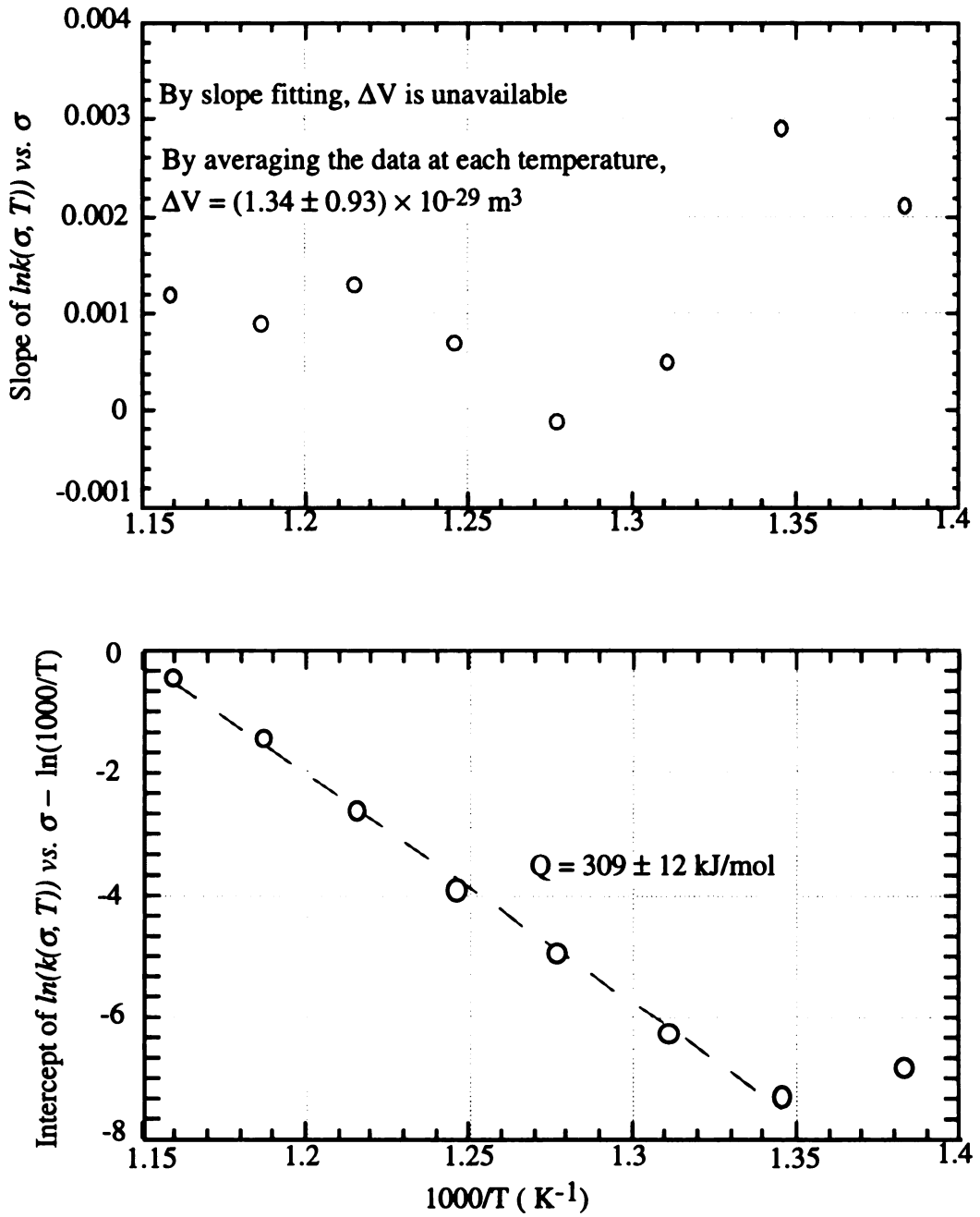

Figure 4-4(b) Calculation of activation volume (upper) and activation energy (lower) calculations based on the intercepts and slopes in Fig. 4-3 for the second stage of stress relaxation in fully crystalline films.

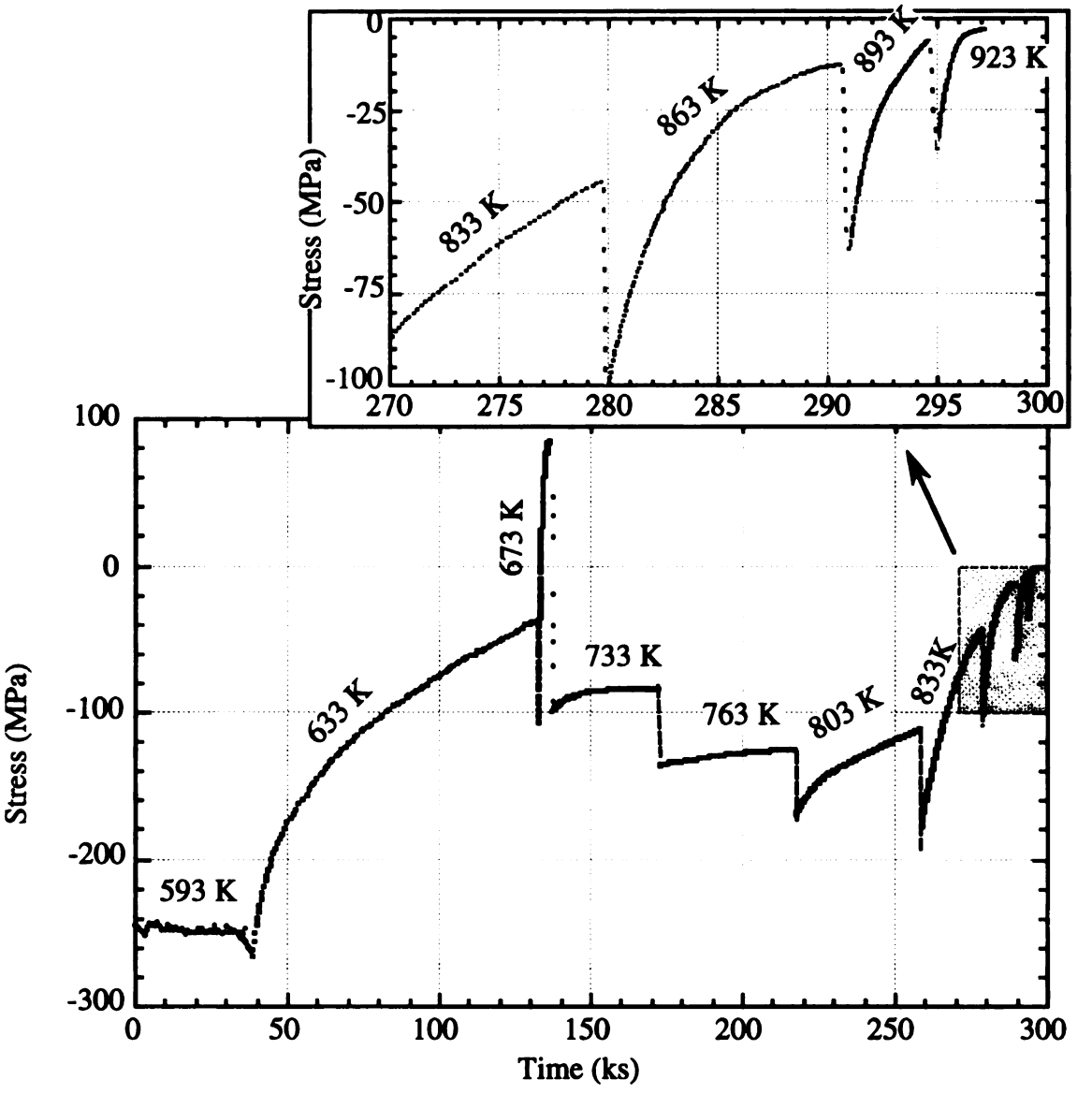

Figure 4-5(a) Stress variation of an initially partially crystalline NiTi on Si deposited at 623 K during thermal treatment with time starting at the first isothermal annealing.

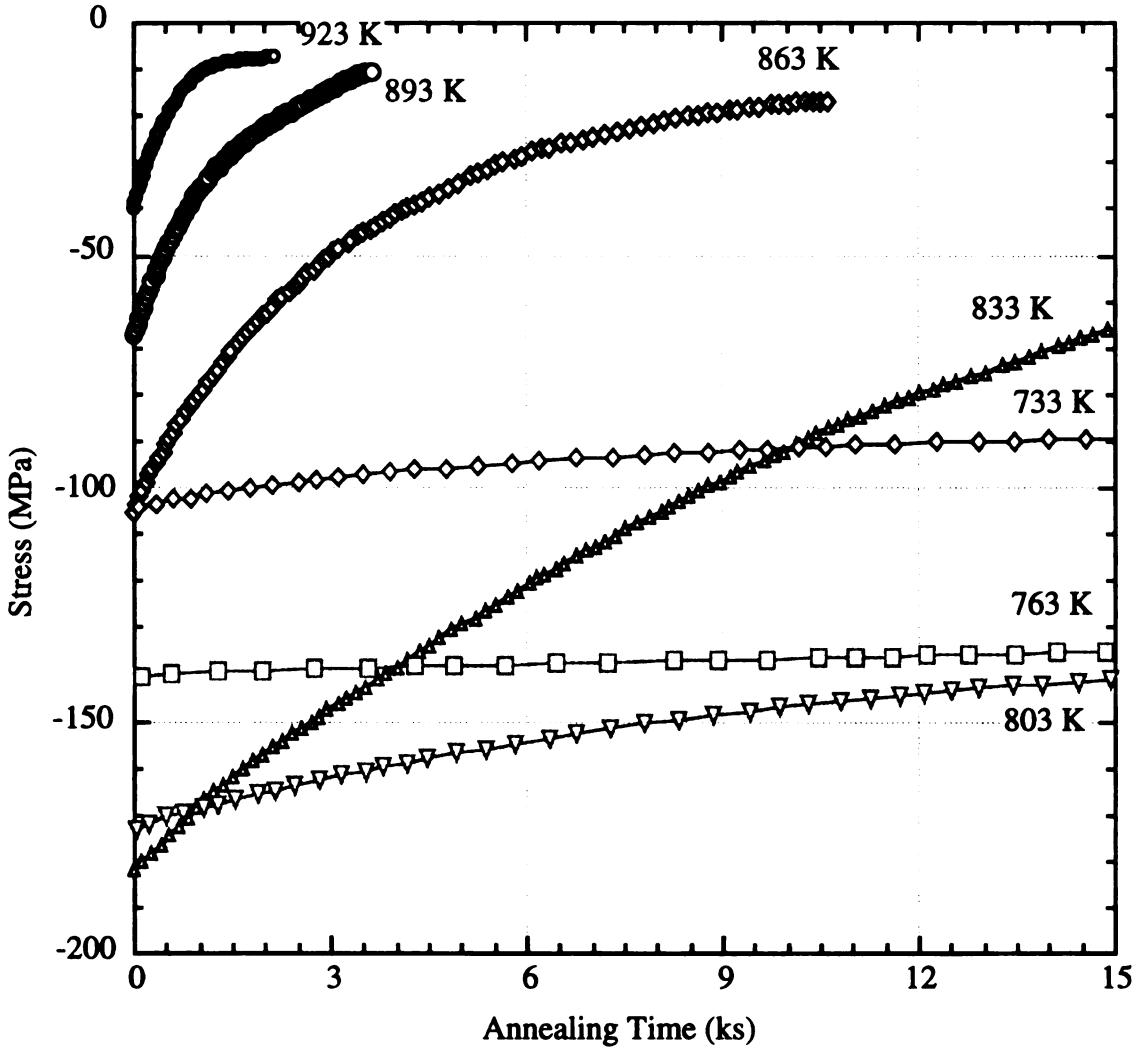

Figure 4-5(b) Stress relaxation curves of the NiTi film on Si deposited at 623 K during the first 15 ks of isothermal holding at different temperatures after the film became fully crystalline. Timing started at each temperature.

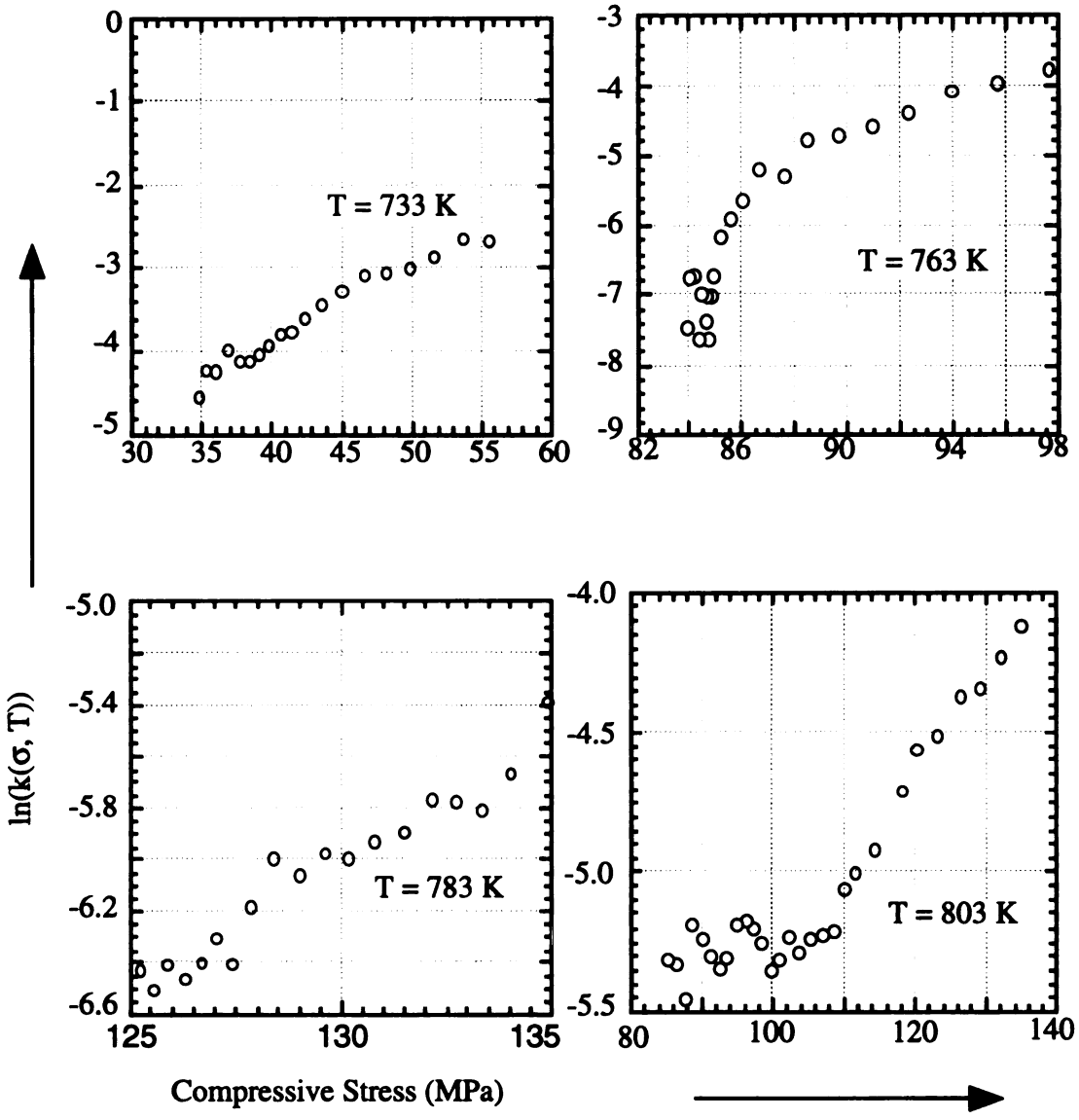

Figure 4-6 Plots of *ln(k(σ, T)) vs.* σ from the stress relaxation curves for the initially partially crystalline films deposited at 623 K and isothermally annealed at different temperatures (to be continued).

Figure 4-6 (cont'd)

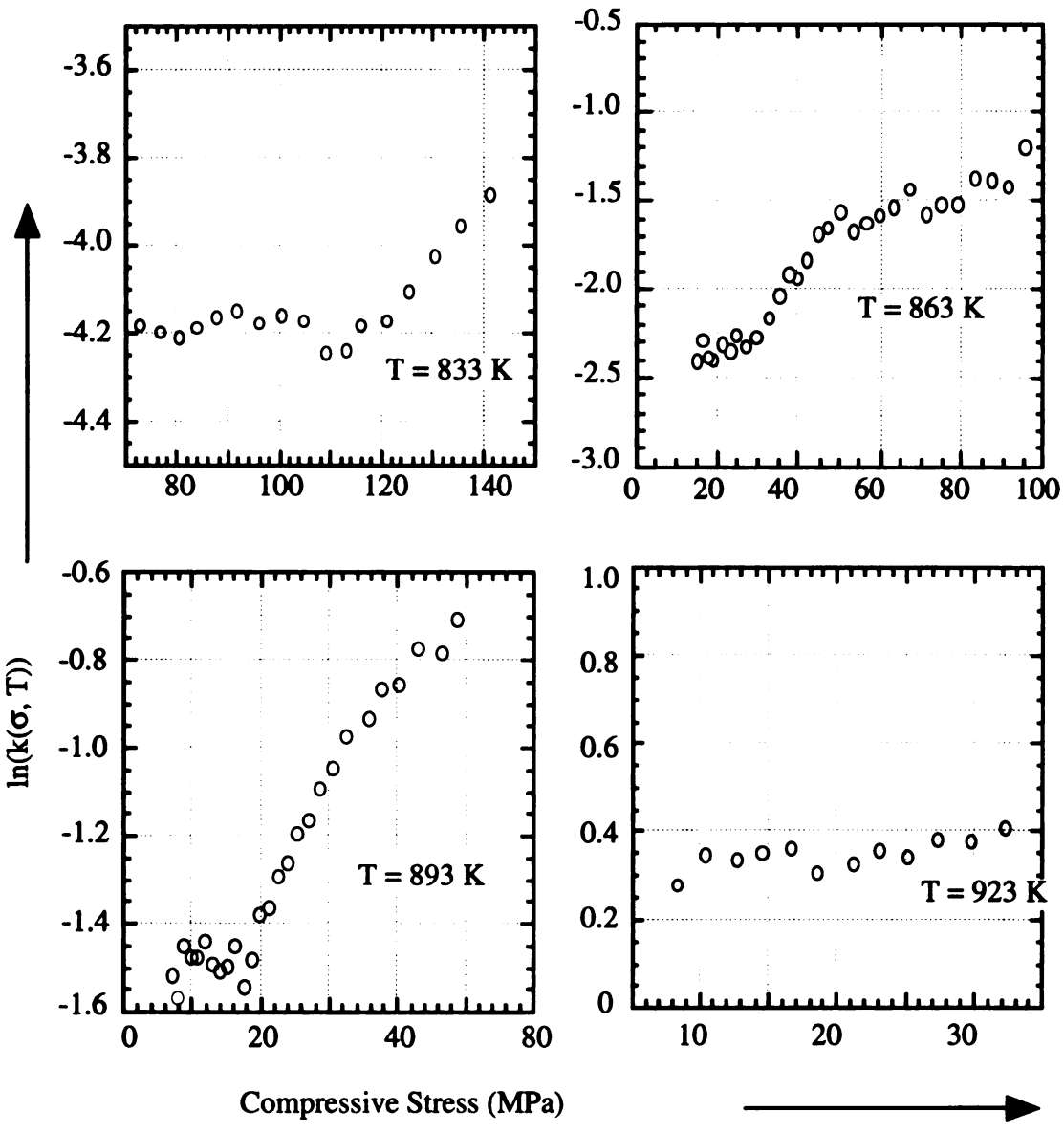

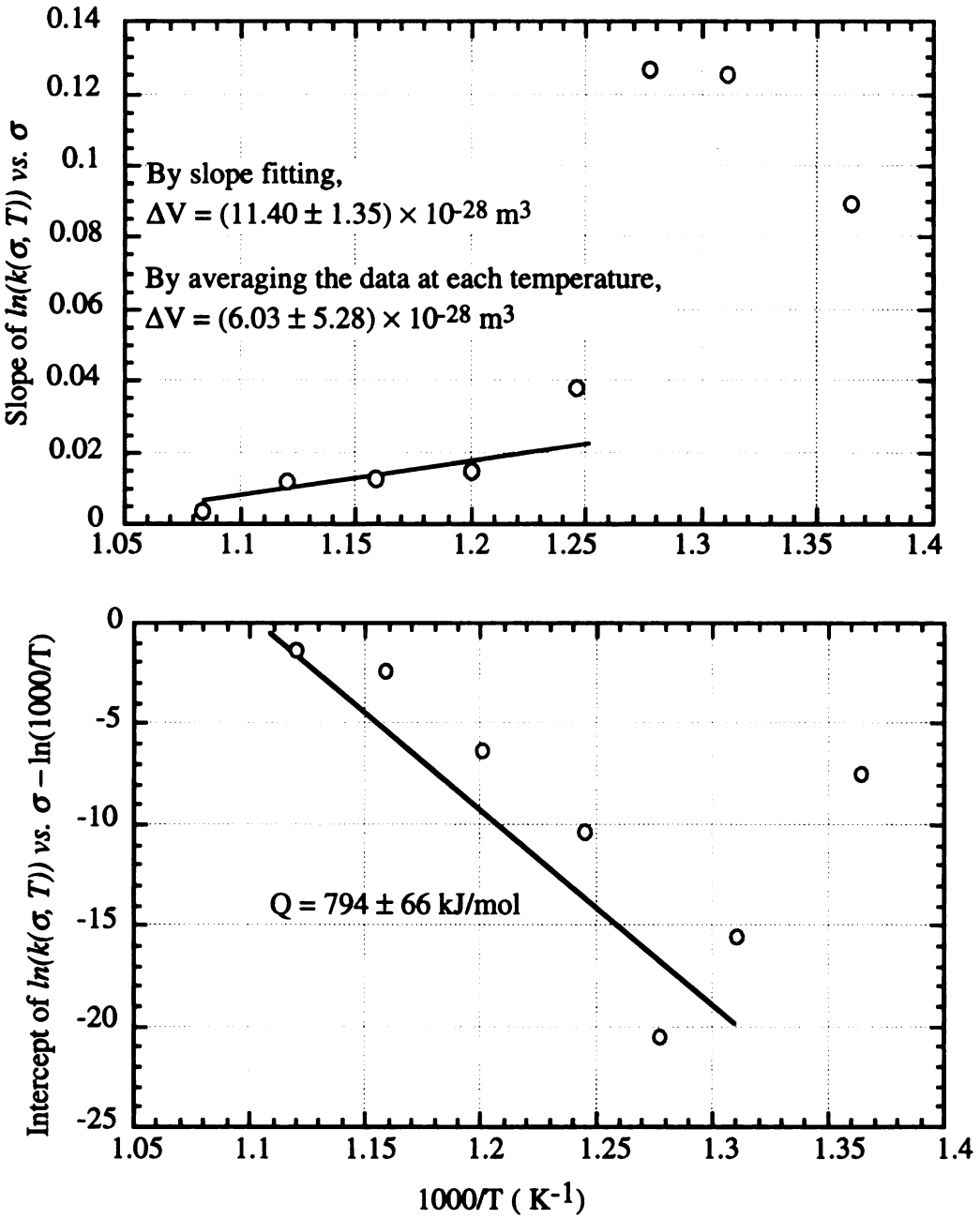

Figure 4-7(a) Diffusion volume (upper) and activation energy (lower) calculations based on the intercepts and slopes in Fig. 4-6 for the first stage of stress relaxation after crystallization of a partially crystalline film.

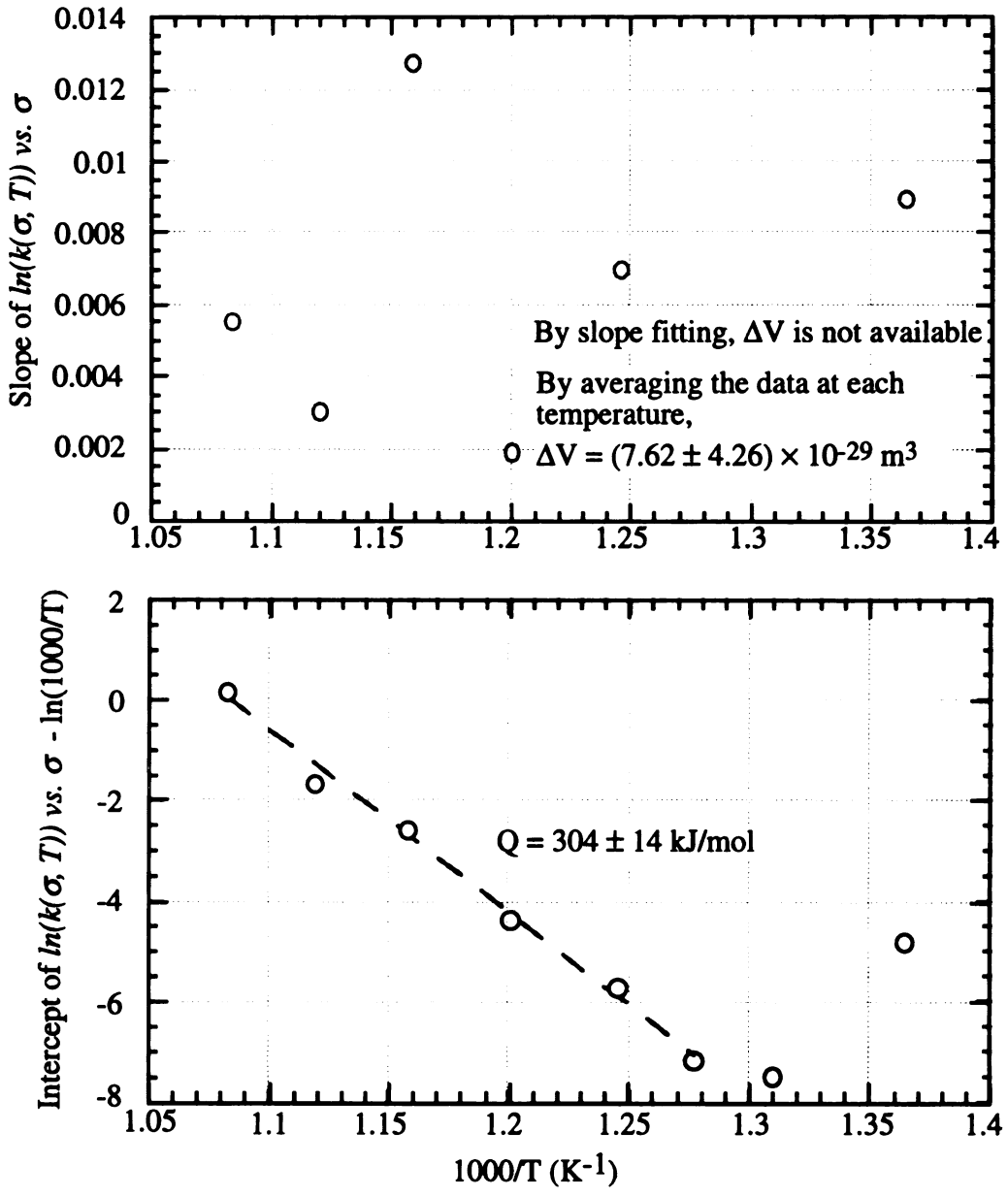

Figure 4-7 (b) Calculations of activation volume (upper) and activation energy (lower) based on the intercepts and slopes in Fig. 4-6 for the second stage of stress relaxation after crystallization of the initially partially crystalline film.

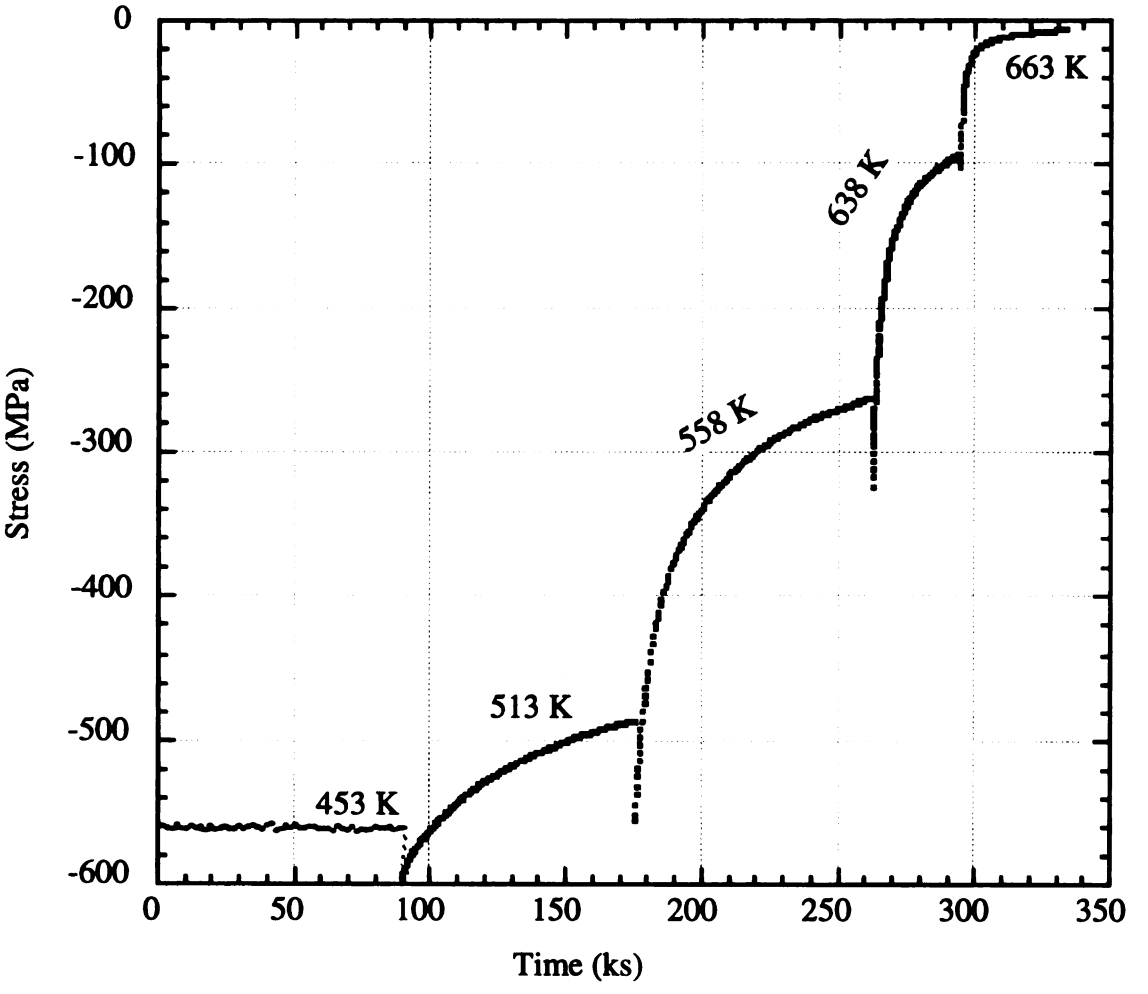

Figure 4-8(a) Stress relaxation of an amorphous NiTi film on Si deposited at 473 K during thermal treatment with time starting at the first isothermal annealing.

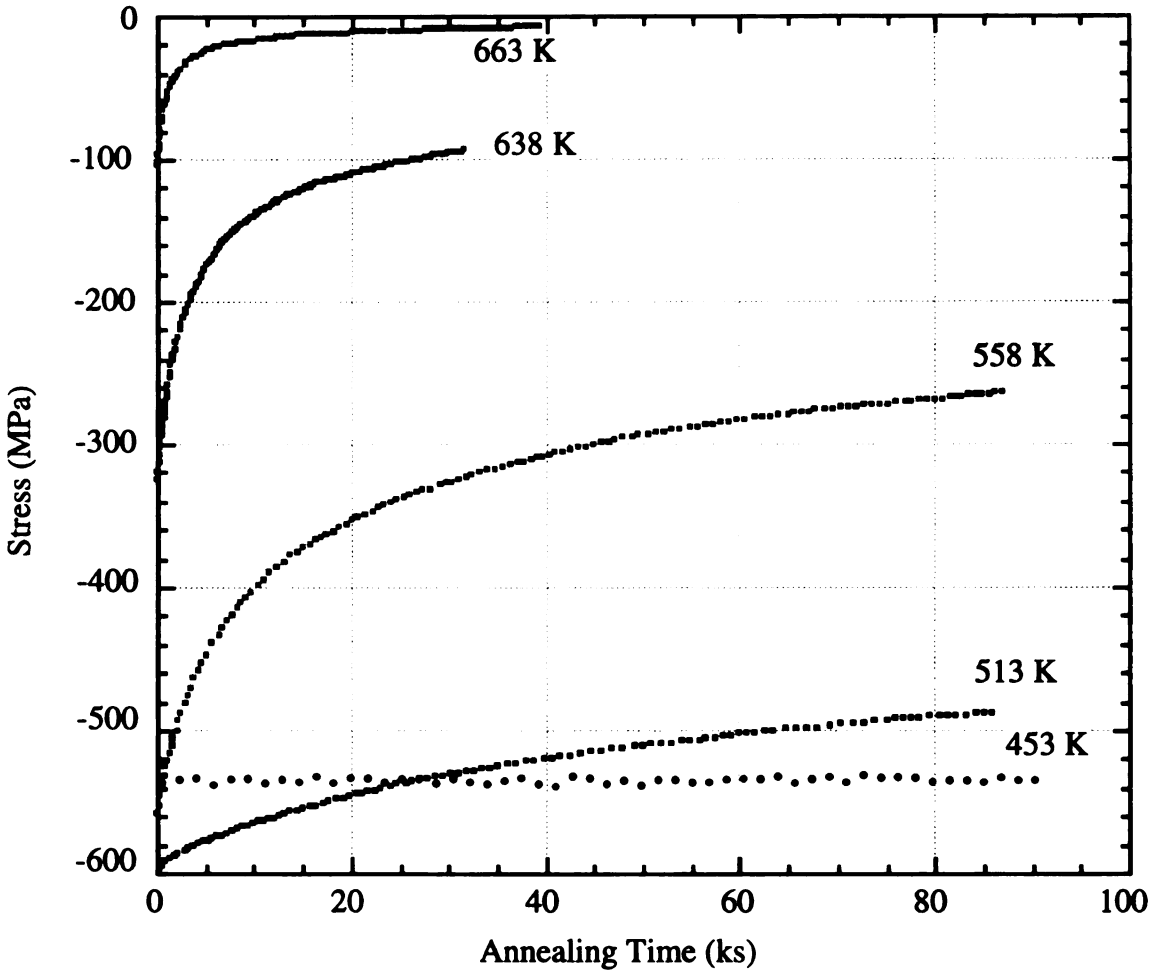

Figure 4-8(b) Stress relaxation curves of the amorphous NiTi on Si deposited at 473 K and isothermally annealed at different temperatures with time starting each isothermal annealing.

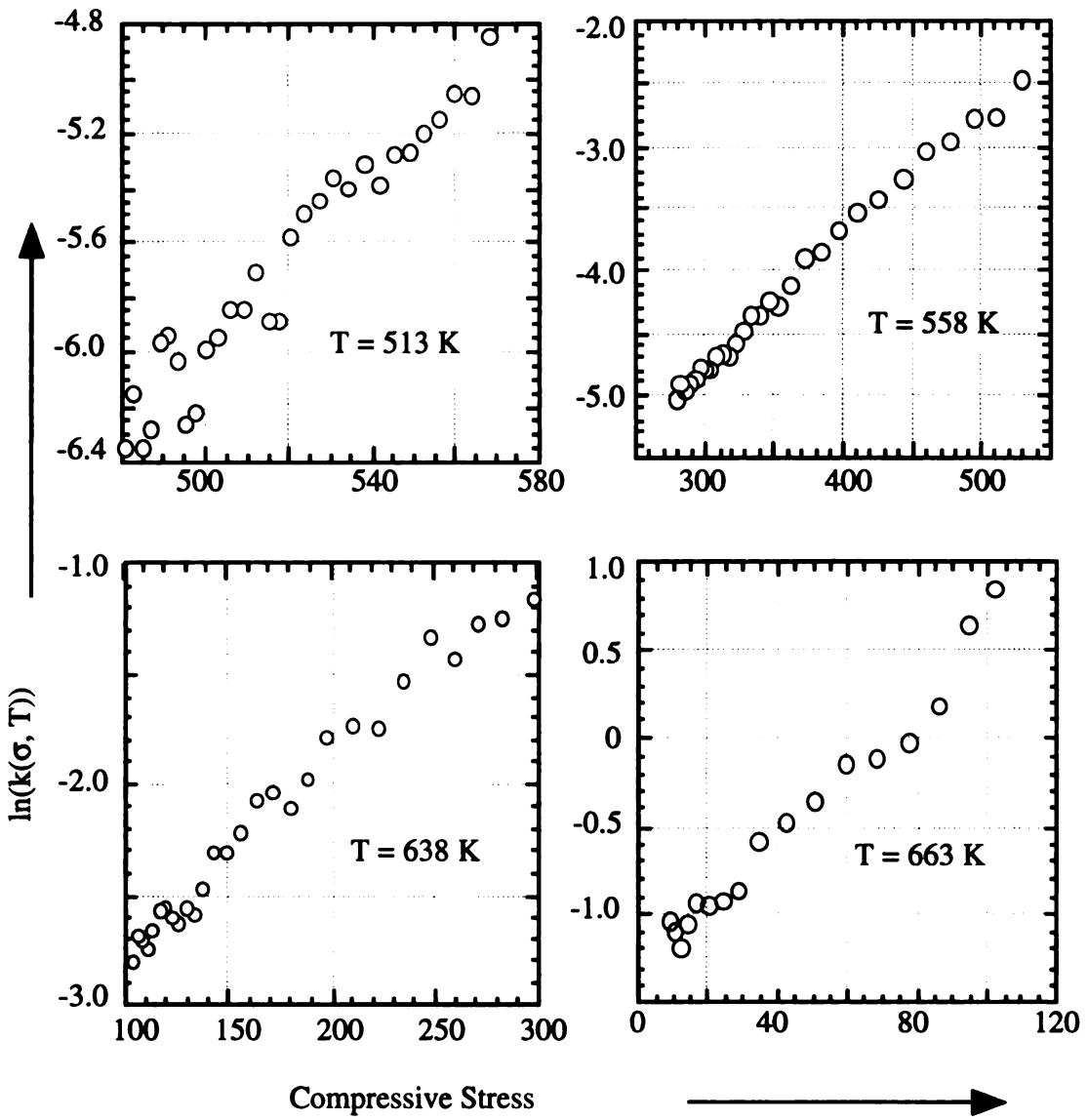

Figure 4-9 Plots of *ln(k(σ, T) vs. σ* for an as-sputtered amorphous NiTi on Si deposited at 473 K during isothermal annealing at various temperatures.

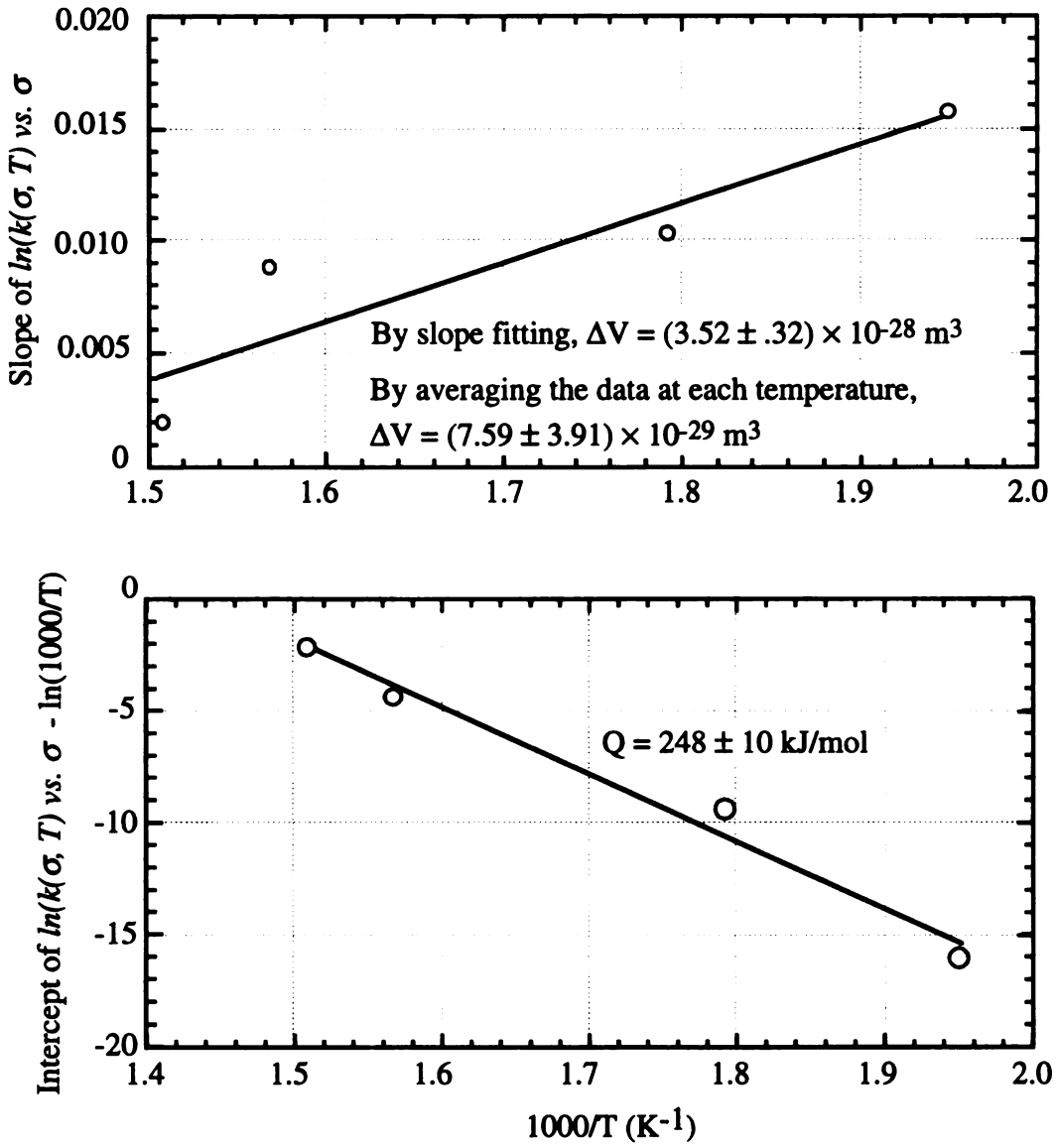

Figure 4-10 Calculations of Actiation volume (upper) and activation energy (lower) calculations for stress relaxation in fully amorphous NiTi on Si based on the intercepts and slopes in Fig. 4-9.

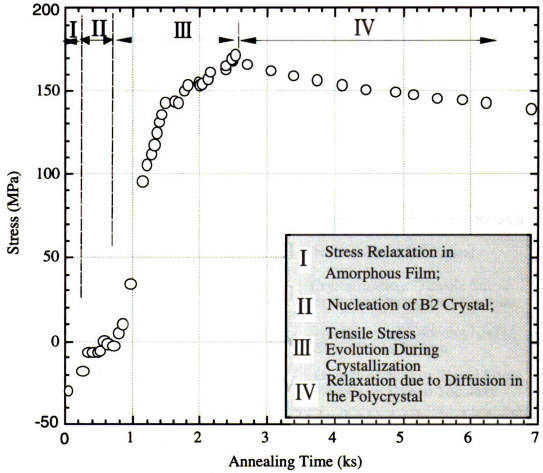

Figure 4-11(a) Stress evolution in a NiTi film deposited at ambient temperature during isothermal annealing at 723 K. TEM shows that the microstructure of the aged film is free of precipitates.

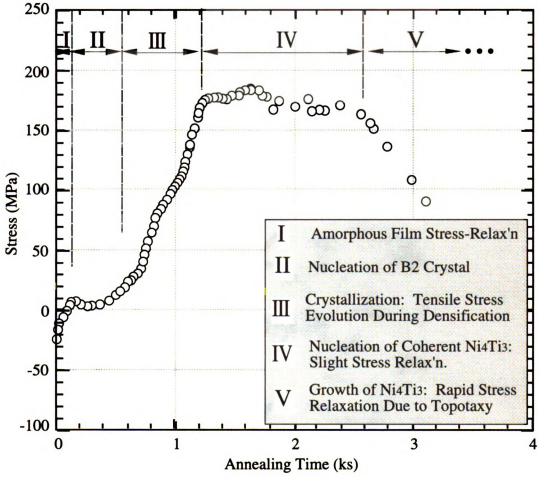

Figure 4-11(b) Stress evolution in a film deposited at 573 K during isothermal annealing at 713 K. TEM shows that the microstructure of the aged film contains numerous Ni_4Ti_3 precipitates.

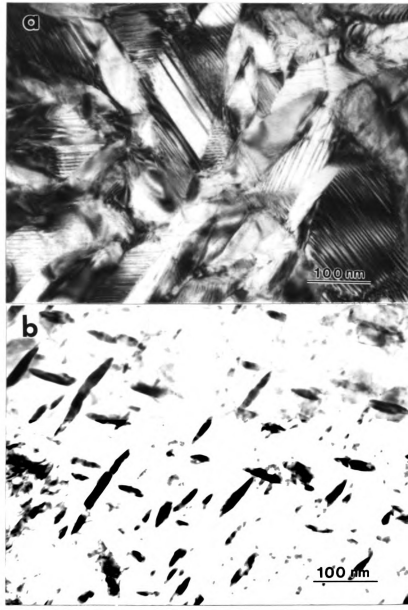

Figure 4-12 TEM micrographs showing the microstructures of the annealed films with two kinds of stress evolution behaviors during annealing at crystallization temperature:

(a) Microstructure is free of precipitates, corresponding to the film with a relatively lower relaxation rate after crystallization (see Fig 4-11(a));

(b) Large number of precipitates, corresponding to the film with a relatively faster relaxation rate after crystallization (see Fig. 4-11(b)).

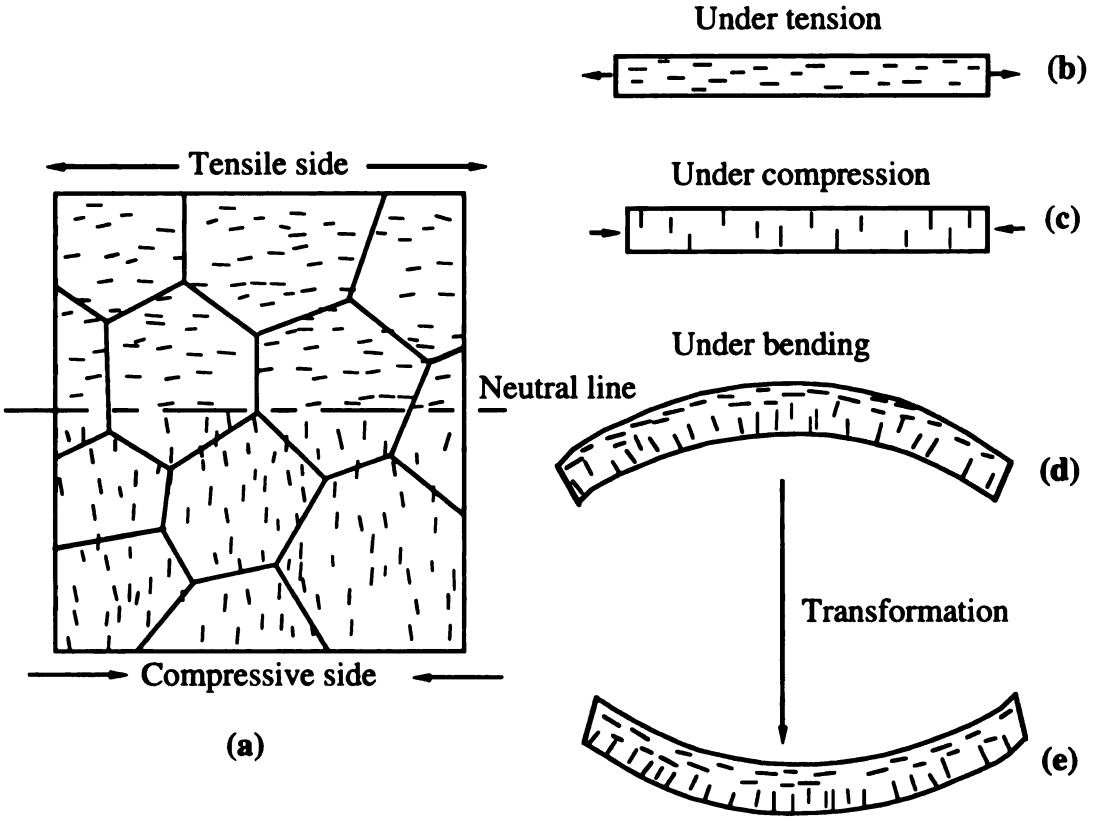

Figure 4-13. Constrained annealing effect on precipitation and intrinsic two-way memory effect mechanism in Ni-rich NiTi alloys proposed by Nishida *et al.* [Nishida *et al.*, 1987].

(a) Precipitate variant was selectively formed during annealing at 673 K ~ 873 K under bending stress for polycrystalline Ni-rich TiNi;

(b) Precipitate variant whose habit plane is most parallel to stress axis is formed if the sample is annealed under tensile stress;

(c) Precipitate variant whose habit plane is most perpendicular to stress axis is formed if the sample is annealed under tensile stress;

(d) Precipitates with different habit planes at different side of the sample are formed if the sample is annealed under bending stress. Curved shape is formed due to the relaxation of elastic constraint stress;

(e) When martensitic transformation is completed, the shape of the sample is inverted due to the biasing effect of the particularly oriented precipitates.

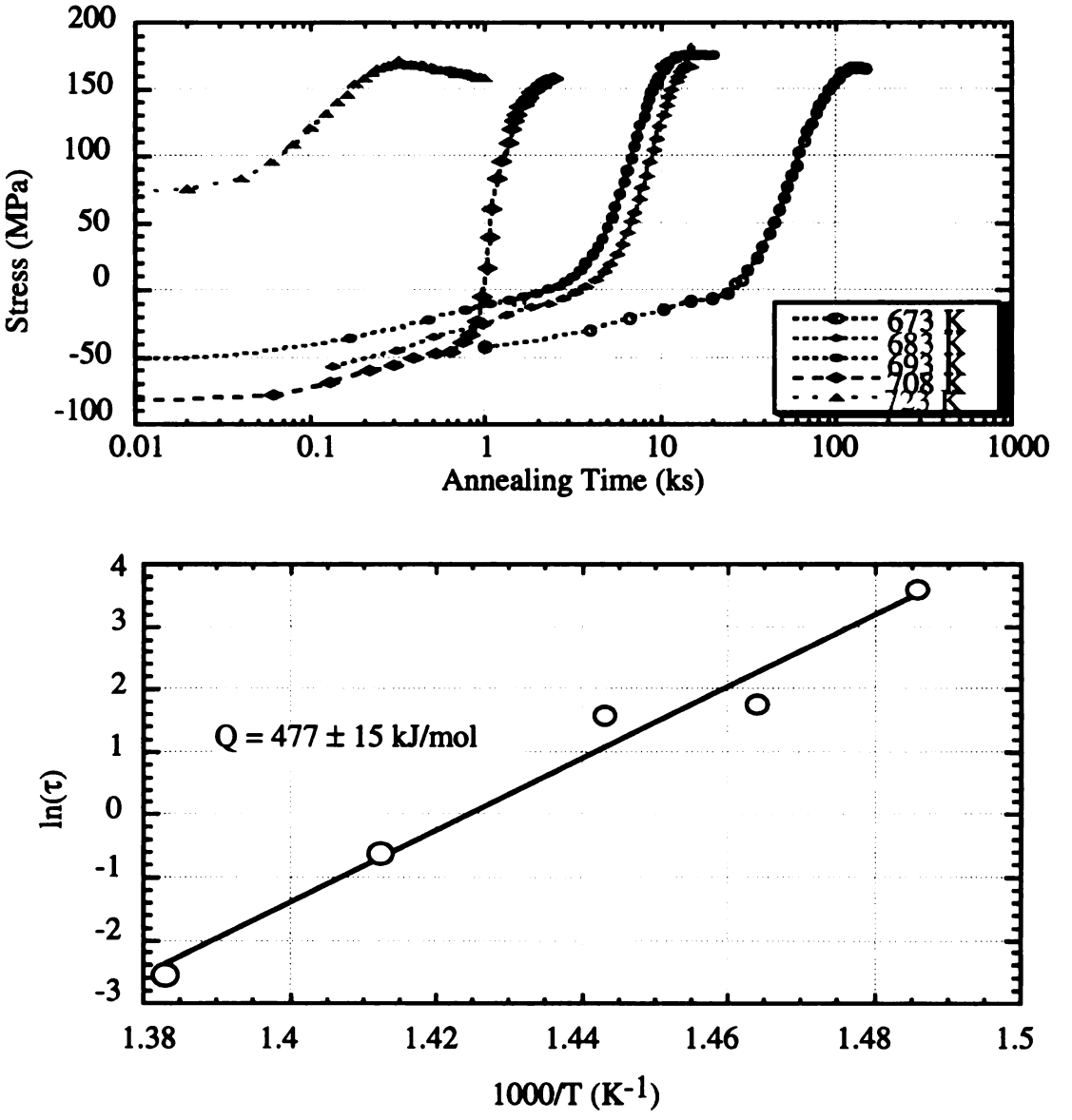

Figure 4-14 (a), Stress variation monitoring crystallization during annealing of amorphous NiTi films deposited at ambient temperature on Si.
(b), Calculation of activation energy for crystallization of amorphous NiTi films by linear fitting.

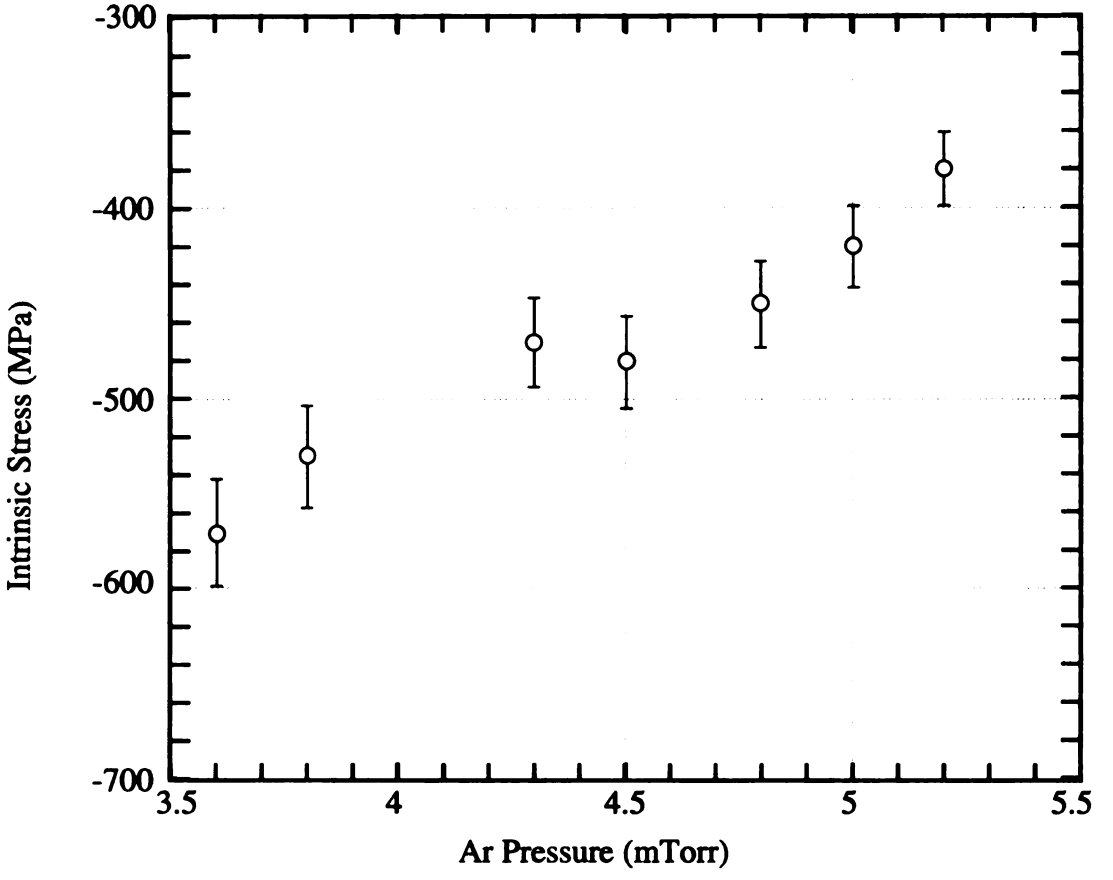

Figure 4-15 Intrinsic stress *vs.* working gas pressure for NiTi films on Si deposited at ambient temperature (T_d ~ 400 K) with film thicknesses ~1.5 to 2.5 microns.

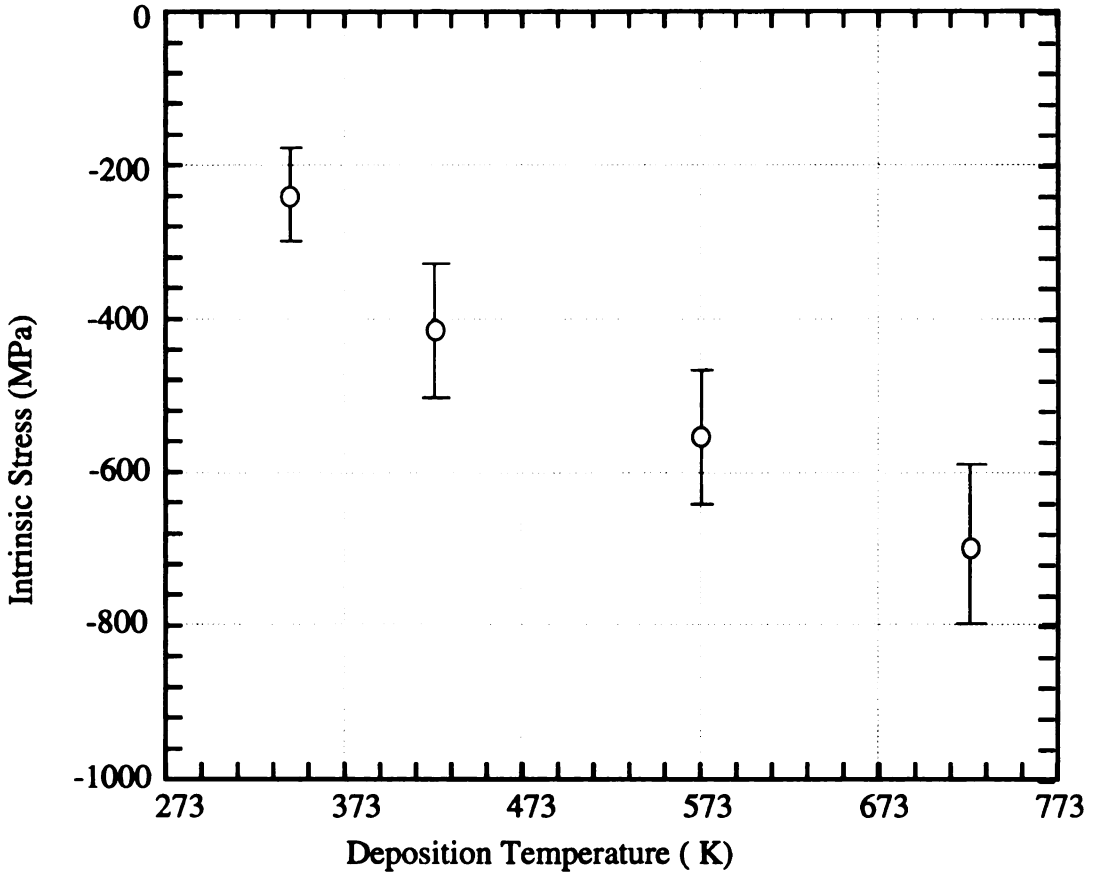

Figure 4-16 Intrinsic stress vs. deposition temperatures for NiTi films on Si deposited at constant working gas pressure of ~ 5.1 mTorr with film thickness 1.5 to 2.5 microns.

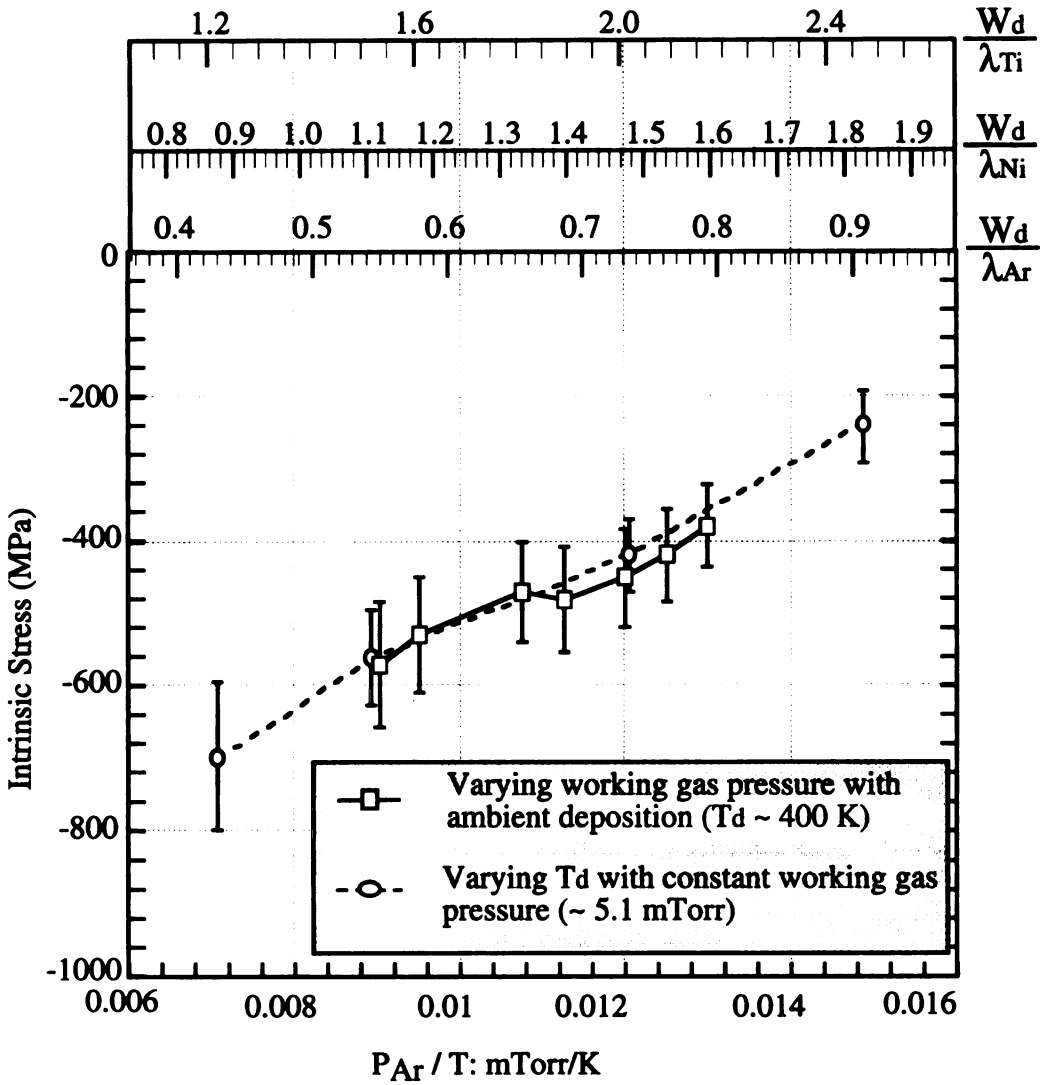

Figure 4-17 Intrinsic stress for as-sputtered NiTi on Si *vs.* the ratio of working gas pressure to deposition temperature, and ratio of working distance (Wd) to mean free-path of Ar (λ_{Ar}), Ni (λ_{Ni}) and Ti (λ_{Ti}) atoms. (combined Fig. 4.15 and 4.16).

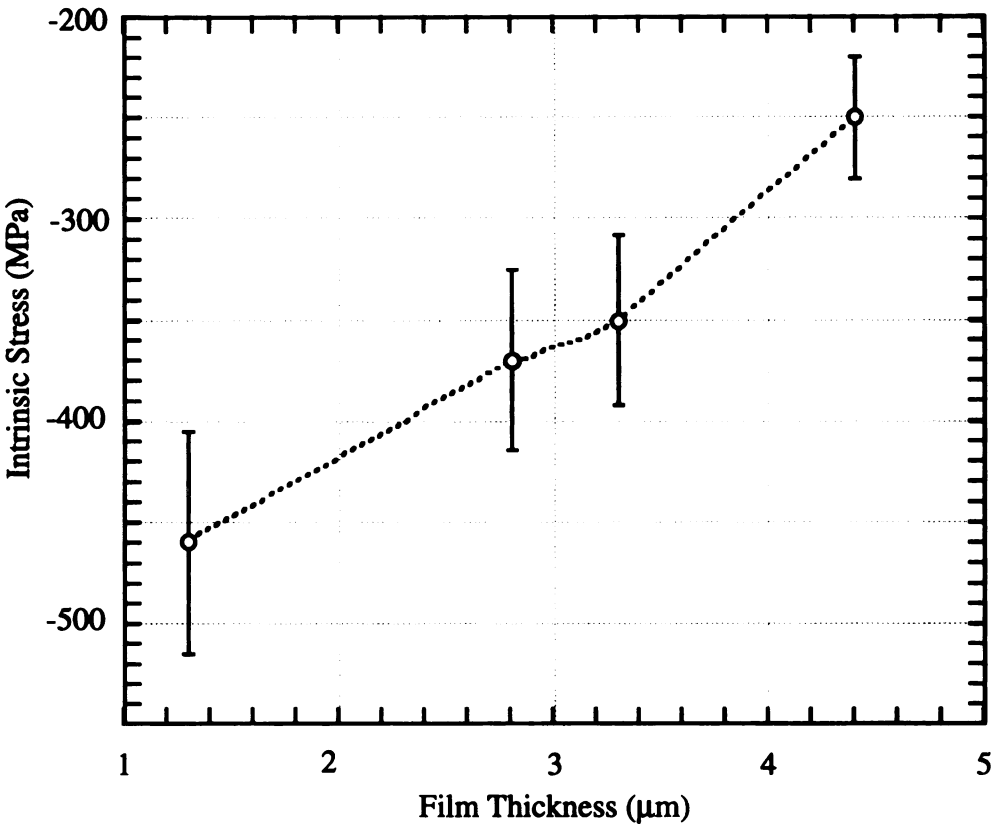

Figure 4-18 Intrinsic stress *vs.* film thickness for NiTi on Si deposited at ambient temperature (T_d ~400 K) and constant Ar pressure (5.1 mTorr).

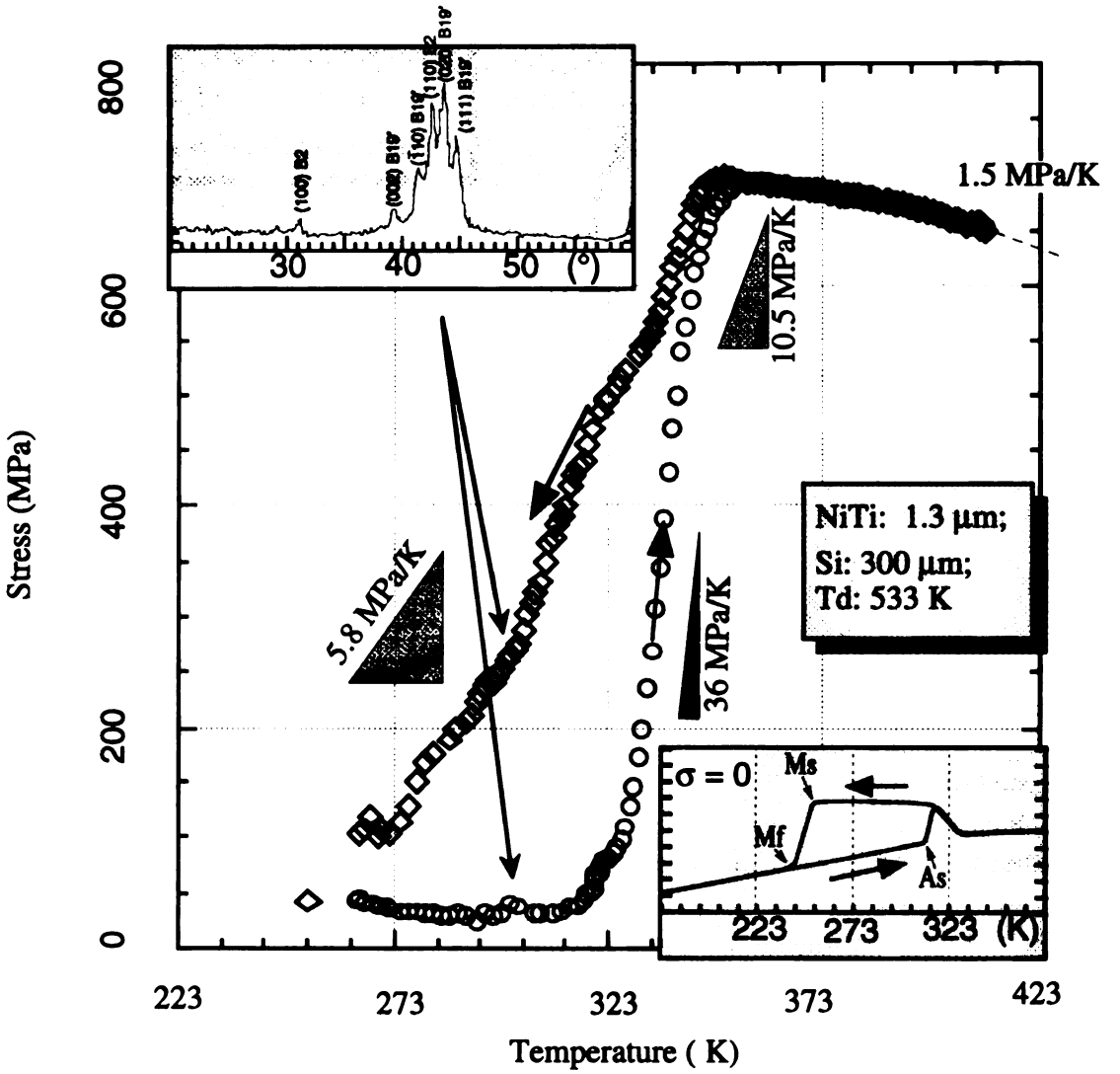

Figure 4-19 Stress relief and recovery during a cooling/heating cycle of a Ni-rich NiTi/Si composite after annealing for 2 hours at 723 K with X-ray diffraction spectrum at room temperature (left-upper corner) and resistivity curve for free-standing film.

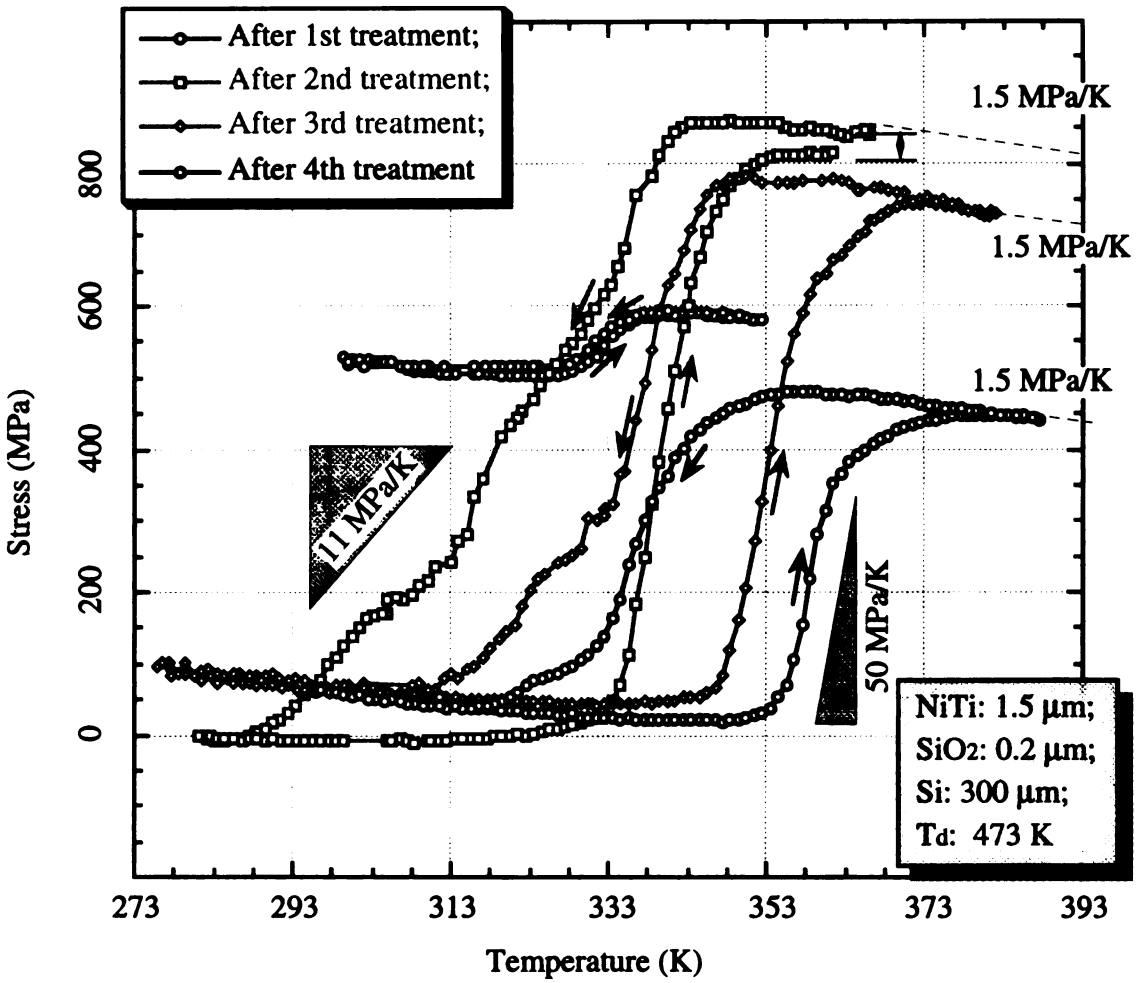

Figure 4-20 Stress relief and recovery during cooling/heating cycles of a Ti-rich NiTi/SiO_2/Si composite after different heat treatments.

1st treatment: 723 K, 2 Hours (the first cooling/heating cycle);
2nd treatment: 873 K, 1 Hour (the first cooling/heating cycle);
3rd treatment: 873 K, 4 Hour (the first cooling/heating cycle);
4th treatment: 873 K, 3.5 Hours (the second cooling/heating cycle).

The heat treatments were applied to the same sample so the effect was accumulative.

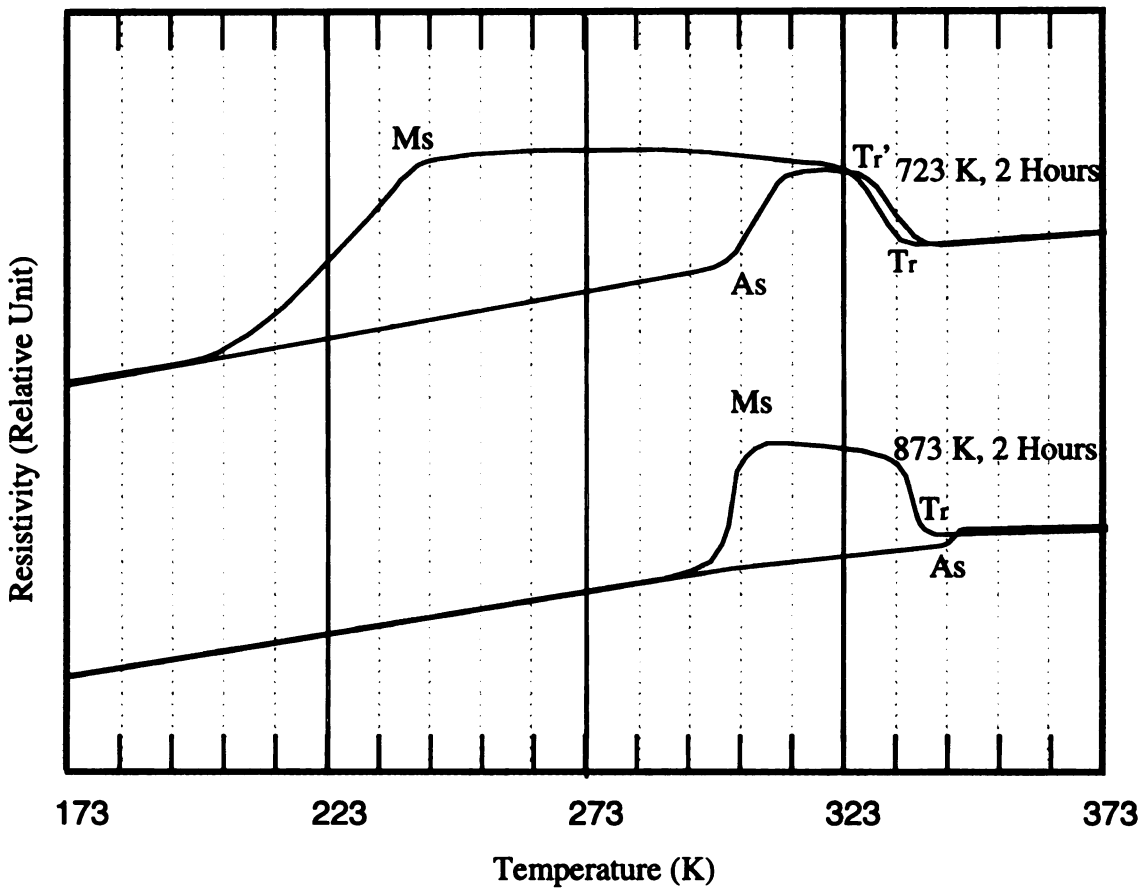

Figure 4-21 Resistivity vs. temperature curves of free-standing Ti-rich NiTi films that was annealed 2 hours at 723 K (upper) and additional 2 hours at 873 K (lower).

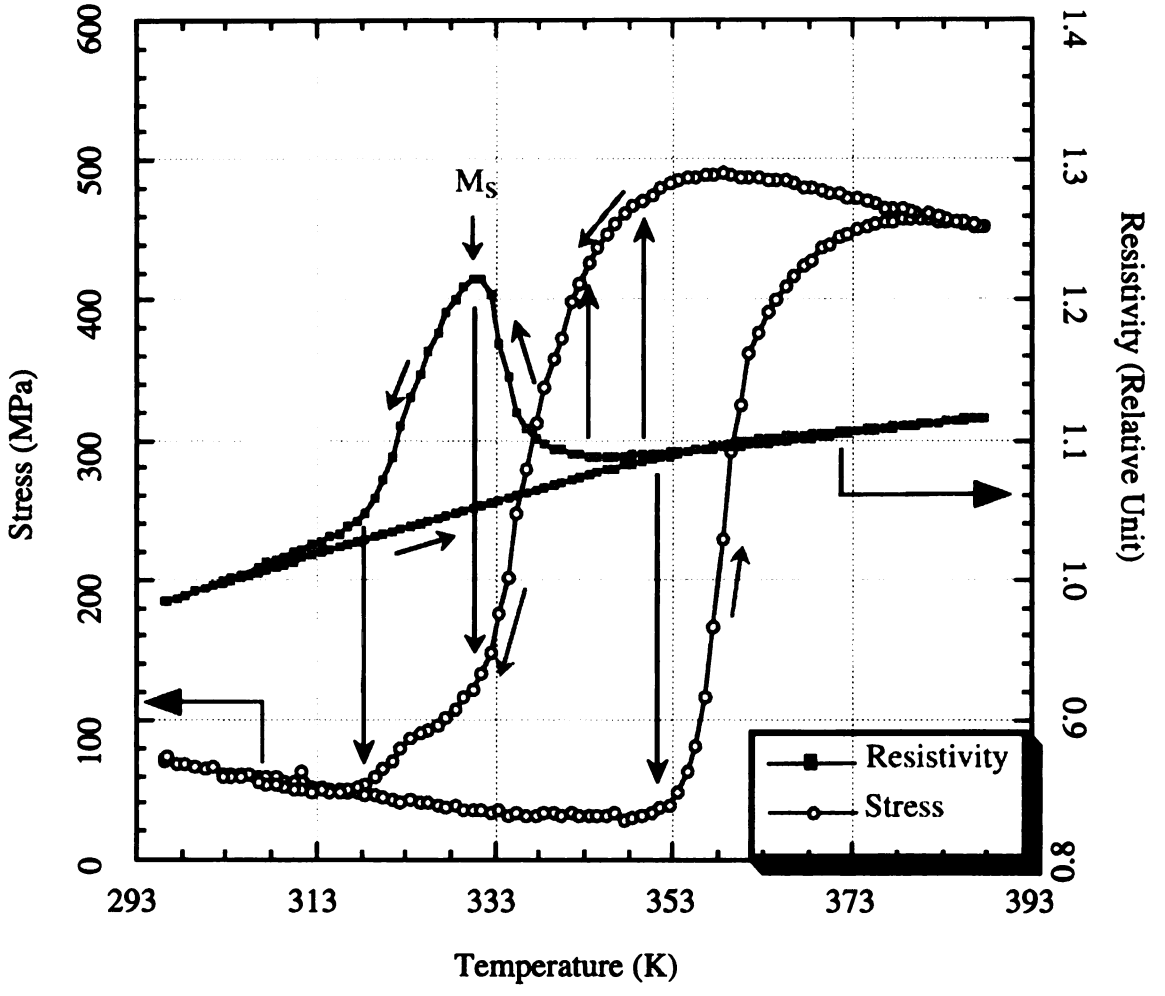

Figure 4-22 Stress variation with temperature during the second cooling/heating cycle of a Ti-rich NiTi/SiO_2/Si composite that has been annealed at 723 K for 2.5 hours followed by anneals at 873 K with accumulative time of 8.5 hours. *In-situ* resistivity measurement was used to monitor phase transformation.

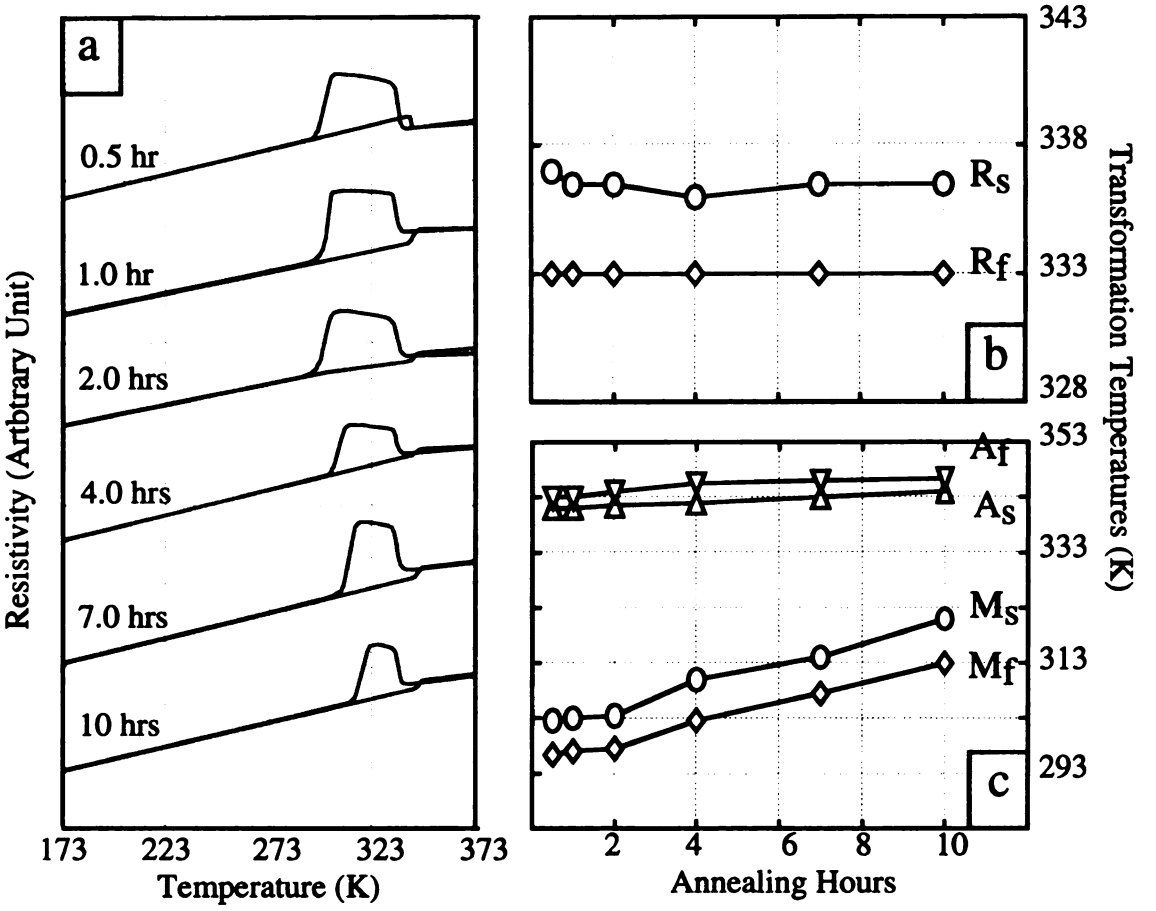

Figure 4-23 **(a)** Resistivity - temperature curves of Ti-rich NiTi films annealed at 873 K for varying time during thermal cycles at stress-free states. **(b),** R-phase transformation temperatures are stable; **(c),** martensitic transformation temperatures increase with increased annealing time at 873 K.

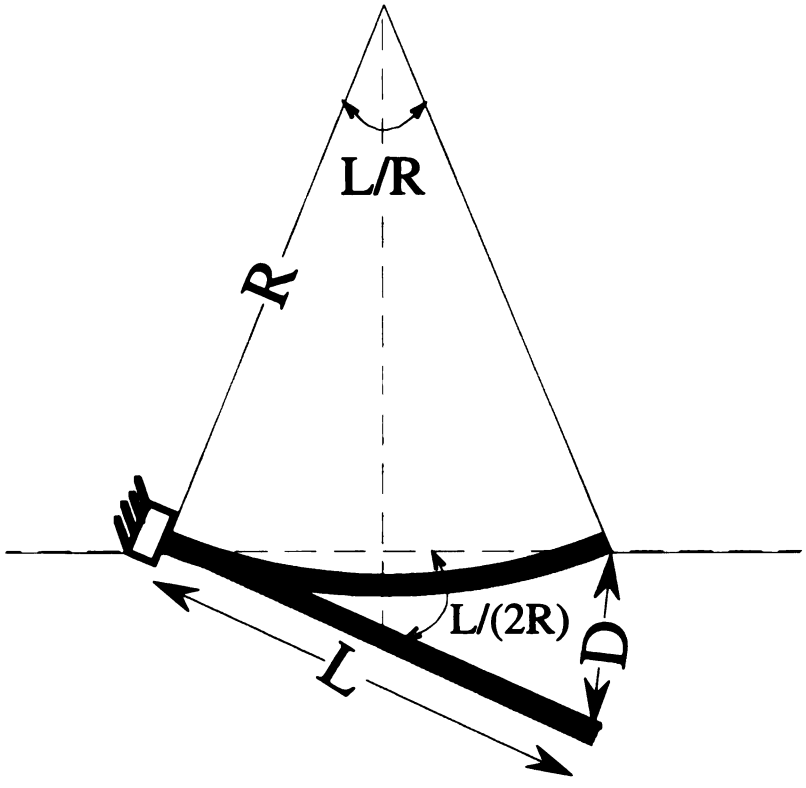

Figure 4-24 Clacualtion of displacement of a cantilever deposited a NiTi layer resulting from stress relaxation by phase transformations.

Considering only elastic deformation, the displacement at one end of the component when the other end is secured can be determined by:

$$D = \frac{L}{2R} * L$$